論文 / 著書情報
Article / Book Information

題目(和文)	
Title(English)	Simulation of quantum Griffiths singularity using a programmable quantum annealer
著者(和文)	西村光嗣
Author(English)	Kohji Nishimura
出典(和文)	学位:博士(理学), 学位授与機関:東京工業大学, 報告番号:甲第11369号, 授与年月日:2020年3月26日, 学位の種別:課程博士, 審査員:西森 秀稔,村上 修一,樺島 祥介,田中 秀数,西田 祐介
Citation(English)	Degree:Doctor (Science), Conferring organization: Tokyo Institute of Technology, Report number:甲第11369号, Conferred date:2020/3/26, Degree Type:Course doctor, Examiner:,,,,
学位種別(和文)	博士論文
Type(English)	Doctoral Thesis

Doctoral Thesis

Simulation of quantum Griffiths singularity using a programmable quantum annealer

Kohji Nishimura

Department of Physics
Tokyo Institute of Technology

February 14, 2020

Abstract

In this thesis we study the simulation of the Griffiths-McCoy singularity on a physical quantum annealer.

Quantum annealing is one of the heuristic algorithms for solving combinatorial optimization and has been gaining attention because of its physical implementation on a commercialized device named the D-Wave machine. Although this machine initially aimed at performing ideal quantum annealing, the coherent time-evolution is disturbed by environment noise. Moreover, it has turned out that the measurement result from the D-Wave machine in some cases follows the Boltzmann distribution, leading to practical applications of the D-Wave machine as a classical Boltzmann sampler. Besides, recent studies show that the D-Wave machine can also be used as a sampler of the quantum Boltzmann distribution, that is, simulator of the quantum thermal equilibrium state. Studies also demonstrate the simulation of the quantum phase transition of the quantum spin glass model on the D-Wave device, which provides a potential to an application of the D-Wave device as a quantum simulator.

Motivated by these studies, we show another example of the quantum simulation, quantum simulation of the Griffith-McCoy singularity, on the D-Wave device. We first investigated this physical phenomenon by using quantum Monte Carlo simulation on a large-scale computing and confirmed that the model we deal with does exhibit the Griffiths-McCoy singularity. Next we demonstrate the simulation of the same model on the D-Wave device, leading to the conclusion that the result is qualitatively consistent with the one from the quantum Monte Carlo method. This means that the D-Wave device can capture the Griffiths-McCoy singularity, which is the first example of the demonstration of this physical phenomenon. This research sheds important light on demonstrating physical phenomenon on a real programmable quantum device, not a simulation on a conventional digital computer.

Acknowledgments

First, I would like to thank my research advisor Prof. Hidetoshi Nishimori for giving various fruitful advice and stimulating discussions to advance my study. I would also like to thank members in his group, Kazutaka Takahashi, Patrick Koh, Yuki Bando, Kabuki Takada, Yu Yamashiro, Keisuke Suzuki, Noriko Uesugi for useful comments and kind supports throughout my doctoral course. The main part of the study is done during my stay in Texas A&M University. I am very grateful to Prof. Helmut G. Katzgraber, members of his laboratory, Andrew Ochoa and his family in supporting me kindly during my stay in Texas and giving useful ideas which improves my study. I also would like to thank D-Wave systems, Inc. and the members of the company for supporting me during the visit. I would especially like to thank Richard Harris for guiding me how to use the D-Wave machine as a quantum simulator face-to-face at the office. As for computational resource, I would like to acknowledge the TSUBAME supercomputer for the large-scale quantum Monte Carlo simulation. Also I would like to acknowledge IARPA QEO project for the extensive use of D-Wave 2000Q located at NASA. The most part of the thesis was written at the office of Jij Inc. I would like to thank all members at Jij Inc. I acknowledge the financial support from the Research Fellowship of the Japan Society for Promotion of Science. Finally, I would like to show my gratitude to my family for their supports.

List of publication

1. K. Nishimura, H. Nishimori, A. J. Ochoa, and H. G. Katzgraber, "Retrieving the ground state of spin glasses using thermal noise: Performance of quantum annealing at finite temperatures", *Phys. Rev. E* **94**, 032105, (2016).

2. K. Nishimura, H. Nishimori, "Quantum annealing with a nonvanishing final value of the transverse field", *Phys. Rev. A* **96**, 042310, (2017).

3. K. Nishimura, K. Takahashi, "Counterdiabatic Hamiltonians for multistate Landau-Zener problem", *SciPost Phys* **5**, 029, (2018).

Contents

1. Introduction

Quantum mechanics is one of the most established and important fields in modern physics in the twenty-first century. Starting with the discovery of the Planck's law which was originally introduced to explain black-body radiation precisely, the theory of quantum mechanics has been developed throughout the twentieth century. Although some of the topics in quantum mechanics such as the superposition principle and the collapse of wave function by measurement have aroused a lot of controversies since they seemingly contradict conventional intuitions, these theories have been now refined and sophisticated so that they are now regarded as an established one. Now quantum mechanics forms a fundamental part of modern physics.

One of the promising applications of quantum mechanics which has recently been gaining much attention is quantum computing. The concept of quantum computing is first proposed by Feynman [1]. He states that quantum computer may have a potential to calculate particular kind of tasks exponentially faster than conventional classical computers by using unique properties of quantum mechanics which classical computer needs huge resources that grows exponentially as a function of system size to simulate. After the Feynman's suggestion, various kinds of studies related to quantum computing have been performed especially in terms of computational complexity and some algorithms which are proven that they can solve certain kind of problems faster than classical computers have been discovered [2]. For instance, Grover's algorithm [3] can solve the database search problem, a problem to find the input to a black box function which produces a certain output, with only $O(\sqrt{N})$ evaluations of function while it costs in general $O(N)$ times with classical computers. One of the notable quantum algorithm which is exponentially faster than existing classical algorithm is Shor's algorithm [4] which can be used for prime factorization. Another example of exponentially fast quantum algorithm is the HHL algorithm [5] which is effective for solving linear systems of equations. Theoretical studies of quantum computing have been developed steadily starting with these notable algorithms.

Besides, building a real quantum computer is also a central topic of recent quantum science and technology. Even if the theory of quantum computing is established and developed, constructing a physical device which demonstrates these theories experimentally is in general quite a difficult task due to the existence of environment noise which often causes decoherence of quantum system and hampers demonstrating ideal quantum time evolution. Nevertheless, steady progress of experimental technology enables us to perform larger scale quantum computing than before and the size of problems physical quantum devices can handle is growing year by year. In October 2019, Google has announced the achievement of "quantum supremacy" [6]. They showed the first example that physical quantum device can solve a certain kind of problem which the existing state-of-the-arts supercomputer cannot carry out in a practical time. As of 2020, one of the main directions of the study of quantum computing is to find practical applications which currently (or near-term) available quantum devices can perform more efficiently than conventional classical computers. These types of near-term available quantum device that can perform intermediate scale quantum computation are often referred to as *Noisy Intermediate-Scale Quantum (NISQ)* device as proposed by Preskill [7].

In this thesis, however, we will focus on the other type of quantum device based on *quantum annealing*, not the device based on "quantum gate model" explained above.

Quantum annealing is a quantum algorithm originally proposed by Kadowaki and Nishi-

mori [8] which aims to solve combinatorial optimization by using quantum mechanics. In this paper they showed that quantum annealing may outperform a classical counterpart algorithm by using numerical computation. This quantum algorithm is now gaining a growing attention because of the physical realization of this algorithm which is often referred to as *quantum annealer* by a company named D-Wave Systems [9]. Although at first it was unclear if this device really uses the quantum mechanics explicitly, it has now been confirmed that this D-Wave quantum annealer can exhibit data which definitely obeys quantum mechanics [9–11]. As for combinatorial optimization, various studies show the superiority of the D-Wave machine for certain kinds of problems. For example, D-Wave system has reported that the quantum annealer can solve a certain kind of combinatorial optimization problem (weak-strong cluster problem) 10^8 times faster than one of the classical counterpart algorithms (naive simulated annealing) [12]. Although the subsequent research [13] defeated the result by employing the state-of-the-art classical heuristics, it can still be said that the performance of the D-Wave machine is now comparable to that of classical computers. Finding a practical problem that D-Wave device outperforms the classical computer is of course one of the central tasks of recent studies.

Similarly to the "quantum gate model computer" device explained above, decoherence caused by environment noise also affects the performance of the quantum annealer significantly. The performance of quantum annealing in the presence of finite temperature is discussed in several studies. For example, the study [14] pointed out that the temperature with which the quantum annealer performs ideal quantum annealing must be scaled down with the problem size, whereas the study [15] shows that the finite temperature may help the annealer reach the optimal solution. Interestingly, a study [16] point out that there is a case that the results from the quantum annealer follows the canonical distribution of thermal equilibrium state with the given Hamiltonian rather than ideal time evolved state owing to thermalization induced by environment noise. For these reasons it cannot be said that the D-Wave machine can perform "ideal" quantum annealing in the presence of environment noise.

Recently, another approach of the use of the D-Wave machine, using the D-Wave machine not an optimizer but as a quantum simulator, starts to gain much attention. Initial research of the use of the D-Wave machine as a quantum simulator was done by Harris et al. [17] where they showed experimentally that the D-Wave machine can sample quantum thermal equilibrium states with particular annealing schedule. They also show that the D-Wave machine can simulate three-dimensional quantum Ising spin glass. Another example is by King et al. [18] where they show that the D-Wave machine also exhibits the established physical phenomena, Kosterlitz-Thouless transition [19].

Although these physical phenomena can be simulated by using quantum Monte Carlo method on conventional classical computers in principle, it is still of great significance to demonstrate them on the D-Wave machine because of the following reasons. First, the calculation process between the quantum annealer and quantum Monte Carlo method is intrinsically different. The quantum annealer generates a real quantum state inside the apparatus and outputs the result by measuring magnetic flux of each qubit, whereas quantum Monte Carlo method is one of stochastic simulations on classical computers. It can be said that the quantum annealer can be regarded as a device for large-scale real physics experiments with programmable parameters. Simulation on the D-Wave machine corresponds to a realization of physical phenomena that are predicted by numerical computations. Second, the calculation time of the quantum annealer is much faster than that of classical computers. An annealing process inside the device typically takes several microseconds where quantum Monte Carlo method on the classical computer requires, even with small number of Monte Carlo steps, at least several seconds. Recent study [20] shows an advantage of computational time of the D-Wave machine over classical computers.

Pursing of the quantum simulation on the D-Wave machine is hence of great importance.

In this thesis, we show another example of quantum simulation of the D-Wave machine whose phenomenon is qualitatively different from the above studies: the Griffiths-McCoy singularity. This phenomenon can be characterized as a kind of singularity which occurs in a paramagnetic phase on a percolated quantum Ising system and has been studied especially by using numerical computations [21–26]. Since the previous studies of the use of the D-Wave machine as a quantum simulator mainly focused on the simulation of a global phase transition of the quantum Ising system, this thesis gives a first example of the use of the D-Wave quantum annealer as a quantum simulator which is different from exhibiting a global phase transition. Note that, though we have emphasized only the use of the D-Wave quantum annealer throughout this introduction, this method can be applied not only to the D-Wave machine but also to the same type of quantum annealer which is expected to be constructed by other organizations in the near future.

The thesis is organized as follows. Chapters 2 and 3 show preliminaries of this study. In Chapter 2, we give an overview of quantum annealing and its physical implementation on the D-Wave machine. We first give an introduction to spin glass, the Ising model with disordered interaction, which has a remarkable relation to quantum annealing due to its correspondence to combinatorial optimization problems. Next we introduce a detailed explanation of quantum annealing and how it is implemented on the real physical quantum device, the D-Wave machine. We also give an overview of the D-Wave quantum annealer especially how it works and how to perform quantum simulation on this quantum annealer. In Chapter 3, We show the historical background of the Griffiths-McCoy singularity which we are going to simulate on the D-Wave machine in this study. We also explain what kind of physical quantity shows this singularity.

Chapters 4 and 5 show the results of this study. To confirm that the D-Wave machine really exhibits the result that is physically reasonable, we investigate the physical properties of the model with large-scale quantum Monte Carlo simulation in advance, which is elucidated in detail in Chapter 4. Chapter 5 is the main part of this thesis: simulating on the D-Wave machine. In this chapter we show that the D-Wave machine can simulate the Griffiths-McCoy singularity. We also discuss the comparison to the result obtained from quantum Monte Carlo method in Chapter 4.

Chapter 6 gives concluding remarks of this thesis.

Technical details which are not essential parts of the study are summarized in Appendices.

2. Quantum Annealing and its physical implementation

In this chapter we mainly give an introduction to quantum annealing and its physical implementation on the D-Wave machine. First we give a brief introduction to spin glass, the Ising model with random interactions and its correspondence to the combinatorial optimization problems since quantum annealing mainly focuses on spin glass Hamiltonian when solving a problem. After explaining the concept of quantum annealing, we focus on the physical quantum device, the D-Wave quantum annealer. We show an overview of the D-Wave machine and how it can be used as a quantum simulator of thermal equilibrium states of quantum Ising Hamiltonian by using the *anneal-pause-quench protocol*.

2.1. Spin glass

First, let us give a brief introduction to the ordinary Ising model. The Ising model [27] is a mathematical model of magnetic materials used in statistical mechanics frequently. This model consists of a set of discrete variables $\boldsymbol{S} = \{S_i \in \pm 1 | 1 \leq i \leq N\}$ which represents configurations of classical electron spins, interactions J between the spins, external magnetic field h, and the Hamiltonian $H(\boldsymbol{S})$. A typical Hamiltonian of the Ising model can be written as follows:

$$H(\boldsymbol{S}) = -J \sum_{(ij)\in C} S_i S_j - h \sum_i S_i, \tag{2.1}$$

where C shows the connectivity between spins. This model indicates that, in the case of $J > 0$ (ferromagnetic Ising model), the spins in the system tend to align themselves in the same direction so that the total energy becomes smaller. Any physical quantity such as the magnetization and the susceptibility is derived from the *partition function* in terms of thermal average (hereafter denoted as triangular brackets with the inverse temperature subscript $\langle \cdots \rangle_\beta$),

$$Z(\beta) = \mathrm{Tr} \exp\left[-\beta H(\boldsymbol{S})\right], \tag{2.2}$$

where Tr denotes the sum over all spin configurations. Hence calculating the partition function is of great importance to understand the behavior of the system.

Despite the simplicity of this model, the Ising model can describe *phase transitions* which are one of the most important topics in statistical mechanics [28]. It is known that there exist two phases in the ferromagnetic Ising model. One is the *ferromagnetic phase* which appears at low temperature. The magnetization takes a finite value in this phase. One finds a disappearance of magnetization as the temperature increases. This means that the system turns into the other phase, the *paramagnetic phase*. It is known that this phase transition occurs under the condition that the dimension of the system is two or larger. However, the exact solution of this model is an open problem even now, except for the case of the one-dimensional Ising model, the two-dimensional lattice Ising model, and the mean-field Ising model. The one-dimensional model can be solved easily by the transfer matrix method [27], whereas it is a little complicated to solve the two-dimensional model, which was first solved by Onsager [29].

Suppose that the interactions are different at each site ($J \to J_{ij}$). How does the behavior change? This is the topic of the theory of *spin glasses* [30].

The spin glass is a disordered system where magnetic spins are not aligned uniformly but fixed in time. The term of spin glasses comes from similarity to chemical glasses whose atomic configurations are disordered but frozen (an amorphous phase). This model Hamiltonian can be written as a generalization of the simple ferromagnetic Ising model whose interactions depend on site (referred to as the *quenched disorder*),

$$H(\boldsymbol{S}) = -\sum_{(ij)\in C} J_{ij}S_iS_j - \sum_i h_iS_i. \tag{2.3}$$

One of the notable features of spin glasses is that it has another phase which is neither ferromagnetic nor paramagnetic unlike the conventional Ising model, the *spin glass phase*, where the configurations of spins are disordered but fixed in time.

Another feature is that the definitions of physical quantities change slightly from those of the ferromagnetic Ising model. Remember that every physical quantity of the Ising model can be derived as a thermal average. Besides, there is randomness in interactions in the spin glass model. To calculate a physical quantity without any explicit dependence on J_{ij}, a new concept of the average, the *configurational average*, should be introduced in addition to the thermal average. Supposing that interactions J_{ij} obey the probabilistic distribution $P(J_{ij})$, the configurational average $[\cdots]$ is defined as

$$[\cdots] \equiv \int dJ_{ij}P(J_{ij})(\cdots). \tag{2.4}$$

Hereafter all physical quantities in spin glasses will be treated in the form of configurational average.

Now let us introduce some famous models in the spin glass theory. The model which has only two-body-nearest-neighbor interactions is called the *Edwards-Anderson model* [31],

$$H(\boldsymbol{S}) = -\sum_{\langle ij\rangle} J_{ij}S_iS_j, \tag{2.5}$$

where $\sum_{\langle ij\rangle}$ is the sum over nearest-neighbor pairs. While the exact solution to this model has not been discovered, the infinite-range version of the Edwards-Anderson model, which is referred to as the *Sherrington-Kirkpatrick model* [32] (referred to as the SK model later), turned out to be a solvable model by the mean field analysis and the *replica method*.

$$H(\boldsymbol{S}) = -\sum_{i<j} J_{ij}S_iS_j, \tag{2.6}$$

where $\sum_{i<j}$ is the sum over all distinct pairs of spins.

The spin glass phase described above is clearly formulated in mathematical forms as follows. One needs two types of order parameters,

$$m = [\langle S_i\rangle_\beta], \tag{2.7}$$

$$q = [\langle S_i\rangle_\beta^2]. \tag{2.8}$$

The quantity m is the magnetization, whereas q is an order parameter unique to spin glasses. Remember that each spin is not aligned uniformly in space but fixed in time in the spin glass phase. It follows that the thermal average of spin has a finite value but varies from site to site. Hence the configurational average of the thermal average vanishes but that of the squared thermal average will survive. This leads to the conclusion that the spin glass phase corresponds to the case $m = 0$ and $q > 0$. The paramagnetic and ferromagnetic phases correspond to the case $(m = 0, q = 0)$ and $(m > 0, q > 0)$, respectively.

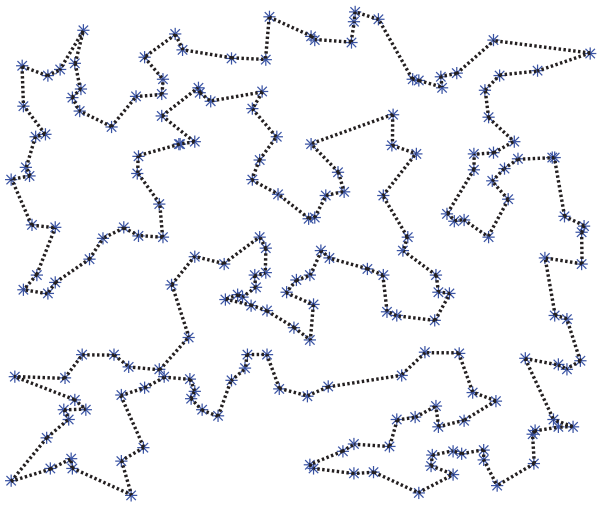

Figure 2.1.: An optimal solution of TSP for 200 cities. A blue dot shows each city and black dashed line shows the path.

2.1.1. Applications to combinatorial optimization problems

Recently, another aspect of the spin glass theory has attracted attention for its application to combinatorial optimization problems.

Combinatorial optimization is the problem to find the solution which minimizes a given cost function [33]. Various tasks in modern society can be mapped into this type of problems, hence solving combinatorial optimization problem as efficiently as possible has great significance. However, finding the optimal solution is difficult in general due to the exponential growth of the calculation time. One of the strategies to avoid this difficulty is to apply a heuristic algorithm which finds an approximate solution rather than the exact one. Many kinds of algorithms to solve these problems quickly have been studied until now [8, 34–37]. It has been known that finding the ground state of spin glasses is equivalent to solving combinatorial optimization problems (see [38] for examples). This section represents how combinatorial optimization problems can be mapped into spin glass problems.

To begin with, each spin variable σ_{ij} is assumed to take either 0 or 1, not ± 1, for simplicity. Let us map the famous combinatorial optimization problem, the *traveling salesman problem* (TSP), into a spin glass [38, 39]. The traveling salesman problem is to find the optimal path which visits all N cities only once each and returns to the starting point. Figure 2.1 is the illustration of an optimal solution of TSP. To relate a salesman's path with a spin configuration, a spin glass, where index i of spin $\sigma_{ij} \in \{0, 1\}$ indicates the city name and index j indicates the number of cities one has visited until now, is prepared. Then, σ_{ij} takes 1 if one visits city i and this is the jth city for his travel and takes 0 otherwise. Figure 2.2 may help the reader understand this situation. The cost

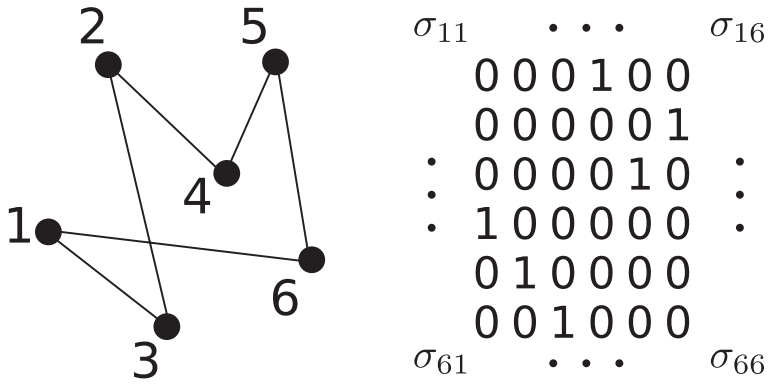

Figure 2.2.: Left: A connectivity of cities and a path ($4 \to 5 \to 6 \to 1 \to 3 \to 2 \to 4$). Right: Corresponding spin configurations.

function of TSP is represented as the Hamiltonian below:

$$H(\boldsymbol{\sigma}) = AE_1 + BE_2 + CE_3, \tag{2.9}$$

$$E_1 = \sum_{i=1}^{N} \left(\sum_{j=1}^{N} \sigma_{ij} - 1 \right)^2, \tag{2.10}$$

$$E_2 = \sum_{j=1}^{N} \left(\sum_{i=1}^{N} \sigma_{ij} - 1 \right)^2, \tag{2.11}$$

$$E_3 = \sum_{i,j,k=1}^{N} J_{ik}\sigma_{ij}(\sigma_{kj+1} + \sigma_{kj-1}). \tag{2.12}$$

Equations (2.10) and (2.11) represent the constraining conditions that each city should be visited only once. These terms vanish only if the estimated path does not violate these constraints. The coefficient $J_{ik} > 0 \in \mathbb{R}$ in Eq. (2.12) is the distance between city i and city k. Hence Eq. (2.12) represents the sum of the path lengths. Coefficients A, B, and C are adjustable parameters. The expansion of Eq. (2.9) results in the form of two-spins interactions and a external magnetic field,

$$\begin{aligned} H(\boldsymbol{\sigma}) &= \sum_{ijkl} K_{ijkl}\sigma_{ij}\sigma_{kl} + L\sum_{ij}\sigma_{ij}, \\ K_{ijkl} &= A\delta_{ik} + B\delta_{jl} + CJ_{ik}(\delta_{lj+1} + \delta_{lj-1}), \\ L &= -2(A+B), \end{aligned} \tag{2.13}$$

where constant terms are omitted. The task is to find the ground state of this Hamiltonian to obtain the optimal salesman's path.

2.2. Quantum annealing

Since solving these combinatorial optimization problems is of great social significance, some algorithms have been suggested as an application of statistical mechanics. One of these algorithms is called simulated annealing (SA) [37] which uses thermal fluctuations to escape from a local minimum of the cost function and reach the global minimum. This strategy first searches the total solution space by setting a temperature-like parameter to a sufficiently large value. As the parameter decreases to zero slowly, the derived solution converges to the optimal one which minimizes the cost function. The study by Geman

and Geman [40] reveals that the probability of reaching the optimal solution by using SA is guaranteed to converge to unity as the temperature $T(t)$ as a function of an elapsed time t decreases by following the schedule:

$$T(t) \sim \frac{c}{\log(1+t)}, \tag{2.14}$$

where c is a constant.

Quantum annealing (QA) is one of the alternative strategies to SA established by Kadowaki and Nishimori [8]. Unlike SA, this strategy uses quantum fluctuations to derive the optimal solution instead of thermal fluctuations. Let us give a more detailed explanation by preparing the target spin glass Hamiltonian H_0 whose interactions describe the corresponding combinatorial optimization problem,

$$H_0 = -\sum_{ij} J_{ij}\sigma_i\sigma_j. \tag{2.15}$$

To derive the ground state of this Hamiltonian, QA exploits the time-dependent Hamiltonian below,

$$H(t) = H_0 + \Gamma(t)H_I, \tag{2.16}$$

where the parameter $\Gamma(t)$ is set to a sufficient large value initially and decreases in the course of the calculation. The Hamiltonian H_I is often referred to as the driver Hamiltonian which is a key of quantum annealing. The initial state $|\psi(t=0)\rangle$ is set to the ground state of H_I which is often chosen as the transverse magnetic field, [1)]

$$H_I = -\sum_i \sigma_i^x. \tag{2.17}$$

QA evolves the initial state with this time-dependent Hamiltonian $H(t)$ according to the time-dependent Schrödinger equation,

$$i\hbar\frac{\partial}{\partial t}|\psi(t)\rangle = H(t)|\psi(t)\rangle. \tag{2.18}$$

If the parameter $\Gamma(t)$ is decreased very slowly, the state $|\psi(t)\rangle$ keeps following the ground state of $H(t)$ and the desired solution is obtained finally. A similar discussion to the convergence of the probability in SA can be applied even to QA and the corresponding time schedule is

$$\Gamma(t) \sim a(\delta t + c)^{-1/(2N-1)}, \tag{2.19}$$

whose decreasing rate obeys the power law and is much faster than that of SA [44, 45]. This fact implies the superiority of QA to SA in the sense of the computational time.

One of the recent progresses of theoretical study of quantum annealing is introducing other types of driver Hamiltonian to accelerate the speed of obtaining the ground state of the Hamiltonian.

For instance, if we introduce the antiferromagnetic "XX" term Hamiltonian,

$$H_{XX} = \sum_{ij} \sigma_i^x\sigma_j^x, \tag{2.20}$$

[1)] In fact H_I does not have to be transverse magnetic field. We can choose any H_I as long as the relation $[H_0, H_I] \neq 0$ holds. Note that there is a method to eliminate the constrains in the combinatorial optimizations (e.g., terms (2.10), (2.11) in traveling salesman problem Hamiltonian) by choosing adaptive H_I so that the constrains is satisfied in principle throughout the process of quantum annealing. See [41–43] for more details.

where the total Hamiltonian becomes

$$H(t) = H_0 + \Gamma(t)H_I + \gamma(t)H_{XX}, \tag{2.21}$$

it has been shown theoretically by using mean-field analysis that the energy gap between the ground state and the first excited state Δ can be larger that the total Hamiltonian with transverse magnetic field with an appropriate choice of annealing schedule $\Gamma(t)$ and $\gamma(t)$ [46,47]. Taking the relation between the annealing time T to obtain the ground states with large probability and the energy gap Δ derived from adiabatic theorem,

$$T \gg \frac{1}{\Delta^2}, \tag{2.22}$$

into consideration, it can be said that the annealing time can be smaller than before by introducing this driver Hamiltonian.

2.3. Physical realization of quantum annealing and its application to quantum simulation

As explained in the introduction, this quantum annealing has been gaining attention due to the device which performs quantum annealing directly. This device utilizes the superconducting systems which can be regarded as an Ising model with transverse magnetic field especially in a low-lying excited state region. Technical details of the superconducting circuits in the D-Wave machine is elucidated in the paper [9] and the original Hamiltonian of this superconducting system is described in Eq (2) in [9]. [2)] The effective Hamiltonian in the D-Wave machine can be represented as a transverse field Ising system with the following terms,

$$H(s) = -\frac{A(s)}{2}\left(\sum_i \sigma_i^x\right) + \frac{B(s)}{2}\left(\sum_{\langle ij\rangle} J_{ij}\sigma_i^z\sigma_j^z + \sum_i h_i\sigma_i^z\right), \tag{2.23}$$

where s denotes an annealing schedule which moves from 0 to 1 during the annealing process. The coefficients $A(s)$ and $B(s)$ show the strength of the transverse field and the problem Hamiltonian, respectively, and the values are depicted in Fig. 2.3. The physical temperature is kept at 12mK inside the D-Wave machine. The coefficient of the transverse field $A(s)$ monotonically decreases while the coefficient of the problem Hamiltonian $B(s)$ increases as s increases, showing that the $s = 0$ and $s = 1$ correspond of the beginning and the ending of the annealing respectively. The result of spins $\boldsymbol{\sigma}$ which is measured with z-basis can be obtained at the end of each annealing process.

Although there is some evidence that the D-Wave machine really utilizes the quantum mechanical effect explicitly [10,11,48], its behavior is far from an ideal quantum annealing. If the D-Wave machine can perform ideal quantum annealing, the wave function during the annealing should obey the Schrödinger equation,

$$i\hbar\frac{d}{ds}|\psi(s)\rangle = H(s)|\psi(s)\rangle\,. \tag{2.24}$$

and the measured probability should represented as an overlap of the final wave function state,

$$P(\boldsymbol{\sigma}) = \langle\boldsymbol{\sigma}|\psi(s=1)\rangle\,. \tag{2.25}$$

[2)] We will not dig into the superconducting flux system any further in this thesis since it is sufficient to consider the approximated Hamiltonian Eq. (2.23) when discussing the D-Wave machine.

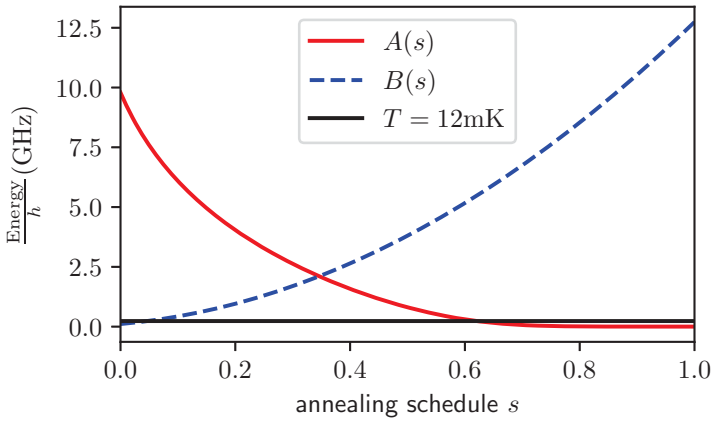

Figure 2.3.: The coefficients $A(s)$ (coefficient of the transverse magnetic field) and $B(s)$ (coefficient of the problem Hamiltonian) as a function of annealing schedule s. Black solid line shows the physical temperature in the D-Wave machine (12mK). The data is taken from the white paper in dwavesys.com.

Besides, there is considerable evidence that the outputs from the D-Wave machine can be explained by assuming the Boltzmann distribution,

$$P(\boldsymbol{\sigma}) = \frac{1}{Z} \exp\left[-\beta\left(\sum_{\langle ij\rangle} J_{ij}\sigma_i\sigma_j + \sum_i h_i\sigma_i\right)\right], \tag{2.26}$$

rather than the Schrödinger dynamics [16]. For that reason, using the D-Wave machine as a Boltzmann sampler comes to be regarded as one of the promising practical applications [16, 49, 50].

Although the previous studies focus on the use of the D-Wave machine as a sampler of the "classical" Boltzmann distribution Eq. (2.26), it has been revealed that a simple trick makes it possible to sample the "quantum" Boltzmann distribution [17, 18]. The trick is to add the "pause" process during the annealing. In the conventional quantum annealing, one sweeps the annealing schedule s linearly from 0 to 1,

$$s = \frac{t}{T}, \tag{2.27}$$

where t and T denote the elapsed time and the total annealing time, respectively. In the new idea one first sweeps s from 0 to a certain value s_* and apply a pause at the point $s = s_*$ for a while. Owing to this procedure, the system gets to the thermal equilibrium state in the presence of he transverse field,

$$P(\boldsymbol{\sigma}) \sim \frac{1}{Z} \exp\left[-\beta\left(-\frac{A(s_*)}{2}\left(\sum_i \sigma_i^x\right) + \frac{B(s_*)}{2}\left(\sum_{\langle ij\rangle} J_{ij}\sigma_i^z\sigma_j^z + \sum_i h_i\sigma_i^z\right)\right)\right]. \tag{2.28}$$

After the pause, one quenches s to 1 as quickly as possible to obtain a set of spins $\boldsymbol{\sigma}$ sampled from the quantum Boltzmann distribution. This protocol is often referred to as *anneal-pause-quench* protocol and will be elucidated in the next section in detail.

Though the hypothesis that anneal-pause-quench protocol can generate the quantum Boltzmann distribution is of course nontrivial, previous studies showed that the hypothesis seems to hold. A first example is the study by Harris et al. [17]. In this study they demonstrated the simulation of the quantum Boltzmann distribution of the three-dimensional quantum spin glass Ising model and they showed that the D-Wave quantum

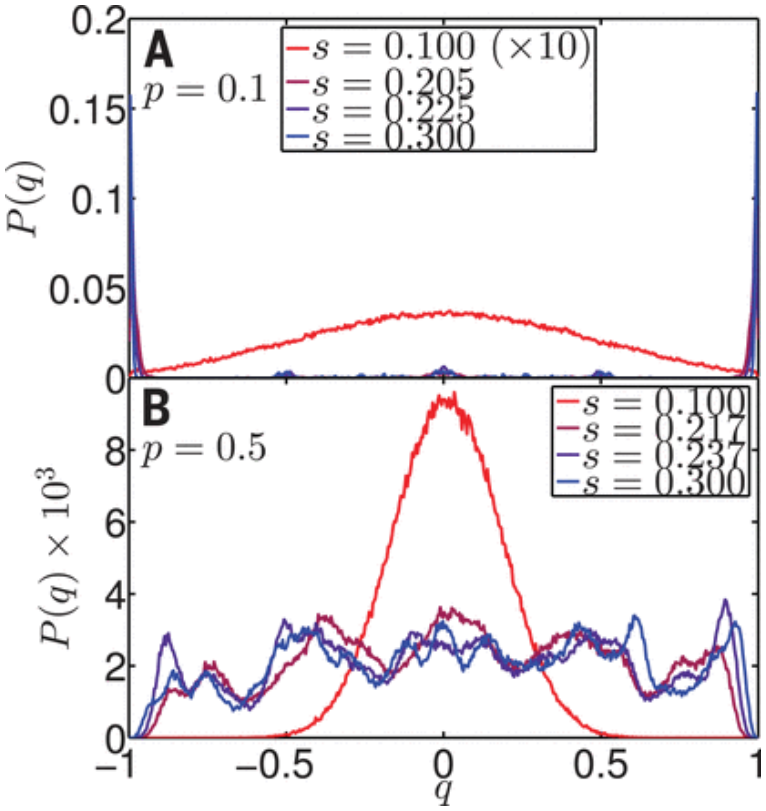

Figure 2.4.: Spin glass parameter q obtained from the D-Wave machine. The variable s in the figure corresponds to the pause point s_*. This figure is taken from [17] (Harris et al. "Phase transitions in a programmable quan- tum spin glass simulator", Science, 2019).

annealer can detect a quantum phase transition. Let us give a brief explanation of the derived result. The figure which captures the phase transitions in [17] is quoted and shown on Fig. 2.4. The variable s in the figure is the same as the pause point s_* during the anneal-pause-quench protocol. $P(q)$ shows the histogram of the overlap between spins q,

$$q = \frac{1}{N}\sum_{i=1}^{N} \sigma_i^A \sigma_i^B, \tag{2.29}$$

where σ_i^A and σ_i^B denote the ith spin from different samples (named A and B). The quantity $P(q)$ indicates what kind of phase the system is in. If the system is in the paramagnetic phase, $P(q)$ shows the Gaussian-like distribution with mean $q = 0$. If the system is in the ferromagnetic phase, $P(q)$ should have peaks at $\pm a (a \neq 0)$. The top panel of Fig. 2.4 shows the quantum phase transition from the paramagnetic phase to the ferromagnetic phase. As the pause point s_* increases from 0.1 to 0.3, which corresponds to decreasing the transverse field, we can clearly see that the system goes from the paramagnetic phase (indicated with the red solid line) to the ferromagnetic phase (indicated with blue solid line). The bottom panel of Fig. 2.4 shows the quantum phase transition from the paramagnetic phase to the spin glass phase which occurs in the presence of highly disordered interactions. Unlike the top panel of Fig. 2.4, $P(q)$ turns to the histogram with multiple peaks as the pause point s_* increases, which indicates that the system is in the spin glass phase. Also they showed that the result of the quantum phase transition point is consistent to the previous studies with quantum Monte Carlo method [51].

Quantum simulation with more complicated model has also been performed in [18] where they demonstrate the Kosterlitz-Thouless transition on the D-Wave machine by mapping

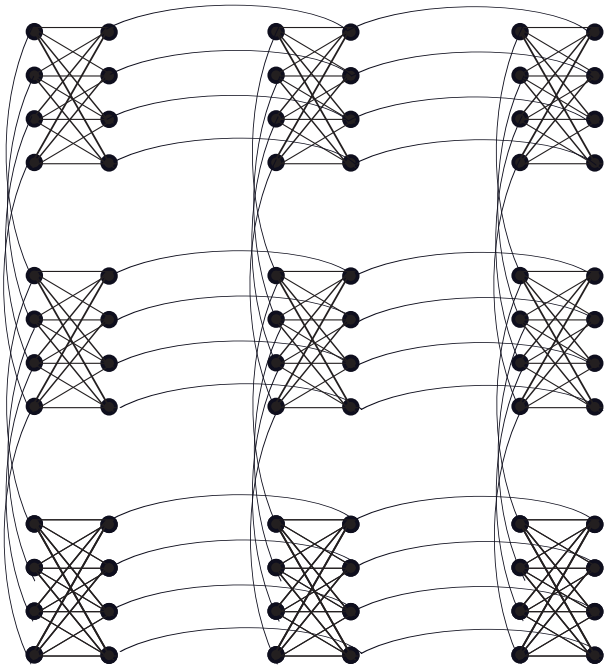

Figure 2.5.: A schematic diagram of the chimera graph on the D-Wave machine. Each chimera unit consists of eight spins. This figure contains 3×3 chimera units ($3 \times 3 \times 8$ Ising spins).

multiple Ising spins into a single clock-model spin. The techniques used in the study is almost the same as the previous one.

It can be said that the anneal-pause-quench protocol may be useful as a versatile tool for simulating quantum mechanical thermal equilibrium state.

2.4. An overview of the D-Wave machine

In the previous section we mainly introduced the previous researches of the quantum simulation on the D-Wave machine. In this section we give a detailed explanation of the practical use of the D-Wave machine from technical perspective. More specifically, we introduce the parameter that can be set on the D-Wave machine which is quite relevant to this study and two important features, anneal-pause-quench and independent control of longitudinal field.

2.4.1. Interfaces and parameters

The main flow of the use of the D-Wave machine is quite simple: specify the interactions J_{ij} and h_i and send the query to the machine. After receiving the query, the D-Wave machine performs the annealing with given interactions and returns the measurement result $\boldsymbol{\sigma} = \{\pm 1\}$ for each annealing process. Owing to the connectivity of the superconducting flux qubits in the device, the connectivity is restricted to what is called the "chimera" graph as described on Fig. 2.5 where each set of eight spins consists of a single bipartite graph which is referred to as the chimera unit. If we want to carry out a computation with a different topology, we have to map the structure of the topology into this chimera graph.

One of the most important tunable parameters for quantum simulation is the interval for each annealing process. To see this let us focus on Fig. 2.6 which shows the annealing process inside the D-Wave machine. After receiving a query, the D-Wave machine starts to install the interactions to the superconducting flux qubits, which is indicated by a

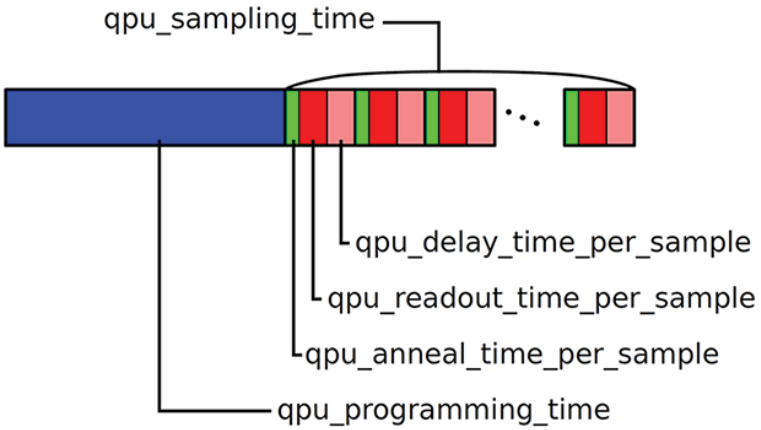

Figure 2.6.: A schematic diagram of the procedure of annealing process inside the D-Wave machine. This figure is taken from docs.dwavesys.com/docs/latest/c_timing_2.html. Green rectangles show the annealing time and the interval between each annealing process is indicated by red and pink rectangles, whose length can be adjusted by using the parameter "readout_thermalization" on the D-Wave machine.

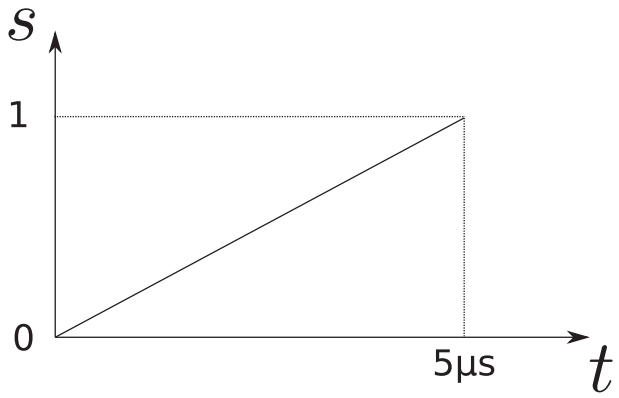

Figure 2.7.: Linear annealing schedule specified by the list $[(0,0),(5,1)]$. s represents the annealing schedule and t shows the actual elapsed time (μs).

blue rectangle in Fig. 2.6. After setting the interactions, the machine starts to repeat the annealing processes for specified times. The bunch of green, red, and pink rectangles represents a single annealing process and the red and pink ones show the interval between the annealing process. If the interval is set too short, the spins for each samples tend to correlate each other. Hence the interval should be set as long as possible, which can be adjusted by using optional variable "readout_thermalization" on the D-Wave machine.

2.4.2. Anneal-pause-quench protocol

Next we explain the setting of the annealing schedule. The annealing schedule on the D-Wave machine can be specified by passing a list of tuples of the elapsed time t and annealing schedule s. For example, if we set schedules like $[(0,0),(5,1)]$, this means that annealing schedule is linearly changed from $s=0$ to $s=1$ in 5μs. The schematic figure is shown on Fig. 2.7. If we set schedules like $[(0,0),(5,0.6),(20,1)]$, it follows that the annealing schedule s is first linearly changed from $s=0$ to $s=0.6$ in 5μs, and then changed to $s=1$ in 15μs. The total elapsed time of the example is 20μs.

A schematic diagram of the anneal-pause-quench schedule is shown on Fig. 2.8 where the corresponding list is $[(0,0),(t_1,s_*),(t_2,s_*),(t_f,1)]$. The elapsed time of anneal, pause,

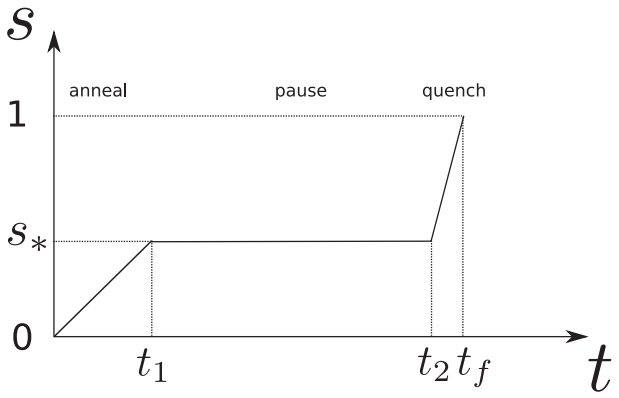

Figure 2.8.: A schematic diagram of anneal-pause-quench schedule. The notation is the same as Fig. 2.7.

and quench are t_1, $t_2 - t_1$, $t_f - t_2$ μs respectively. Since current D-Wave machine requires the annealing schedule s to be unity at the end of the annealing, the quench process is inevitable even though it is not essential. Hence the elapsed time of the quench process $t_f - t_2$ should be set as small as possible. By applying this anneal-pause-quench protocol, it is expected that the system goes to the thermal equilibrium state with $s = s_*$.

2.4.3. Independent control of longitudinal magnetic field

One of the important physical quantities is the susceptibility which is defined as a derivative of the magnetization as a function of longitudinal magnetic field h,

$$\chi = \left.\frac{\partial m}{\partial h}\right|_{h\to 0} \tag{2.30}$$

In fact, as explained in the next chapter, the susceptibility has an important role of investigating the main theme of this thesis, the Griffiths-McCoy singularity. This physical quantity can be observed via the D-Wave quantum annealer by adding a longitudinal magnetic field in the course of quantum annealing. With this function activated, the amplitude of longitudinal magnetic field can be controlled which is independent of annealing schedule. The Hamiltonian can hence be rewritten by

$$H(s) = -\frac{A(s)}{2}\left(\sum_i \sigma_i^x\right) + \frac{B(s)}{2}\left(\sum_{\langle ij\rangle} J_{ij}\sigma_i^z\sigma_j^z + \Phi(t)\sum_i h_i\sigma_i^z\right), \tag{2.31}$$

where $\Phi(t)$ controls the amplitude of h_i independently to the annealing schedule s. The schematic diagram of the annealing in the presence of $\Phi(t)$ is on Fig. 2.9. By repeating the annealing process with changing the amplitude of $\Phi(t)$, we can derive the magnetization dependence as a function of longitudinal magnetic field. An example is shown on Fig. 2.10. One can obtain the linear susceptibility χ and the nonlinear susceptibility $\chi_{\rm nl}$,

$$\chi_{\rm nl} = -\frac{1}{6}\left.\frac{\partial^3 m}{\partial h^3}\right|_{h\to 0}, \tag{2.32}$$

by applying a polynomial fit to the magnetization as

$$m \sim \chi h - \chi_{\rm nl} h^3 + \cdots. \tag{2.33}$$

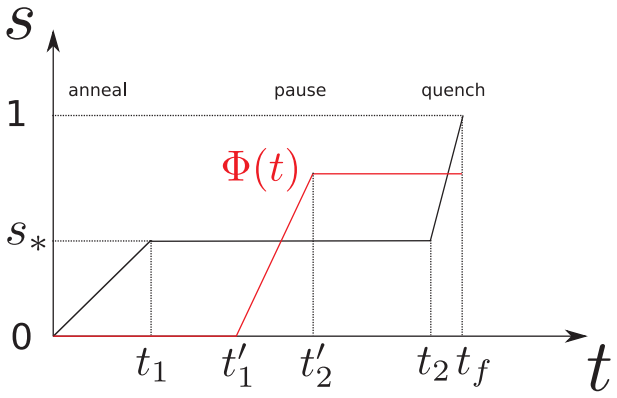

Figure 2.9.: A schematic diagram of anneal-pause-quench schedule in the presence of $\Phi(t)$. This schedule is depicted with the red line and can be controlled independently to the annealing schedule.

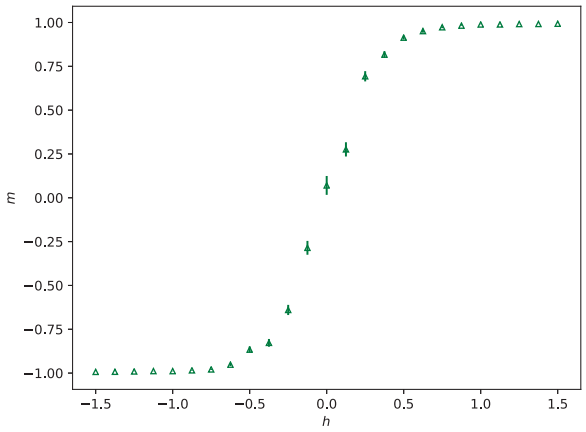

Figure 2.10.: Magnetization as a function of the longitudinal magnetic field obtained from the D-Wave quantum annealer by using the technique explained above. The range of the amplitude of $\Phi(t)$ at the end of annealing $t = t_f$ is from -1.5 to 1.5 and all local fields h_i are set to -0.02. The horizontal axis corresponds to $\Phi(t_f)$. Linear (and nonlinear) susceptibility can obtained from the plot by applying a polynomial fit (2.33).

2.5. Summary

In this chapter we gave an introduction to quantum annealing starting with the explanation of the spin glass Ising model. We also showed that the notable previous studies of the use of the D-Wave quantum annealer as a quantum Boltzmann sampler. In the last section we demonstrate the technical details of the use of the D-Wave machine, especially how to use this machine as a quantum simulator and the method to obtain the susceptibilities.

Note that the environment noise is also a significant problem for the D-Wave machine since it is in principle an analog device. Therefore the technique to mitigate noise is also needed to obtain more reliable results from the D-Wave machine. Throughout the experiments, we apply two types of which is described in detail in Appendix D.

3. Griffiths-McCoy singularity

In this chaper we introduce the background of the Griffiths singularity — a singularity which occurs on a diluted Ising lattice. We show that emergence of Griffiths singularity is quite different between classical and quantum Ising model and see what kind of behavior is caused by this singularity.

3.1. Classical Griffiths singularity

Phase transition is one of the most important traits in statistical physics. In the classical Ising model,

$$H = \sum_{\langle i,j \rangle} J_{ij}\sigma_i\sigma_j - h\sum_i \sigma_i \ (\sigma = \pm 1), \tag{3.1}$$

a phase transition occurs at a certain temperature [1)] if the dimension of the Ising model is two or more and the local field h is set to 0. It has been well established that the Ising model with uniform ferromagnetic interactions ($J_{ij} = J(< 0)$) has two phases: namely the ferromagnetic phase where magnetization has a finite value and the paramagnetic phase where spins are thermally fluctuating and completely disordered. In the case of the spin glass Ising model (Ising model with random interactions), there would be another phase: the spin glass phase where spins are disordered but thermally frozen. This phase can be observed when the system is in low temperature and the amplitude of random interactions, which can be characterized theoretically as a variance of the distribution $P(J_{ij})$, is large.

In 1969, Griffiths proposed a new type of phase which appears in a randomly diluted Ising ferromagnetic model [52]. This phase exists at a certain region inside the paramagnetic phase $T_c < T < T_c^*$ as denoted in Fig. 3.1. He also claimed that in this region the magnetization is not an analytic as a function of local field h at $h = 0$.

Here we show the statement in more detail. The dilute model can be characterized by introducing a probability p. For each bond $\langle i, j \rangle$, where $\langle i, j \rangle$ denotes the nearest neighbor

[1)] This temperature is often called the transition point or the critical point and denoted as T_c.

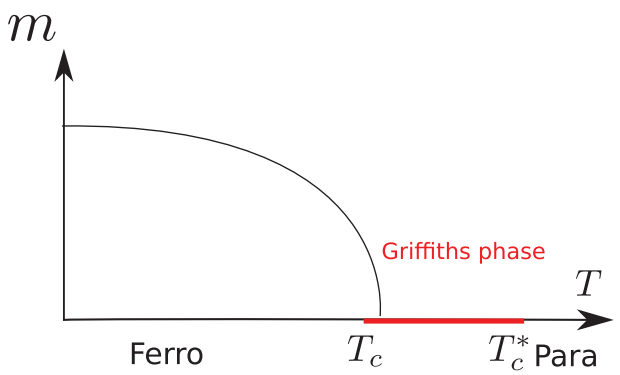

Figure 3.1.: A schematic diagram of the Griffiths singularity. Even if the system in paramagnetic phase $T_c < T$, there exists a singularity in the region where the magnetization is not an analytic function.

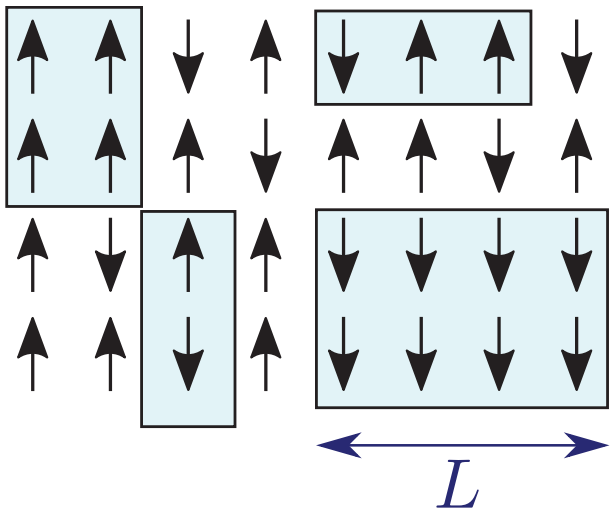

Figure 3.2.: A schematic figure representing clusters (a set of spins connected by ferromagnetic interactions in the percolated model) which are denoted by light-blue colored rectangles. Even if the system is globally in the paramagnetic phase, owing to these clusters the Griffiths singularity emerges. The length of each cluster is denoted as L in main text.

connectivity, J_{ij} takes a ferromagnetic value with probability p and takes zero with the probability $1-p$.

$$P(J_{ij}) = p\delta_{J_{ij},J} + (1-p)\delta_{J_{ij},0} \tag{3.2}$$

The probability $p = 1$ corresponds to the ordinary ferromagnetic Ising model.

The main claim of this study is as follows: at any temperature below the critical point of the ordinary Ising ferromagnetic model the magnetization is not an analytic function of local field h at $h = 0$. That is, there will be a singularity in the region $T_c < T < T_c^{\text{ferro}}$ where T_c^{ferro} is a critical point of ferromagnetic Ising model ($p = 1$).

For simplicity we first focus on the case that the probability p is small enough [2)] to assume that the total magnetization m can be represent as a sum of "local" magnetization $m(\psi)$ for each cluster region (see the schematic figure in Fig. 3.2),

$$\begin{aligned} m &= \frac{1}{N}\sum_i \sigma_i \\ &= \sum_{\{\psi\}} \frac{\nu(\psi)}{N} \frac{1}{\nu(\psi)} \sum_{i\in\psi} \sigma_i \\ &= \sum_{\{\psi\}} p(\psi) m(\psi), \end{aligned} \tag{3.3}$$

where ψ is a set of spins (cluster) and the quantity $\nu(\psi)$ shows the number of spins in a cluster ψ. The probability $p(\psi)$ is a ratio of $\nu(\psi)$ to the number of total spins N.

The magnetization $m(\psi)$ can also be represented as a differentiation of free energy, [3)]

$$m(\psi) = -\frac{1}{\nu(\psi)} \frac{\partial}{\partial h} \left(-\frac{1}{\beta} \log Z \right). \tag{3.4}$$

[2)] In other words the connectivity of the model is quite sparse.

[3)] For simplicity we assume that the local field h is applied only to spins with index $i \in \psi$.

Using the expansion of the partition function with respect to the parameter $z = e^{-2\beta h}$ shown below:

$$\begin{aligned} Z &= \sum_{\boldsymbol{\sigma}} \exp\left[-\beta \sum_{\langle i,j\rangle} J_{ij}\sigma_i\sigma_j + h\sum_{i\in\psi}\sigma_i\right] \\ &= e^{\beta\nu(\psi)h}\left(a_0 + a_1 e^{-2\beta h} + a_2 e^{-4\beta h} + \cdots + a_{\nu(\psi)} e^{-2\nu(\psi)\beta h}\right) \\ &= e^{\beta\nu(\psi)h}\left(a_0 + a_1 z + a_2 z^2 + \cdots + a_{\nu(\psi)} z^{\nu(\psi)}\right) \\ &= e^{\beta\nu(\psi)h} a_{\nu(\psi)} \prod_{i\in\psi}(z-\xi_i), \end{aligned} \tag{3.5}$$

where $\xi_i (i \in \psi)$ are complex variables which satisfy the equation $a_0 + a_1 z + a_2 z^2 + \cdots + a_{\nu(\psi)} z^{\nu(\psi)} = 0$ and the Lee-Yang circle theorem [53] ensures $|\xi_i| = 1$, the magnetization can be rewritten as

$$m(\psi) = 1 + \frac{2z}{\nu(\psi)} \sum_{i\in\psi} \frac{1}{\xi_i - z}. \tag{3.6}$$

It follows that $m(\psi)$ is an analytic function in the region $|z| < 1$ and fails to be analytic when z crosses the accumulating point of ξ_i.

Next consider a set of the cluster depicted in Fig. 3.2. For each cluster with finite system size the magnetization $m(\psi)$ is an analytic function of z as far as the local field h is a real variable since ξ is located away from real axis. [4)] In the case of thermodynamic limit ($N \to \infty$), the set of ξ_i starts to cover the real axis as the temperature goes near the critical point of ordinary ferromagnetic Ising model T_c^{ferro}, which leads to a singular behavior of the magnetization (3.6) near $h = 0$. This means even if the temperature is above the transition point of diluted Ising model T_c and whole system is in paramagnetic phase, there might be a non-analytical behavior of the magnetization $m(\psi)$ unless the temperature is above T_c^{ferro} due to the existence of the cluster.

One may wonder if such a relatively huge cluster can really be generated from the distribution $P(J_{ij})$ in (3.2). The probability of generating a certain volume (say L^d in d dimensional lattice) of cluster can be estimated as $\exp(-cL^d)$. [5)] It follows that the probability is exponentially small, which is the reason that this kind of cluster is often called a *rare region*. Since the susceptibility for each cluster χ_{cluster} grows $\sim L^d$ as a function of cluster size, [6)] the total susceptibility in the system will be [25]

$$\chi = \int dL^d \exp(-cL^d)\chi_{\text{cluster}} \sim \int dL^d \exp(-cL^d) L^d, \tag{3.7}$$

leading to an exponential decay as the system size increases.

The above discussion indicates that in the classical Ising model, even if there is a non-analytical behavior of the susceptibility, this kind of singularity is quite difficult to be

[4)] If there exists $\xi_i \in \mathbb{R}$ with finite system size, the partition function Z takes zero at the point $z = e^{-2\beta h} = \xi_i$, which must not happen as can be confirmed from the definition of Z.

[5)] One can confirm the statement by using the fact that the probability of generating a cluster with the volume $V_1 + V_2$, $P(V_1 + V_2)$ is the product of the probability with the volume V_1 and V_2: $P(V_1 + V_2) = P(V_1)P(V_2)$.

[6)] Note that the susceptibility can be represented with spins as

$$\chi_{\text{cluster}} = \frac{\beta}{\nu(\psi)}\left[\left\langle\left(\sum_{i\in\psi}\sigma_i\right)^2\right\rangle - \left\langle\sum_{i\in\psi}\sigma_i\right\rangle^2\right]$$

.

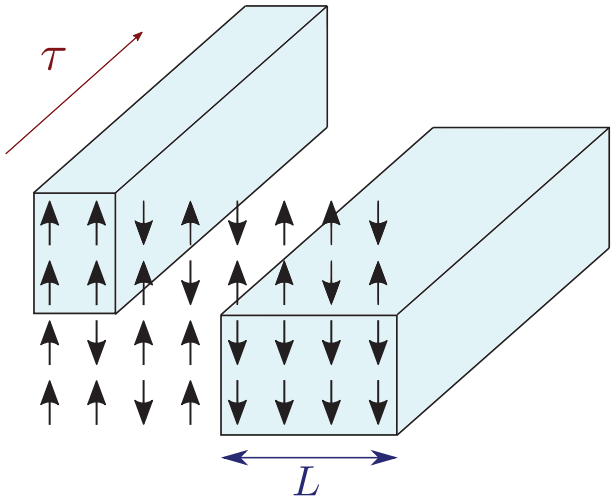

Figure 3.3.: A schematic figure representing clusters with the Trotter dimension. Each cluster is extended to an extra dimension of imaginary time denoted as τ.

observed since the probability of appearance of large cluster, which mainly contributes the singularity, is exponentially small.

In the next section we see that this situation is quite changed if we consider the "quantum" counterpart of Griffiths singularities.

3.2. Quantum Griffiths singularity: Griffiths-McCoy singularity

3.2.1. Enhancement of Griffiths singularity by quantum effects

Consider the quantum counterpart of the diluted Ising model — the transverse Ising model where a transverse magnetic field term is added to the classical Ising model as

$$H = \sum_{\langle i,j \rangle} J_{ij} \hat{\sigma}_i^z \hat{\sigma}_j^z - h \sum_i \hat{\sigma}_i^z - \Gamma \sum_i \hat{\sigma}_i^x. \tag{3.8}$$

Similarly to the classical phase transition, the model goes from the ferromagnetic phase to the paramagnetic phase as Γ crosses a certain value Γ_c at the zero temperature limit ($\beta \to \infty$) in the absence of longitudinal magnetic field h.

This model can be mapped onto a corresponding classical Ising model by using the Suzuki-Trotter decomposition (see Appendix A). The corresponding model has $d+1$ dimensions compared to the original one of the transverse field Ising model and the interactions J_{ij} take the same value throughout the Trotter direction as depicted in the schematic figure Fig. 3.3. This property makes the behavior of physical quantities (say, the susceptibility) change drastically.

Next let us consider the behavior of the local susceptibility in the Griffiths region ($\Gamma_c < \Gamma < \Gamma_c^{\text{ferro}}$) where Γ_c^{ferro} is the critical point of ordinary (ferromagnetic) transverse Ising model. Figure 3.4 shows a cluster with Trotter dimension. Since each Trotter slice is connected by ferromagnetic interactions, each cluster can be regarded as the classical one-dimensional Ising model with ferromagnetic interactions along the Trotter direction,

$$H_{\text{cluster}} = -\sum_{\tau=0}^{\beta} J_{\text{eff}} S_\tau S_{\tau+1}. \tag{3.9}$$

The effective interaction J_{eff} of this Ising model is proportional to the volume of each

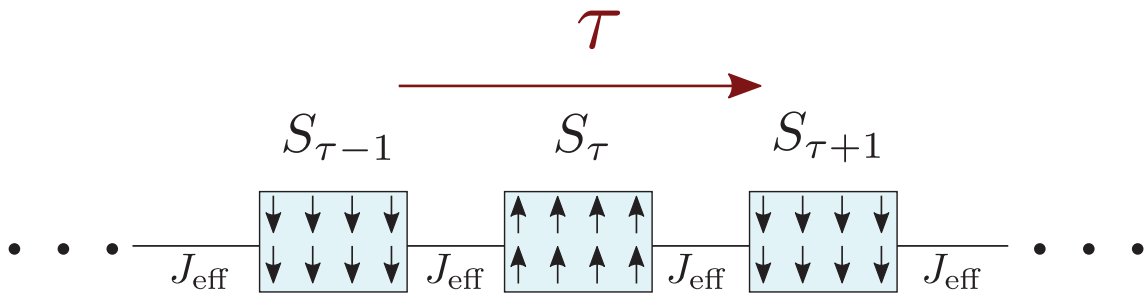

Figure 3.4.: A schematic diagram of a cluster with Trotter dimension. Since each Trotter slice is connected by ferromagnetic interactions, if we assume that the spins have the same direction in each Trotter slice, the cluster can be regarded as a one-dimensional Ising model Eq. (3.9) with an effective interaction $J_{\text{eff}} \sim L^d$ and effective spins S_τ, where L^d is a volume of each Trotter slice in the cluster.

rare region $J_{\text{eff}} \sim L^d$. [7] Hence the susceptibility grows exponentially as the cluster size increases ($\chi_{\text{cluster}} = \beta e^{2\beta J_{\text{eff}}} \sim e^{aL^d}$). [8] The total susceptibility can then diverge as the system size increases,

$$\chi \sim \int dL^d \exp(-cL^d)\chi_{\text{cluster}} \sim \int dL^d \exp(-cL^d)e^{aL^d}, \tag{3.10}$$

compared to Eq.(3.7) where the susceptibility decays exponentially. This result implies that the quantum effect can enhance the Griffiths singularity.

This phenomenon was first discovered by McCoy and Wu [54], which is the origin of the name of the "Griffiths-McCoy singularity". [9]

3.2.2. Power-law distribution

One of the notable features of the quantum Griffiths singularity is the emergence of a "power-law distribution" which affects the behavior of some physical quantities.

Since the susceptibility for each cluster behaves e^{aL^d} and the energy gap Δ is typically inverse of the susceptibility, [10] the energy gap decays exponentially as a function of cluster size, [11]

$$\Delta \sim e^{-aL^d}. \tag{3.12}$$

Next we introduce the density of states which typically have the energy gap Δ, $\rho(\Delta)$, which plays an important role in the theory. This quantity can be determined by rewriting the probability of generating the cluster with size between L^d and $L^d + dL^d$, $e^{-cL^d}dL^d$, to

[7] Remember that L denotes the length of each cluster.

[8] The equation $\chi_{\text{cluster}} = \beta e^{2\beta J}$ comes from the susceptibility of ferromagnetic one-dimensional Ising model.

[9] They performed the analysis not on a quantum model but on a classical two-dimensional anisotropic Ising model whose interactions are correlated in one direction (often referred to as McCoy-Wu model), which can be regarded as a one-dimensional transverse Ising model mapped into effective classical Hamiltonian by using Suzuki-Trotter formalization.

[10] Note that the susceptibility can be represented as

$$\chi \sim \frac{1}{N}\sum_{n\neq 0}\frac{2}{E_n - E_0}\langle 0|\sum_{i=1}^{N}\sigma_i^z|n\rangle\langle n|\sum_{j=1}^{N}\sigma_i^z|0\rangle \tag{3.11}$$

by using spectral decomposition. Δ corresponds to $E_1 - E_0$.

[11] From now we only consider clusters whose energy gaps Δ are sufficiently small so that the coefficient of e^{-aL^d} can be ignored.

a probability of generating cluster with the energy gap between Δ and $\Delta + d\Delta$, $\rho(\Delta)d\Delta$, as shown below:

$$\begin{aligned} e^{-cL^d} dL^d &= e^{-cL^d} \frac{\partial L^d}{\partial \Delta} d\Delta \\ &= e^{-cL^d} \frac{\partial}{\partial \Delta} \left(-\frac{1}{a} \log \Delta \right) d\Delta \\ &= e^{-cL^d} \left(-\frac{1}{a\Delta} \right) d\Delta \\ &\sim e^{-cL^d} e^{aL^d} d\Delta \\ &= \Delta^{\lambda - 1} d\Delta, \end{aligned} \tag{3.13}$$

where $\lambda = c/a$ and we use Eq.(3.12) in the course of derivation. It follows that $\rho(\Delta)$ has a power-law distribution as a function of Δ, namely $\Delta^{\lambda-1}$.

Some important results can be derived from the above relation [24, 25]. Assume that the small longitudinal magnetic field h is applied to the system uniformly. The rare region whose energy gap is smaller than h will be completely polarized while the region whose energy gap is larger than h will not be affected by the magnetic field. Hence the total magnetization is expected to response as

$$m \sim \int_0^h d\Delta \ \rho(\Delta) \sim h^\lambda. \tag{3.14}$$

in the small limit of h.

The linear and nonlinear susceptibility (χ, $\chi_{\rm nl}$) can also be represented as

$$\chi = \frac{\partial m}{\partial h} \sim h^{\lambda - 1}, \tag{3.15}$$

$$\chi_{\rm nl} = \frac{\partial^3 m}{\partial h^3} \sim h^{\lambda - 3}, \tag{3.16}$$

leading to a divergence when $\lambda < 1$ (linear susceptibility) and $\lambda < 3$ (nonlinear susceptibility). In the case of low temperature T, since the cluster with energy gap smaller than T can be assumed to contribute, the dependence of the linear susceptibility as a function of temperature is determined as

$$\begin{aligned} \chi &\sim \int_0^T \chi_{\rm cluster} \rho(\Delta) d\Delta \\ &\sim \int_0^T \frac{1}{\Delta} \rho(\Delta) d\Delta \\ &= T^{\lambda - 1}, \end{aligned} \tag{3.17}$$

$$\tag{3.18}$$

and a similar relation holds in the nonlinear susceptibility:

$$\chi_{\rm nl} \sim T^{\lambda - 3}, \tag{3.19}$$

leading to the same divergence as for the case of h.

The quantity λ itself comes from the ratio of the exponents between the probability of forming clusters e^{-cL^d} and the energy gap of each cluster $\Delta = e^{-aL^d}$ and depends on the strength of the transverse magnetic field Γ. According to Fisher [55] who reaches the same conclusion of the power-law distribution by demonstrating renormalization group analysis on the one-dimensional transverse random Ising model, the inverse of λ can interpreted as

a kind of "dynamical exponent" since it relates a length scale l to a time scale τ as $\tau \sim l^{d/\lambda}$, which is reminiscent of the ordinary dynamical critical exponent z, $\tau \sim l^z$. Hereafter we denote λ as d/z' [12] and the above relations are rewritten as follows:

$$m \sim h^{d/z'}. \tag{3.20}$$

$$\chi \sim h^{d/z'-1}, \tag{3.21}$$

$$\chi_{\rm nl} \sim h^{d/z'-3}, \tag{3.22}$$

$$\chi \sim T^{d/z'-1}, \tag{3.23}$$

$$\chi_{\rm nl} \sim T^{d/z'-3}. \tag{3.24}$$

Fisher's renormalization analysis also figured out that the z' goes to zero as Γ closes to the critical point of the ferromagnetic model $\Gamma \to \Gamma_c^{\rm ferro}$ and $z' \to \infty$ in the limit of critical point $\Gamma \to \Gamma_c$. [13]

A computational procedure to determine d/z' on a numerical calculation is first proposed by Rieger and Young [21,22]. The probability of generating cluster with local susceptibility between $\chi_{\rm loc}$ and $\chi_{\rm loc} + d\chi_{\rm loc}$ can be obtained as

$$P(\chi_{\rm loc}) \sim \chi_{\rm loc}^{-d/z'-1}, \tag{3.25}$$

or

$$\log P(\chi_{\rm loc}) \sim -\left(\frac{d}{z'}+1\right)\log \chi_{\rm loc}, \tag{3.26}$$

by applying a similar discussion to Eq. (3.13),

$$\begin{aligned} e^{-cL^d}dL^d &= e^{-cL^d}\frac{\partial L^d}{\partial \chi_{\rm loc}}d\chi_{\rm loc} \\ &\sim e^{-cL^d}e^{-aL^d}d\chi_{\rm loc} \\ &= \chi_{\rm loc}^{-\lambda-1}d\chi_{\rm loc} \\ &= \chi_{\rm loc}^{-d/z'-1}d\chi_{\rm loc} \\ &= P(\chi_{\rm loc})d\chi_{\rm loc}. \end{aligned} \tag{3.27}$$

Taking the logarithm of $P(\chi_{\rm loc})$ leads to [14]

$$\begin{aligned} \log \tilde{P}(\log \chi_{\rm loc}) &= \log P(\chi_{\rm loc}) + \log \chi_{\rm loc} \\ &\sim -\frac{d}{z'}\log \chi_{\rm loc}. \end{aligned} \tag{3.28}$$

The above relation shows that the $\tilde{P}(\log \chi_{\rm loc})$ roughly obeys a power-law as a function of $\chi_{\rm loc}$ on a log-log plot and d/z' can be obtained as the slope on a histogram of $\tilde{P}(\log \chi_{\rm loc})$.

The procedure proposed by Rieger and Young is shown below:

[12] The prime on z is to distinguish from ordinary dynamical exponents in statistical physics.

[13] Though his analysis is performed on the one-dimensional model, the result seems to be expected to be applicable roughly in general. Besides, a counterexample of this conjecture has also been discovered. For instance, Rieger and Young [21] claimed that z' converges to a finite value at the limit of criticality in the case of higher dimensional model.

[14] The tilde on $\tilde{P}(\log \chi_{\rm loc})$ is to indicate that this distribution has a different measure to $P(\chi_{\rm loc})$. More precisely, the following equality,

$$\int \tilde{P}(\log \chi_{\rm loc}) d\log \chi_{\rm loc} = \int P(\chi_{\rm loc}) d\chi_{\rm loc} = 1,$$

leads to a relation $\tilde{P}(\log \chi_{\rm loc}) = \chi_{\rm loc} P(\chi_{\rm loc})$.

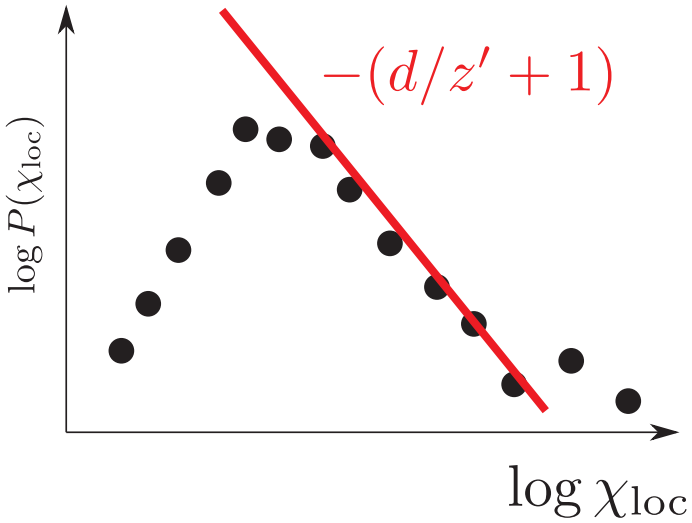

Figure 3.5.: A schematic diagram of extracting d/z' from the log-log plot of local susceptibilities. Red solid line shows the slope whose value corresponds to $-(d/z'+1)$. Since the theory is applicable especially to small energy gap (large susceptibilities), The data should be fit around the large region of the susceptibility.

1. Calculate local susceptibilities for each random instance and site and gather the data.

2. Plot a log-log histogram of $\tilde{P}(\log \chi_{\rm loc})$.

3. Apply a linear fitting on the data. The estimated slope corresponds to $-d/z'$.

One can also use the log-log plot of $P(\chi_{\rm loc})$ versus $\chi_{\rm loc}$, whose slope is expected to be $-(d/z'+1)$. The schematic figure of histogram is in Fig. 3.5.

A procedure which gives better statistics is suggested by Ikegami, Miyashita and Rieger [26]. They use integrated distribution function $I(\chi_{\rm loc})$ instead of $\tilde{P}(\log \chi_{\rm loc})$ which gives the same power-law relation as shown below,

$$I(\chi_{\rm loc}) = \int_{\chi_{\rm loc}}^{\infty} P(\chi_{\rm loc}) d\chi_{\rm loc} \sim \frac{z'}{d} \chi_{\rm loc}^{-d/z'}, \tag{3.29}$$

and taking logarithm of both sides gives

$$\log I(\chi_{\rm loc}) \sim -\frac{d}{z'} \log \chi_{\rm loc}. \tag{3.30}$$

In the case of the nonlinear local susceptibility $\chi_{\rm nlloc}$, we can assume that $\chi_{\rm nlloc}$ behaves as $(\chi_{\rm loc})^3$ since it contains the triple integral with respect to the imaginary time [21], leading to

$$\log P(\chi_{\rm nlloc}) \sim \left(-\frac{d}{3z'} - 1\right) \log \chi_{\rm nlloc}, \tag{3.31}$$

or

$$\log \tilde{P}(\log \chi_{\rm nlloc}) \sim -\frac{d}{3z'} \log \chi_{\rm nlloc}. \tag{3.32}$$

3.3. Summary

In this chapter we give a historical review of the Griffiths-McCoy singularity. Since this singularity can only be observed clearly in the presence of quantum effects, it is of great significance to demonstrate the phenomena on the D-Wave quantum annealer. To observe the effect, we also show that the histogram of susceptibilities can be a reasonable indicator for detecting divergence caused by the singularity.

The following chapters show our main study. We perform the demonstration of the Griffiths-McCoy singularity of the quantum system using both quantum Monte Carlo method and the D-Wave device.

4. Quantum Monte Carlo simulation

In the previous chapter we introduced a background of (classical and quantum) Griffiths singularities, divergences of certain physical quantities induced by the singularities, and methods to compute the exponent d/z' numerically. Remember that before demonstrating Griffiths effect on a quantum annealer, we need to prepare a "reference" — results calculated on a classical computer with the same models and parameters to assure that the derived results from the annealer is consistent with the ones from conventional computers. Since there are no previous quantum Monte Carlo studies which demonstrate Griffiths singularities on the D-Wave machine chimera graph, we first start with a Monte Carlo simulation on a transverse Ising model on the chimera graph

$$H = \sum_{\langle i,j \rangle} J_{ij} \hat{\sigma}_i^z \hat{\sigma}_j^z - \Gamma \sum_i \hat{\sigma}_i^x. \tag{4.1}$$

then run the D-Wave machine.

Here we introduce the models and methods for the calculation and show the results in this chapter.

4.1. Models and methods

Since the D-Wave machine has a chimera connectivity, it will be convenient to run a simulation on a classical computer with a chimera topology to compare both results directly. [1)] We employ the "sparse" Chimera graph as depicted in Fig 4.1 to reduce the dimensionality of the lattice which is expected to be feasible for detecting the Griffiths effect clearly. As for the distribution of J_{ij}, the choice of the distribution of interactions may not be relevant to the emergence of the Griffiths effect following the discussion by Griffiths [52] and previous studies show that the distribution need not to be a binary distribution Eq. (3.2). For these reasons we set the interactions J_{ij} following the discretized uniform ferromagnetic distribution,

$$P(J_{ij}) = \frac{1}{6} \sum_{k=0}^{5} \delta(J_{ij} + 0.2k), \tag{4.2}$$

i.e, J_{ij} is randomly chosen from the set $\{0, -0.2, -0.4, -0.6, -0.8, -1.0\}$.

We perform quantum Monte Carlo simulation based on the Suzuki-Trotter decomposition with parameters listed on Table. 4.1. [2)] The total number of spins we deal with for each Monte Carlo step is $L \times L \times 8 \times M \times N_\beta \times N_\Gamma$. For each random instance, we store the following thermal-averaged physical variables:

[1)] Embedding the square or the cube-lattice on the D-Wave chimera graph might be an alternative approach as demonstrated in [17,18] since it enables us to compare the obtained results to previous Monte Carlo results from the previous quantum Monte Carlo study directly. Nevertheless we decided to avoid embedding since it may obscure the cause of calculation errors, i.e., we cannot figure out whether the error comes from the factor related to analog noise on the quantum annealer or the error is caused by embedding if we receive doubtful results.

[2)] Although the number of the Trotter slices M is fixed to 150, we performed the same calculation with $M = 100$ and obtained almost the same properties (e.g. the location of the critical point) of the system.

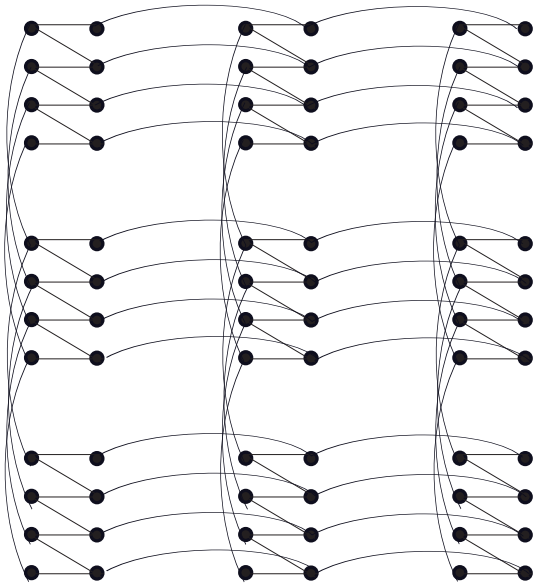

Figure 4.1.: A connectivity of sparse chimera graph. The figure contains 3×3 chimera units ($3 \times 3 \times 8$ Ising spins).

Table 4.1.: Parameters for quantum Monte Carlo method

# of random instances N_{rand}	200
# of Trotter slices M	150
system size N	$L \times L \times 8$ ($L = 6, 8, 10, 12$)
number of Monte Carlo steps	2^{20}
maximum value of inverse temperature β_{max}	50
minimum value of inverse temperature β_{min}	2.5
# of inverse temperatures N_β	10
minimum value of transverse field Γ_{min}	1.4
maximum value of transverse field Γ_{max}	2.135
# of transverse fields N_Γ	50

- absolute total magnetization $\langle |m| \rangle = \left\langle \left| \frac{1}{NM} \sum_{i=1}^{N} \sum_{t=1}^{M} \sigma_i(t) \right| \right\rangle$,
- squared total magnetization $\langle m^2 \rangle = \left\langle \left(\frac{1}{NM} \sum_{i=1}^{N} \sum_{t=1}^{M} \sigma_i(t) \right)^2 \right\rangle$,
- fourth-power of total magnetization $\langle m^4 \rangle = \left\langle \left(\frac{1}{NM} \sum_{i=1}^{N} \sum_{t=1}^{M} \sigma_i(t) \right)^4 \right\rangle$,
- squared local magnetization $\langle m_i^2 \rangle = \left\langle \left(\frac{1}{M} \sum_{t=1}^{M} \sigma_i(t) \right)^2 \right\rangle$,
- fourth-power of total magnetization $\langle m_i^4 \rangle = \left\langle \left(\frac{1}{M} \sum_{t=1}^{M} \sigma_i(t) \right)^4 \right\rangle$,

where $\langle ... \rangle$ denotes thermal average and m shows the sum of spins over all sites and Trotter direction,

$$m = \frac{1}{NM} \sum_{i=1}^{N} \sum_{t=1}^{M} \sigma_i(t). \tag{4.3}$$

The quantity m_i shows the spin of local site averaged over Trotter direction,

$$m_i = \frac{1}{M}\sum_{t=1}^{M}\sigma_i(t). \tag{4.4}$$

We employ a GPU-based algorithm to perform Monte Carlo calculation and calculate the thermal averages of physical quantities. Details of the Monte Carlo algorithm we use in this study are summarized in Appendix B.

Following the prescription on Appendix C, we apply the finite-size scaling analysis to compute the critical point and critical exponents of the Binder ratio g:

$$g = \left[\frac{1}{2}\left(3 - \frac{\langle m\rangle^4}{\langle m^2\rangle^2}\right)\right], \tag{4.5}$$

The global susceptibility χ:

$$\chi = \left[\beta N \langle m^2\rangle\right], \tag{4.6}$$

The magnetization $[\langle|m|\rangle]$, and dynamical critical exponent. [3)]

As for the exponent d/z', we make the histograms $P(\chi_{\rm loc})$ of both local susceptibilities $\chi_{\rm loc}$ and nonlinear local susceptibilities $\chi_{\rm nlloc}$: [4)]

$$\chi_{\rm loc} = \langle m_i^2\rangle, \tag{4.7}$$

$$\chi_{\rm nlloc} = -(\langle m_i^4\rangle - 3\langle m_i^2\rangle^2), \tag{4.8}$$

which is expected to satisfy the relation elucidated in Chapter 3. Each histogram is made from $N \times N_{\rm rand}$ samples.

We also plot the same histogram for global (linear and nonlinear) susceptibilities: [5)]

$$\chi = \langle m^2\rangle, \tag{4.9}$$

$$\chi_{\rm nl} = -(\langle m^4\rangle - 3\langle m^2\rangle^2), \tag{4.10}$$

to compare the behavior to local susceptibilities. Each histogram is made from $N_{\rm rand}$ samples.

4.2. Results

4.2.1. Phase transitions and critical exponents

The left panel of Fig. 4.2 shows the Binder ratio as a function of Γ (strength of the transverse field) with the inverse temperature $\beta = 20$. We employ an alternative quantity $-\log(1-g)$ instead of a naive Binder ratio in order to obtain a good resolution near the critical point [56]. The figure indicates that the phase transition point is located around $\Gamma \sim 1.7$.

The right panel of Fig. 4.2 shows the result of finite-size scaling analysis of the left panel data. One can see that the data with different sizes collapse onto the same curve as we choose proper Γ_c and ν. From the finite-size scaling, the critical point and the critical exponent of the correlation length can be determined as $\Gamma_c = 1.75(4)$ and $\nu = 1.4(2)$ respectively. [6)]

[3)] $[\cdots]$ denotes the average over random instances.
[4)] We omit the coefficients from the susceptibilities since it does not affect the log-log plot.
[5)] We omit the coefficients for the same reason as local susceptibilities.
[6)] The right panel of Fig. 4.2

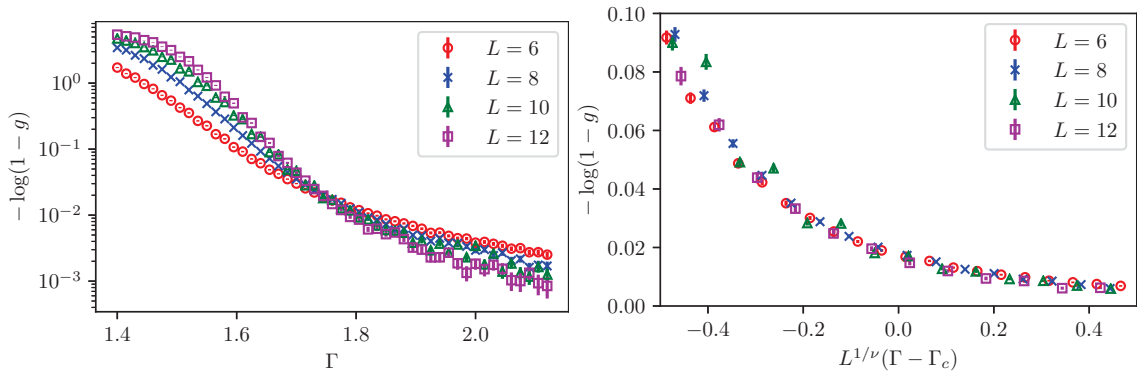

Figure 4.2.: (Left panel) TheBinder ratio $-\log(1-g)$ with different system sizes $L = 6, 8, 10, 12$ with the inverse temperature $\beta = 20$. Each curve crosses at the same point $\Gamma \sim 1.7$. (Right panel) finite-size scaling analysis of the Binder ratio with $\Gamma_c = 1.75(4)$ and $\nu = 1.4(2)$.

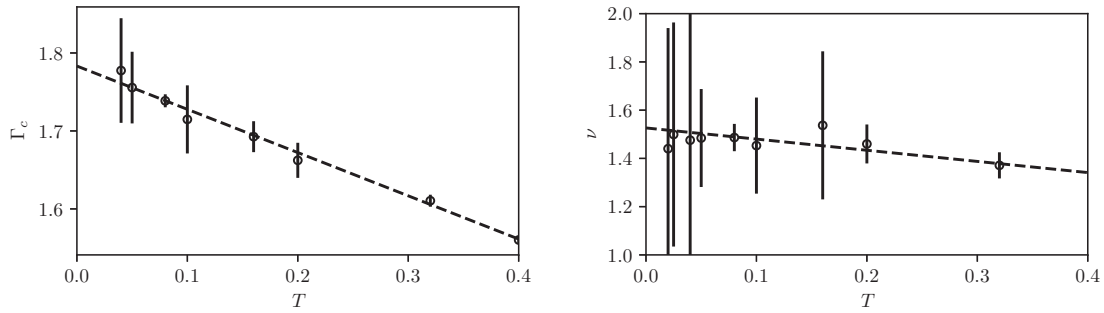

Figure 4.3.: Critical point Γ_c and critical exponent of the correlation length ν and as a function of temperature T. Black dashed line represents the linear fitting of the data. An extrapolation shows that $\Gamma_c = 1.783(3)$ and $\nu = 1.526(13)$ in the zero temperature limit.

We apply the same finite-size scaling for each temperature and the results are summarized in Fig. 4.3. From the left panel of the figure, we observe that Γ_c grows linearly as temperature T closes to zero. [7)] Linear fitting shows that Γ_c can be determined to 1.780(3) in the limit of zero temperature. We also see that the critical exponent ν does not clearly depend on the temperature and can be estimated as $\nu = 1.526(13)$. [8)]

The same analysis is performed on the global susceptibility χ and the magnetization $|m|$ as described in Figs. 4.4 and 4.5 and the results of extrapolation are in Fig.4.6.

To determine the dynamical critical exponent, we follow the finite-size scaling method elucidated in the Section C.3. It follows from this section that the right choice of the dynamical critical exponent makes the Binder ratios g with different sizes and temperatures collapse onto the same curve of

$$g \sim \tilde{f}(\beta/L^z), \tag{4.11}$$

[7)] The cases of $\beta = 40, 50$ are not included in the figure since the Trotterization error grows $\mathcal{O}((\beta/M)^2)$ and cannot be ignored especially in the region of lower temperatures (larger inverse temperatures).

[8)] One may notice that the error bar of the critical exponent ν seems to be relatively large especially near zero temperature. This large deviation comes from the fact that the data collapse in the right panel of Fig. 4.2 does not severely depend on the value ν: the data collapse behaves robustly against the deviation of the value ν. We performed the same finite size scaling analysis on different quantities (say magnetization and susceptibility) to obtain the value ν with a small error bar and confirmed that the result is consistent to that obtained from the Binder ratio.

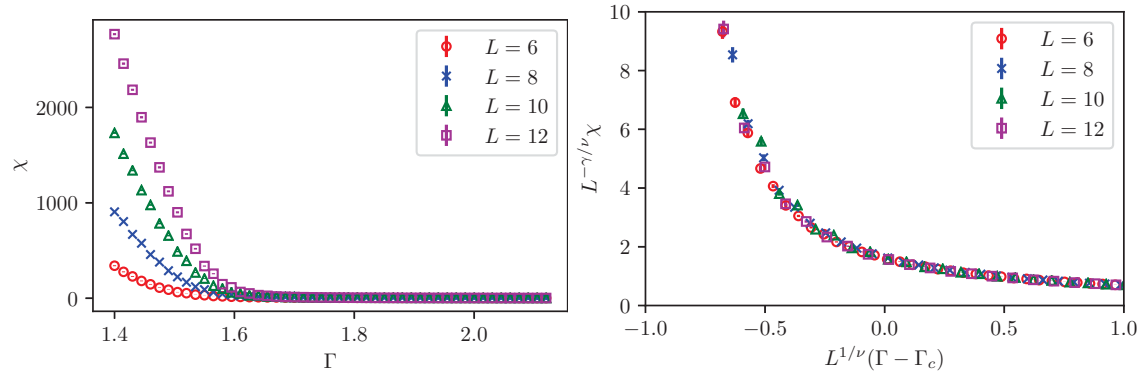

Figure 4.4.: (Left panel) global susceptibility χ with different system sizes $L = 6, 8, 10, 12$ with the inverse temperature $\beta = 20$. (Right panel) finite-size scaling analysis of the global susceptibility with $\gamma = 0.96(6)$.

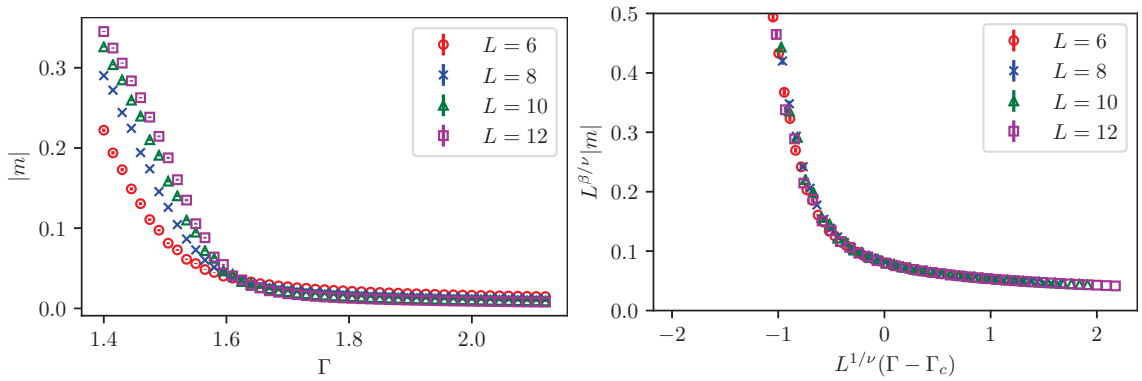

Figure 4.5.: (Left panel) magnetization $|m|$ with different system sizes $L = 6, 8, 10, 12$ with the inverse temperature $\beta = 20$. (Right panel) finite-size scaling analysis of the global susceptibility with $\beta = 0.95(6)$.

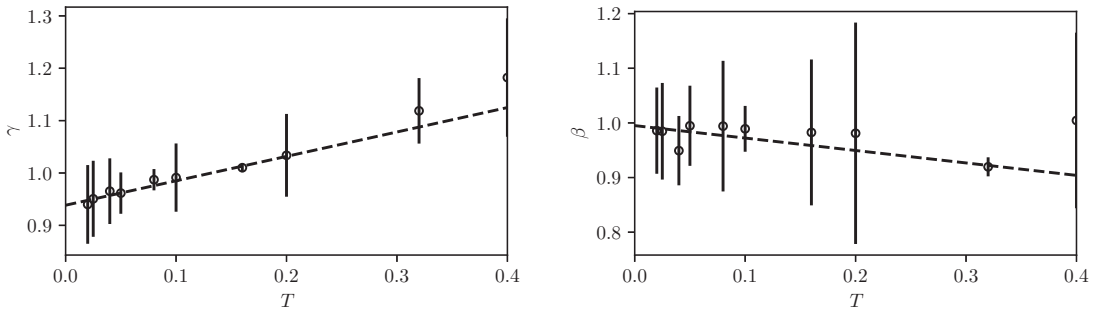

Figure 4.6.: Critical exponents of the global susceptibility γ and the magnetization $|m|$ as a function of temperature T. Black dashed line represents the linear fitting of the data. An extrapolation shows that $\gamma = 0.938(8)$ and $\beta = 0.995(12)$ in the zero temperature limit.

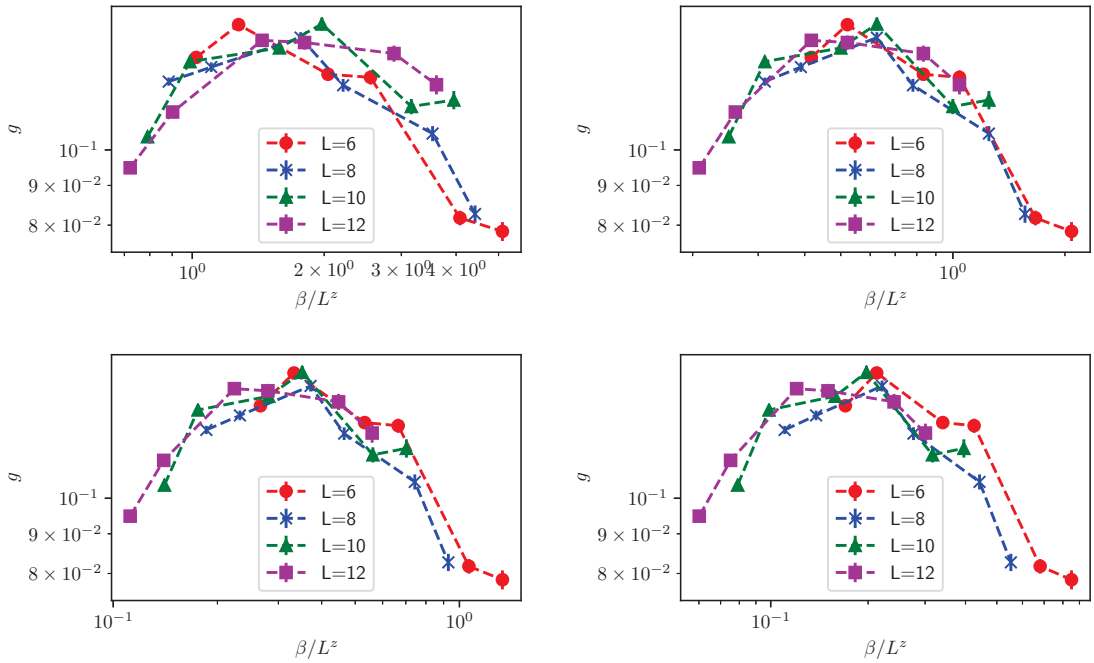

Figure 4.7.: Binder ratio g with different sizes as a function of β/L^z at the critical point. The dynamical critical exponent z is set to $z = 0.5$ (left top), $z = 1.0$ (right top), $z = 1.25$ (left bottom), and $z = 1.5$ (right bottom). The plots use logarithmic scales on both horizontal and vertical axes.

at the critical point and the plot is on Fig. 4.7.

Since it is difficult to determine z precisely from these figures, we employ the following "mean squared error" criteria. One can see that the function $\tilde{f}(\beta/L^z)$ can be parametrized by a quadratic function as [9)]

$$\log g = \log\left(a\left(\frac{\beta}{L^z}\right)^2 + b\left(\frac{\beta}{L^z}\right) + c\right), \tag{4.12}$$

where $a < 0$ since all data in Fig. 4.7 roughly collapse onto a single concave function. By fitting parameters a, b, c to minimize the mean squared error between the parametrized function and the actual Binder ratio, we get the optimal parameters a, b, c and the corresponding mean squared error. This mean squared error indicates how precise the data collapse onto the single curve, which is depicted in Fig. 4.8. This graph clearly shows that the mean squared error takes the minimal value around $z = 1$, which means that setting z to 1 gives the best data collapse. For this reason we can determine the dynamical critical exponent is around $z \simeq 1$. The derived critical point and critical exponents are listed on Table. 4.2.

4.2.2. Histograms of susceptibilities

In this section we derive the exponent d/z' from the result of local (and global) susceptibilities.

[9)] Remember that Fig. 4.7 uses log-log plot.

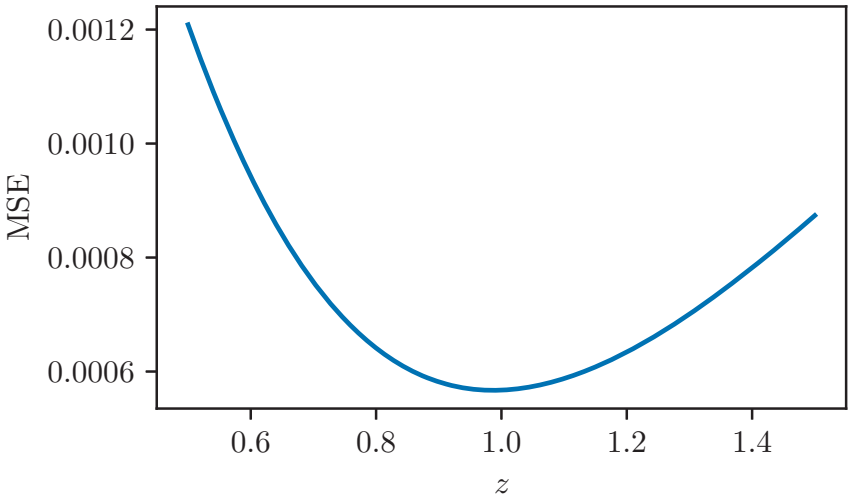

Figure 4.8.: Mean squared error (MSE) as a function of dynamical exponent z. This figure shows that MSE takes minimal value around $z \simeq 1$.

Table 4.2.: Critical point and critical exponents of the sparse chimera graph in the zero temperature limit. η is determined by the relation $\nu(2-\eta) = \gamma$.

		value
critical point	Γ_c	1.780(3)
magnetization	β	0.995(12)
susceptibility	γ	0.938(8)
correlation length	ν	1.526(13)
correlation function	η	1.385(7)
dynamical critical exponent	z	$\simeq 1$

Local susceptibilities

Fig. 4.9 shows the histogram of the local susceptibilities $P(\chi_{\mathrm{loc}})$ in a paramagnetic region far from the critical point ($\Gamma = 1.895$).

In this region one can see the behavior of the histogram is independent of system size and roughly obeys the power-law. Following the relation of Eq. (3.25) which can be rewritten as

$$\log P(\chi_{\mathrm{loc}}) \sim -\left(\frac{d}{z'} + 1\right) \log \chi_{\mathrm{loc}}, \tag{4.13}$$

Since the above relation is expected to hold in a large susceptibility region (the clusters which have a small energy gap), we apply a linear fitting mainly to a large region of susceptibilities. One can read the value d/z' by observing the slope of the black solid line in Fig. 4.9. In this situation d/z' turns out to be around 11.15. Following the discussion in Chapter 3, we can conclude that both linear and nonlinear susceptibilities exhibit no divergence at the point since $d/z' > 3$.

Figure 4.10 shows the same histogram where Γ is set to be close to the critical point Γ_c. We observe that the slope clearly depends on the system size owing to the finite-size effect and the slope tends to be shallow as system size increases. To extract the information of d/z', we apply the linear fitting to the system with largest size $L = 12$ whose slope is expected to be near the system with infinite system size. The actual value of d/z' should

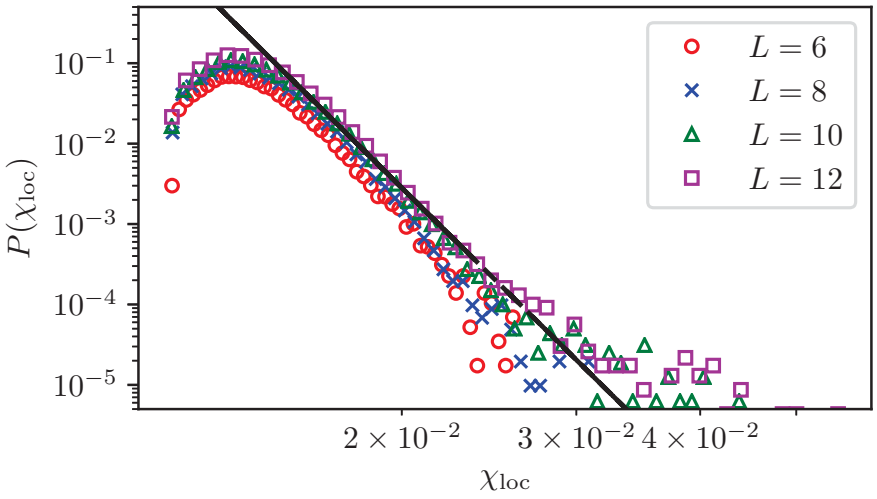

Figure 4.9.: Log-log plot of the histogram of the local susceptibility $P(\chi_{\mathrm{loc}})$ for different sizes and inverse temperature $\beta = 50$ and the transverse field $\Gamma = 1.895$. Black solid line shows the fitting to the data whose slope is -12.15, which indicates that $d/z' = 11.15$.

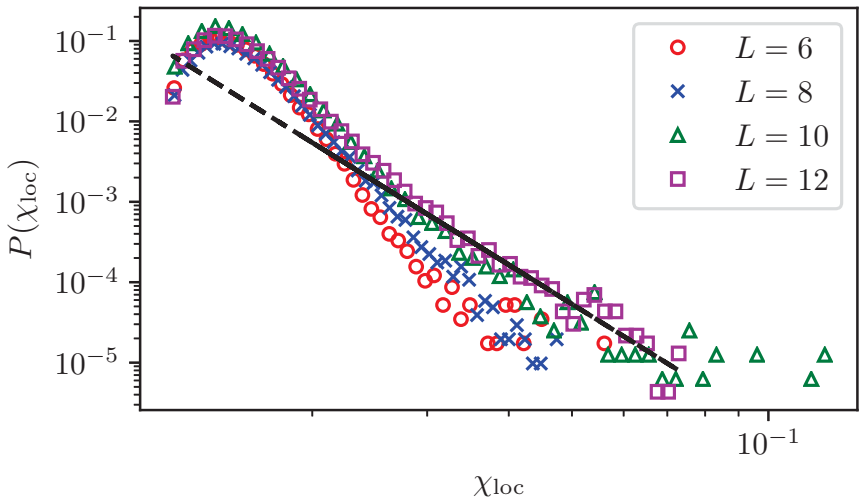

Figure 4.10.: Log-log plot of the histogram of the local susceptibility $P(\chi_{\mathrm{loc}})$ for different sizes and inverse temperature $\beta = 50$ and the transverse field $\Gamma = 1.79$. The slope clearly depends on the system size compared to Fig. 4.9. Black solid line shows the fitting to the data with the largest system size $L = 12$ whose slope is -5.04, which indicates that d/z' is at least smaller than 4.04.

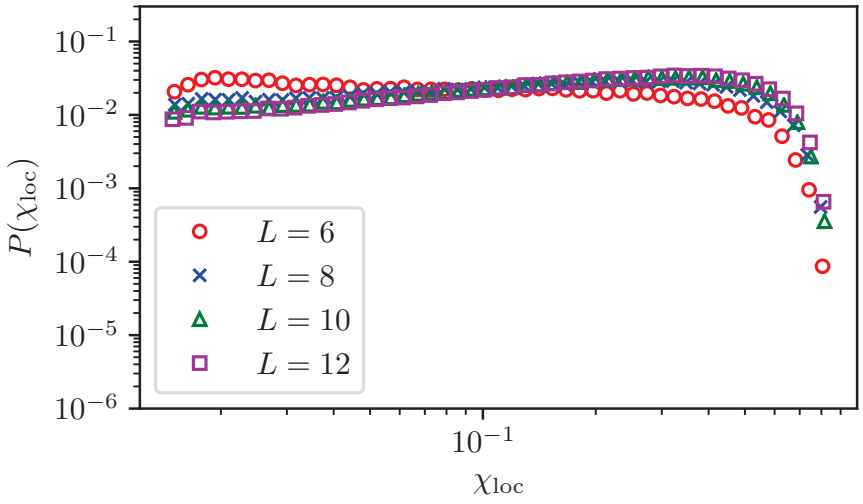

Figure 4.11.: Log-log plot of the histogram of the local susceptibility $P(\chi_{\mathrm{loc}})$ for different sizes and inverse temperature $\beta = 50$ and the transverse field $\Gamma = 1.4$ (ferromagnetic phase). We find that $P(\chi_{\mathrm{loc}})$ grows monotonically as the susceptibility χ_{loc} increases especially for the largest system size $L = 12$.

thus be smaller than the slope. From this figure we can say that the exponent d/z' is is at least smaller than 4.04.

The histogram $P(\chi_{\mathrm{loc}})$ in the ferromagnetic phase $\Gamma_c = 1.4$ is on Fig. 4.11. We find the behavior of the histogram of the susceptibility is quite different compared to the above results. In the ferromagnetic phase, $P(\chi_{\mathrm{loc}})$ increases monotonically as the susceptibility χ_{loc} increases especially for large system size.

We perform the same method to nonlinear local susceptibility χ_{nlloc}. The results for $\Gamma = 1.895$ (far from the critical point) and $\Gamma = 1.79$ (near the critical point) are shown in Figs. 4.12 and 4.13 respectively. The histograms exhibit similar behavior to that of linear local susceptibility where the plots has no size-dependence in the case the transverse field Γ is far from the critical point Γ_c and has clear size-dependence in the case Γ is near Γ_c. The slope is expected to obey the assumption in Eq. (3.31),

$$\log P(\chi_{\mathrm{nlloc}}) \sim -\left(\frac{d}{3z'} + 1\right) \log \chi_{\mathrm{nlloc}}. \tag{4.14}$$

We measure the slope (i.e., d/z') for each transverse field and the exponent z' as a function of the transverse field Γ is shown on Fig. 4.14. [10] [11]

We observe that the exponent z' starts to grow near the critical point and exceed the value $d/z' = 3$ where the nonlinear susceptibility starts to diverge, whose behavior is consistent to the previous study [21]. The bottom figure in Fig. 4.14 shows that the d/z' decrease linearly towards the critical point, which means that the behavior of the exponent

[10] Even though the space dimension d of the percolated sparse chimera graph is still unclear, we can determine the value via the other exponents. Using a relation derived from Eqs. (C.3) to (C.4),

$$\frac{\beta}{\nu} = \frac{d + z - 2 + \eta}{2}, \tag{4.15}$$

and the exponents on Table. 4.2, d should be near 1, which implies that the percolated sparse chimera graph is close to one-dimensional system.

[11] As explained above, the actual value of z' might be larger than the data indicated in Fig. 4.14 especially in the vicinity of the critical point.

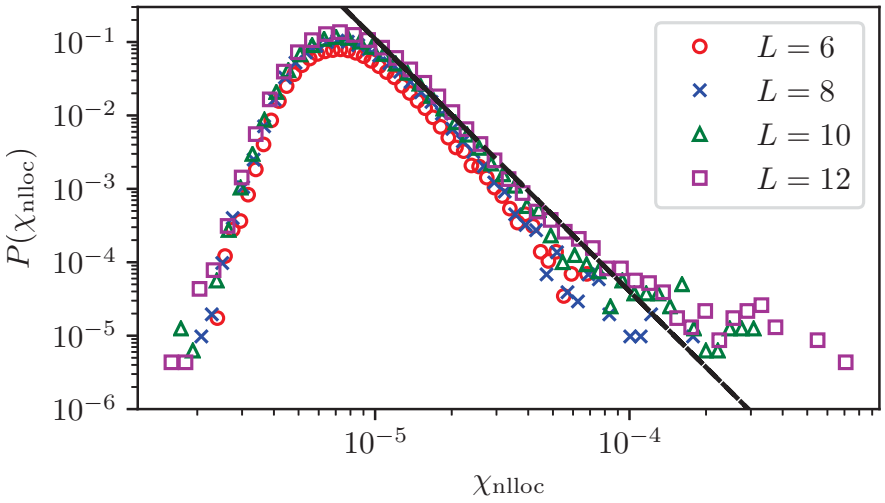

Figure 4.12.: Log-log plot of the histogram of the nonlinear local susceptibility $P(\chi_{\mathrm{nlloc}})$ for different sizes and inverse temperature $\beta = 50$ and the transverse field $\Gamma = 1.895$. Black solid line shows the fitting to the data whose slope is -3.436, which indicates that $d/3z'$ is around 2.436.

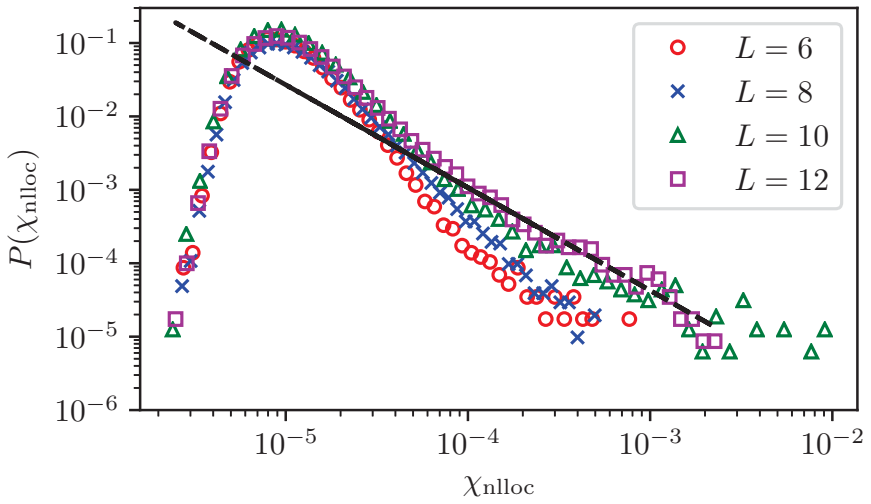

Figure 4.13.: Log-log plot of the histogram of the nonlinear local susceptibility $P(\chi_{\mathrm{nlloc}})$ for different sizes and inverse temperature $\beta = 50$ and the transverse field $\Gamma = 1.79$. Black solid line shows the fitting to the data with the largest system size $L = 12$ whose slope is -1.4, which indicates that $d/3z'$ is at least smaller than 0.4.

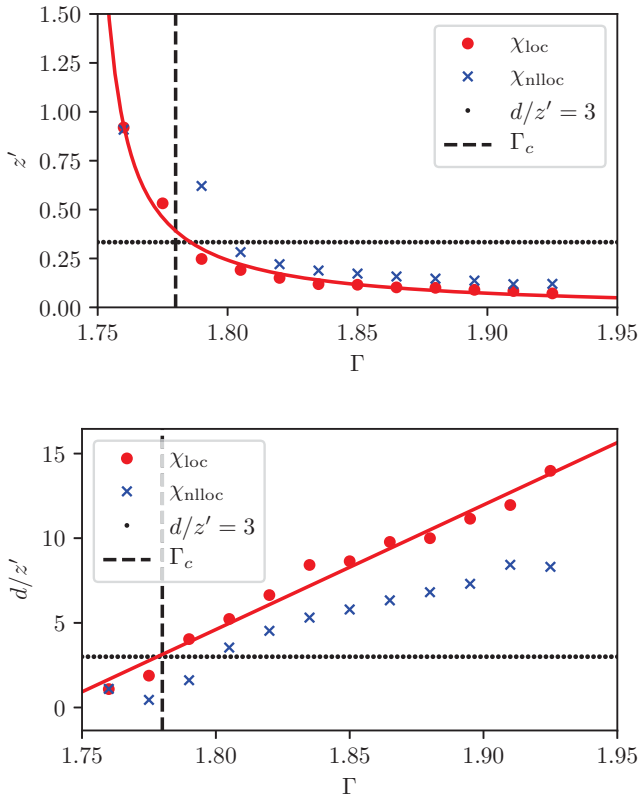

Figure 4.14.: (Top) The exponent z' as a function of Γ. The data with circle and cross marker are taken from χ_{loc} and χ_{nlloc} respectively. Vertical dashed line shows the critical point in the zero temperature limit $\Gamma_c = 1.78$ and the actual critical point should be smaller than Γ_c since the results are taken with a finite temperature. Horizontal dotted line illustrates the point $d/z' = 3$ where the nonlinear susceptibility starts to diverge. Red solid curve is just a guide for eye. (Bottom) The same data but the vertical axis shows d/z' and the red solid line shows the linear fitting to χ_{loc}.

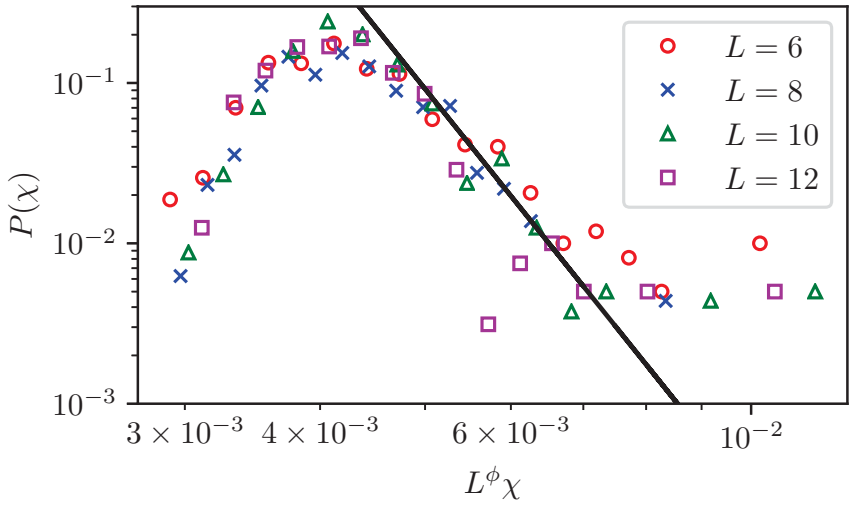

Figure 4.15.: $P(\chi)$ which is similar to Fig. 4.9 but for the global susceptibility and $\Gamma = 1.925$ (far from the critical point). Black solid line shows the fitting to the data whose slope is -8.418, which indicates that d/z' is around 7.418.

z' near the critical point can be approximated by inverse of linear function, which is in some sense consistent to the result of Fisher [55]. Taking the fact that the actual z' might be larger than the plot in Fig. 4.14 into consideration, we can say that there does exist the point where the nonlinear susceptibility starts to diverge in the paramagnetic region induced by the Griffiths-McCoy singularity. Besides, we also find that the linear susceptibility seems not to diverge since none of these data in the paramagnetic phase satisfies the condition $d/z' < 1$ where the linear susceptibility starts to diverge.

Global susceptibilities

Figure 4.15, 4.16, and 4.17 shows the histogram $P(\chi)$ as a function of global linear (or nonlinear) susceptibility. [12] Although the histogram is deviated compared to those of local susceptibilities due to lack of samples, these figures shows qualitatively the same behavior as the histogram of local susceptibilities. As for global linear susceptibility, Fig. 4.15 shows that the slope is independent of system size when the system is far from the critical point and Fig. 4.16 also shows that this slope turns to depend on system size near the critical point.

We extract d/z' from the global linear susceptibility in the same way as the local linear susceptibility and the result is illustrated on Fig. 4.18. [13]

From these results we conclude that global linear susceptibility exhibits quite a similar behavior to that of local linear susceptibility in terms of both histograms and the exponent z'. In the same as the local susceptibilities, we read from the bottom panel of Fig. 4.18 that the d/z' decreases linearly.

[12] The horizontal axis of global susceptibilities is scaled as $L^{\phi}\chi$ so as to make plots with different sizes gather onto the same region, which does not change the slope since this scaling only moves plots along the horizontal axis.

[13] One may find a large tail especially in the region of large susceptibility in the histogram of susceptibility (such as Figs. 4.15 and 4.16). Taking the number of samples ($N_{\mathrm{rand}} = 200$) into consideration, the plot with $P(\chi) \sim N_{\mathrm{rand}} \sim 1/\sim 10^{-2}$ can be ignored since the number of counts is too small to rely on.

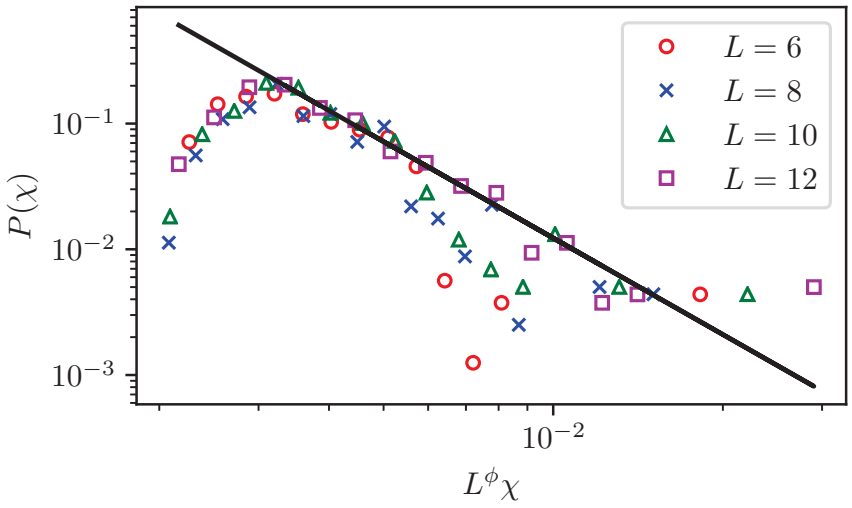

Figure 4.16.: $P(\chi)$ which is similar to Fig. 4.9 but for the global susceptibility and $\Gamma = 1.79$ (close to the critical point). Black solid line shows the fitting to the data whose slope is -2.65, which indicates that d/z' is around 1.65.

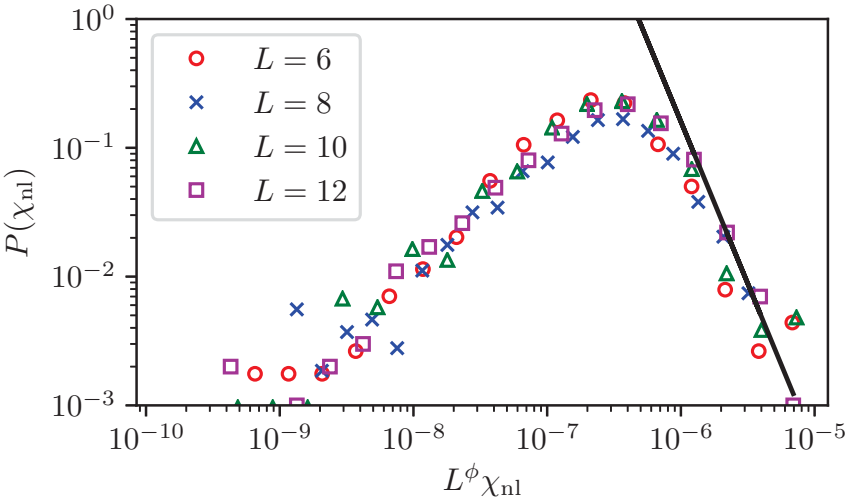

Figure 4.17.: $P(\chi_{\mathrm{nl}})$ which is similar to Fig. 4.12 but for the global nonlinear susceptibility and $\Gamma = 1.91$. Black solid line shows the fitting to the data whose slope is -2.514, which indicates that $d/3z'$ is around 1.514.

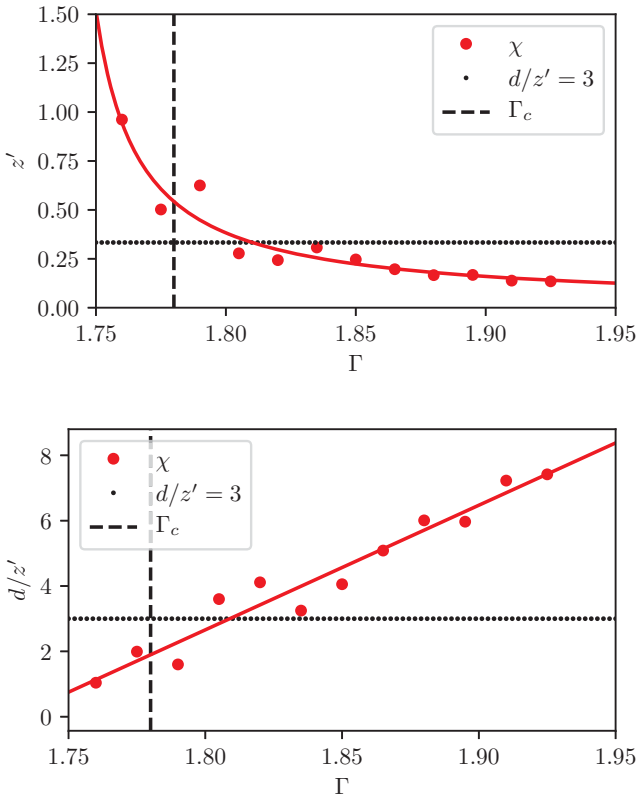

Figure 4.18.: (Top) similar to Fig. 4.14 but for the global linear susceptibility. Red solid curve is just a guide for eye. (Bottom) the same as the top panel but the vertical axis shows d/z'.

4.3. Summary and discussion

In this chapter we investigated the percolated sparse chimera graph model with a transverse magnetic field by using the quantum Monte Carlo method to explore phenomena induced by the Griffiths-McCoy singularity.

We first explored the property of phase transitions and critical exponents for each temperature using finite size scaling analysis and the results in the zero temperature limit are summarized in Table. 4.2. We also find from the calculation that the dynamical critical exponent z should be unity, which is reasonable since the model has almost the same ferromagnetic connectivity along the spatial and the Trotter direction. A similar model is dealt with the previous study and in the study authors also concluded that z should be unity [26]. Although the space dimension of the percolated sparse chimera model is not trivial, this dimension d can be derived by using scaling relation from Eqs. (C.3) to (C.4) and the calculated critical exponents, leading to $d \simeq 1$. This means that the percolated sparse chimera model we deal with is close to a one-dimensional system.

Note that the critical points and critical exponents with transverse Ising model with different (but similar) interactions are investigated in previous studies. One of the similar models are square lattice Ising model with random interactions and transverse field studied by Rieger and Kawashima [57] whose Hamiltonian is

$$H = \sum_{\langle i,j \rangle} J_{ij} \hat{\sigma}_i^z \hat{\sigma}_j^z - \Gamma_i \sum_i \hat{\sigma}_i^x, \tag{4.16}$$

where the distributions of J_{ij} and Γ_i are

$$P(J_{ij}) = \begin{cases} 1 & \text{for } 0 < J_{ij} < 1 \\ 0 & \text{otherwise} \end{cases}, \tag{4.17}$$

$$P(\Gamma_i) = \begin{cases} \Gamma^{-1} & \text{for } 0 < \Gamma_i < \Gamma \\ 0 & \text{otherwise} \end{cases}. \tag{4.18}$$

Previous studies mainly focus on models with typical connectivity, e.g., square or cube lattice Ising model, (see [23,26,58]), whereas our model focuses on the chimera graph which is implemented on the D-Wave quantum annealer. Although classical random Ising model with chimera connectivity is studied in [59], there critical points and critical exponents of sparse chimera graph with transverse quantum term has not been investigated. It can be said that our Monte Carlo study is the first study of investigating critical exponents of transverse Ising model with sparse chimera graph.

We next focused on the histogram of the local susceptibilities to extract the exponent d/z' which is directly connected with the Griffiths-McCoy singularity as explained in Chapter 3. Figures of the histogram of the local susceptibilities show that the histogram is independent of system size for the transverse field far from the critical point, whereas in the vicinity of the critical point, the finite size effect may affect the system, which leads to the system size dependence of the histogram. The exponent z' as a function of the transverse field Γ is summarized on Fig. 4.14. As stated above, we can conclude that there does exist the region in a paramagnetic phase that the nonlinear susceptibility diverges whereas the linear susceptibility does not.

We also apply the same analysis not only to local susceptibilities but also to global susceptibilities. In the case of the global linear susceptibility, we obtain the similar behavior of the histograms and the exponent z' to local susceptibilities as illustrated in Figs. 4.15, 4.16, and 4.18.

As for the global nonlinear susceptibility, however, the exponent z' is quite different compared to Fig. 4.18. The histogram of the global nonlinear susceptibility which is

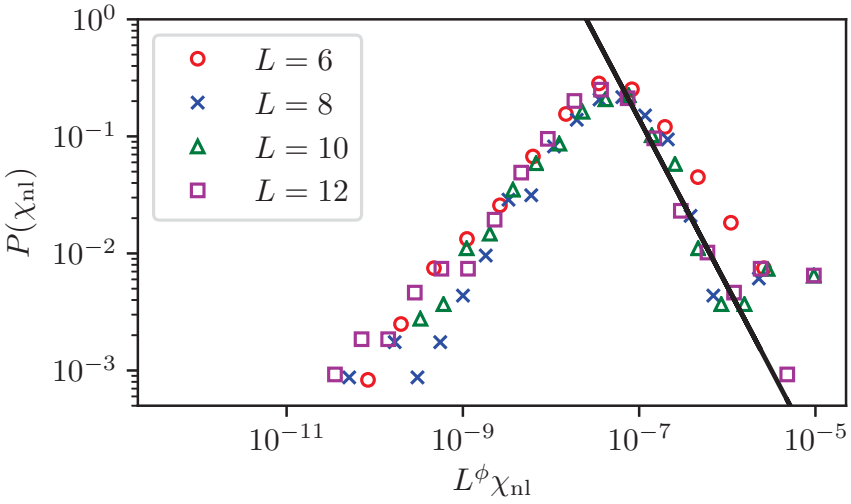

Figure 4.19.: $P(\chi_{\mathrm{nl}})$ which is similar to Fig. 4.12 but for the global nonlinear susceptibility and $\Gamma = 1.865$. Black solid line shows the fitting to the data whose slope is -1.428, which indicates that $d/3z'$ is around 0.428 or $z' \sim 1.2$, which seems to be quite large compared to the data from global linear susceptibility in Fig. 4.18.

far from the critical point is shown on Fig. 4.19. One can read from the figure that the exponent d/z' is relatively small compared to the data from the global linear susceptibility. One of the possible reasons for this unexpected behavior lies in the fact that the nonlinear susceptibility diverges at the critical point strongly enough that the power-law Eq. (3.31) cannot be applied. In fact, the global nonlinear susceptibility diverges at the criticality as [23]

$$\chi_{\mathrm{nl}} \sim L^{2-\eta+2z}, \tag{4.19}$$

which is stronger than the global linear susceptibility which diverges as

$$\chi \sim L^{2-\eta}. \tag{4.20}$$

5. Experiments on the D-Wave quantum annealer

In the previous chapter we performed quantum Monte Carlo simulations to investigate the phenomena induced by Griffiths-McCoy singularities on the percolated sparse chimera model. We next run the above experiment on the D-Wave machine by using it as a quantum simulator to demonstrate the Griffiths-McCoy singularities. In this chapter, we show the detailed method and the results following the technical details of the use of the D-Wave machine explained in Section 2.4.

5.1. Models and methods

The Hamiltonians of the model in the D-Wave machine is represented by using annealing schedule s and the functions $A(s)$ and $B(s)$ (see Fig. 2.3 for details) as follows:

$$H(s) = -\frac{A(s)}{2}\left(\sum_i \hat{\sigma}_i^x\right) + \frac{B(s)}{2}\left(\sum_{\langle i,j\rangle} J_{ij}\hat{\sigma}_i^z\hat{\sigma}_j^z\right), \tag{5.1}$$

where $A(s)$ and $B(s)$ are monotonically decreasing and increasing functions respectively. This means that if we apply the anneal-pause-quench protocol with the pause point s_*, the D-Wave machine is expected to give spin configuration $\boldsymbol{\sigma}$ sampled from the canonical ensemble with the Hamiltonian $H(s_*)$ (5.1).

As introduced in Chapter 4, we use the sparse chimera graph for the simulation on the D-Wave machine. We set the amplitude of the interactions to a half of that used in the quantum Monte Carlo method,

$$P(J_{ij}) = \frac{1}{6}\sum_{k=0}^{5}\delta(J_{ij} + 0.1k), \tag{5.2}$$

which is expected to reduce the effect of the noise in the D-Wave machine. The parameters used throughout the experiments are listed on Table. 5.1. [1)] With these parameters, we measured magnetizations and global susceptibilities by using the D-Wave device, which is described in the following sections.

Measuring magnetizations

First we describe how to measure the magnetization. For each annealing process, we obtain a set of spins $\{\sigma_1, \sigma_2, \cdots\}$ from the D-Wave machine following the anneal-pause-quench protocol (see Section 2.4.2) with longitudinal field switched off ($\Phi(t_f) = 0$) and store the magnetization,

$$m_a = \frac{1}{N}\sum_{i=1}^{N}\sigma_i. \tag{5.3}$$

[1)] # of random instances is set to 438 for histogram of susceptibility to obtain more reliable data.

Table 5.1.: Parameters for calculations on the D-Wave machine. Some of the notations listed on the table are defined in figures in Sections 2.4.2 and 2.4.3. The last four parameters are for measuring susceptibilities (see Section 2.4.3 for details).

# of random instances N_{rand}	255
# of repetition times of annealing N_{rep}	100
system size N	$L \times L \times 8$ $(L = 8, 12, 16)$
minimum value of annealing schedule $s_{*\mathrm{min}}$	0.36
maximum value of annealing schedule $s_{*\mathrm{max}}$	0.41
# of transverse fields N_Γ	50
anneal time in anneal-pause-quench t_1	1000 s_* μs
pause time in anneal-pause-quench $t_2 - t_1$	100μs
quench time in anneal-pause-quench $t_f - t_2$	$(1 - s_*)$ μs
readout_thermalization	2000 μs
range of the amplitude at $t = t_f$ $\Phi(t_f)$	$[-2, 2]$
local fields h_i	0.02
timing t_1' in the schedule $\Phi(t)$	$\frac{3t_1+t_2}{4}$ μs
timing t_2' in the schedule $\Phi(t)$	$\frac{t_1+t_2}{4}$ μs

This annealing process is repeated N_{rep} times to obtain the set of magnetization m_a $(1 \leq a \leq N_{\mathrm{rep}})$. Given enough interval time between each annealing process (the parameter "readout_thermalization" in Table. 5.1, [2)] we can assume that magnetizations m_a are uncorrelated each other. The nth power of the magnetization is calculated from these as

$$\langle m^n \rangle = \frac{1}{N_{\mathrm{rep}}} \sum_{a=1}^{N_{\mathrm{rep}}} m_a^n, \tag{5.4}$$

Various physical quantities such as the Binder ratio are derived from the above nth power of the magnetization.

Measuring susceptibilities

As for measuring linear (and nonlinear) susceptibilities χ and χ_{nl}, we modulate the amplitude of the local field bias $\Phi(t)$ and obtain magnetizations in the same way as above for each amplitude. Linear and nonlinear susceptibility (χ and χ_{nl}) are obtained by applying a polynomial fit to magnetizations (see Section 2.4.3 for details),

$$m \sim \chi h - \chi_{\mathrm{nl}} h^3 + \cdots, \tag{5.5}$$

for each random instance.

Noise mitigation

Since the D-Wave machine is intrinsically an analog device, naive runs of the machine without any noise mitigation results in generating doubtful outputs due to systematic error on the machine. We apply two kinds of techniques, namely *calibrating individual flux bias* and *gauge averaging*, to reduce noise and obtain more reliable results. Technical description of these algorithms are summarized in Appendix D.

[2)] This parameter can be controlled via "readout_thermalization" in Table. 5.1.

5.2. Results

5.2.1. Histogram of magnetizations

Let us first see the distribution of the magnetization derived from the D-Wave machine. Figure 5.1 shows the histogram of the magnetization as a function of the annealing schedule s_* for each system size. This figure, especially for the system with larger size, clearly shows that the magnetizations are distributed around zero below the certain value of the annealing schedule s_* and tend to have a peak around ± 1 above the point. This drastic change of the shape of the histogram indicates the existence of a phase transition point around $s_{*c} \sim 0.39$. Besides, especially for small system size, one can see that some samples still have values which are close to ± 1 even in the region which is supposed to be the paramagnetic phase. One of the possible reasons of this unnatural behavior is a systematic error which comes from the quench process during the anneal-pause-quench protocol. At the end of the protocol, the annealing schedule s is changed from s_* to 1 quickly, which corresponds to "switching-off" of the transverse field. Although this quench is expected to be performed quickly so that the effect on the system is negligible, the elapsed time ($\sim 1\mu$s) is in some sense enough to affect the final state of the system, leading to a broad distribution of the magnetization in the paramagnetic region. A similar effect is observed in the previous research [60] where the histogram of the magnetization derived from the D-Wave machine exhibits a broad distribution in the paramagnetic phase, which is similar to our result.

A system with small size tends to be affected by this quench more significantly than that with a large system size. This is one of the qualitative differences between the data from the quantum Monte Carlo and from the D-Wave machine.

5.2.2. Phase transitions

Next we show the result of various physical quantities derived from the D-Wave machine.

Binder ratio and averaged magnetizations

The results of the Binder ratio g which is defined as

$$g = \frac{1}{2}\left[3 - \frac{\langle m^4 \rangle}{\langle m^2 \rangle^2}\right], \tag{5.6}$$

and the averaged magnetization defined as [3)]

$$m_{\mathrm{av}} = [\langle |m| \rangle], \tag{5.7}$$

are shown on Fig. 5.2. It is expected that the Binder ratio with different system sizes have a crossing point at the phase transition point as confirmed in the quantum Monte Carlo method in Fig. 4.2, however, one may notice that there is no crossing point in Fig. 5.2 and both the Binder ratio and the averaged magnetization have a finite value even in the paramagnetic region especially for small system size. This behavior can also be explained in the same way as the case of the histogram of magnetization: The quench process in the anneal-pause-quench protocol prevents the quantities from taking small values in the paramagnetic region. Nevertheless, we find that the magnetization shows tanh-like curve and start to rise near the point $s_* \sim 0.39$, implying the existence of a phase transition point near this value.

[3)] $[\cdots]$ denotes average over random instances

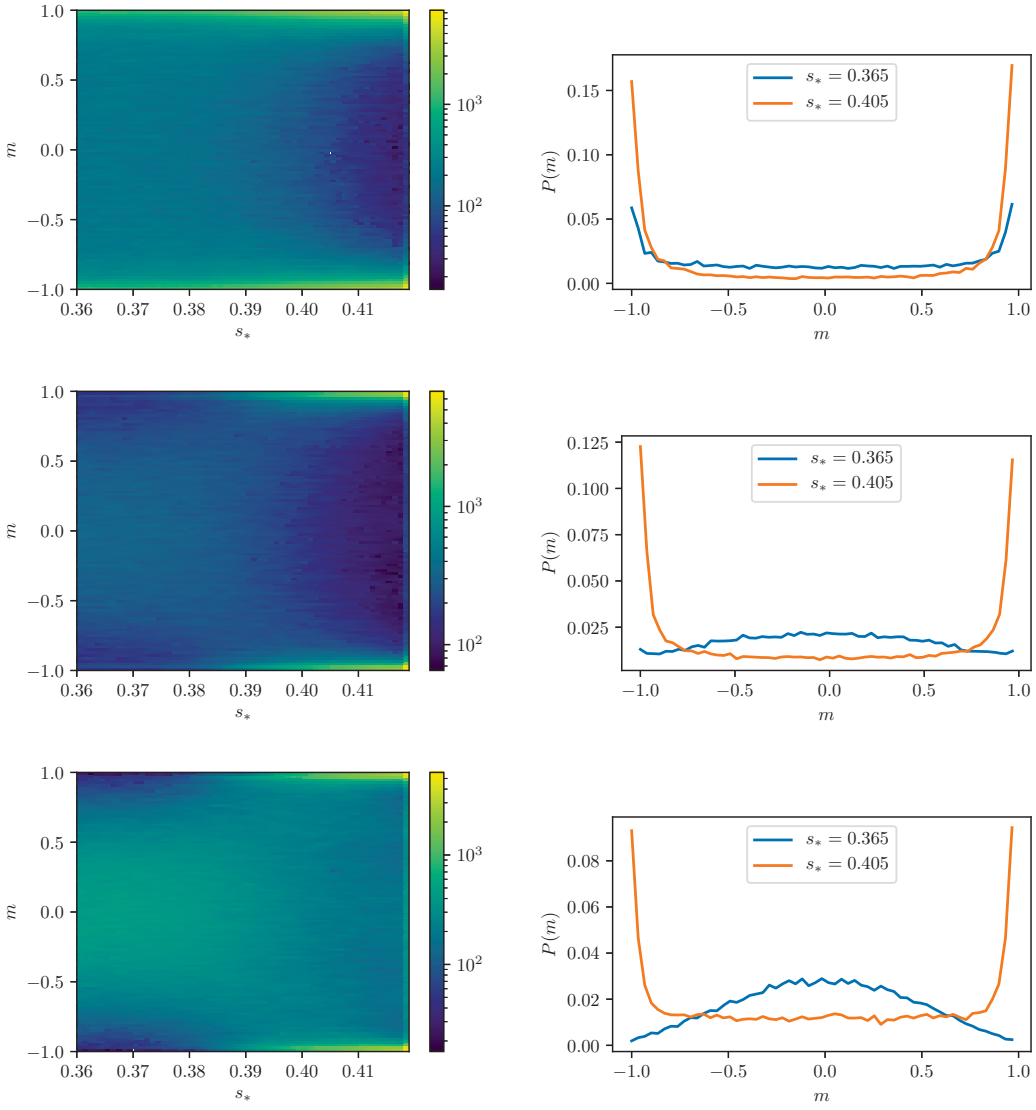

Figure 5.1.: (Left) Histograms (color map) of magnetization with system sizes $L = 8$ (top), $L = 12$ (middle), and $L = 16$ (bottom). s_* denotes the pause point during the anneal-pause-quench protocol. The horizontal axis shows the magnetization. Below a certain point $s_* \sim 0.39$ each magnetization tends to be distributed around zero, which implies that the system is in the paramagnetic region. In the region s_* is larger than 0.39, magnetizations tend to have values close to ± 1, implying the system is in the ferromagnetic phase. Note that the histogram is in logarithmic scale. (Right) Histograms of magnetization with system sizes $L = 8$ (top), $L = 12$ (middle), and $L = 16$ (bottom). The pause point s_* is fixed to 0.365 (paramagnetic phase) and 0.405 (ferromagnetic phase).

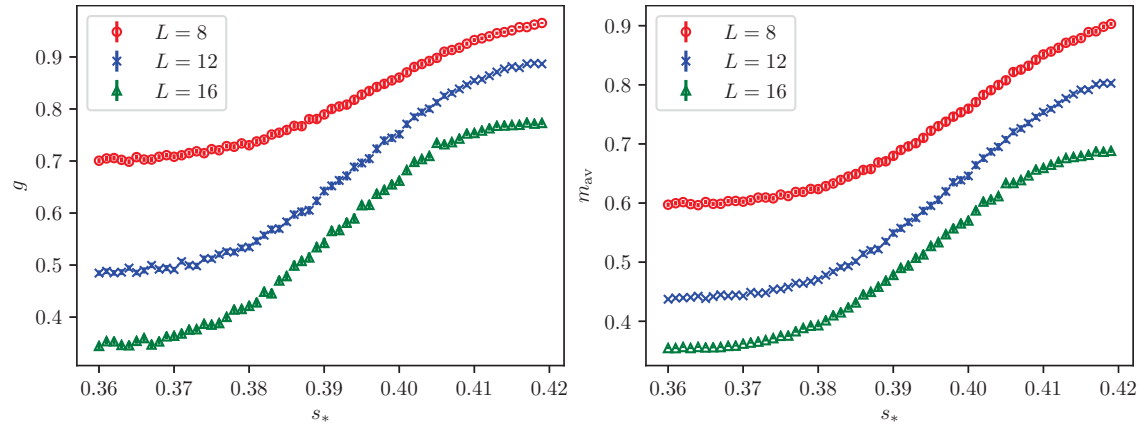

Figure 5.2.: (Left) The Binder ratio g for each system size obtained from the D-Wave machine. (Right) Averaged magnetization m_{av} for each system size obtained from the D-Wave machine.

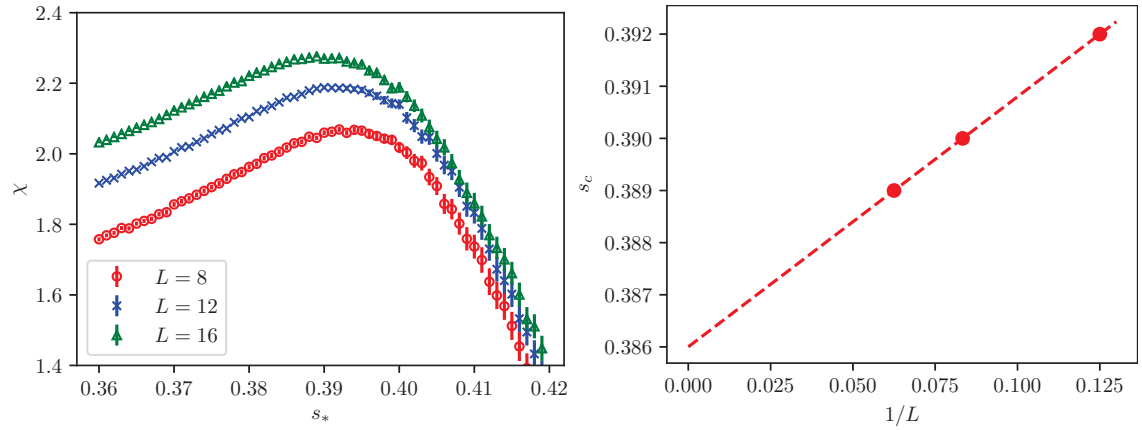

Figure 5.3.: (Left) Global linear susceptibility for each system size obtained from the D-Wave machine. (Right) peak point (which corresponds to the phase transition point s_c) as a function of inverse system size $1/L$. Red dashed line shows fitting to the plot. This figure shows that the phase transition point in the infinite system size limit ($1/L \to 0$) is around 0.386.

Global susceptibilities

The left panel of Fig. 5.3 shows the global linear susceptibility χ for each system size. We find that there is a clear peak of the susceptibility at the point $s_* \sim 0.39$ and the peak position becomes smaller as the system size increases, which indicates the existence of a phase transition at the peak point. To obtain the peak position in the infinite system size limit, we apply an extrapolation to the infinite system size, which is depicted in the right panel of Fig. 5.3. This extrapolation shows that the $s_c \sim 0.386$, which is consistent to data of the histogram of magnetizations in Fig. 5.1.

Besides, it seems that some of the behaviors of the susceptibility are inconsistent with physical intuitions. First, the sharpness of the peak is independent of the system size. Since the system with larger size tends to exhibit stronger singular behavior at the critical point, its peak should be sharper than that obtained from the D-Wave machine. Second, the exponent of the correlation length is unexpectedly large. We apply the finite scaling analysis to the global linear susceptibility with the critical point derived by the above extrapolation, $s_c = 0.386$ and the result is on Fig. 5.4. We find that the critical exponent of the correlation length is quite larger than the exponent derived from the quantum Monte

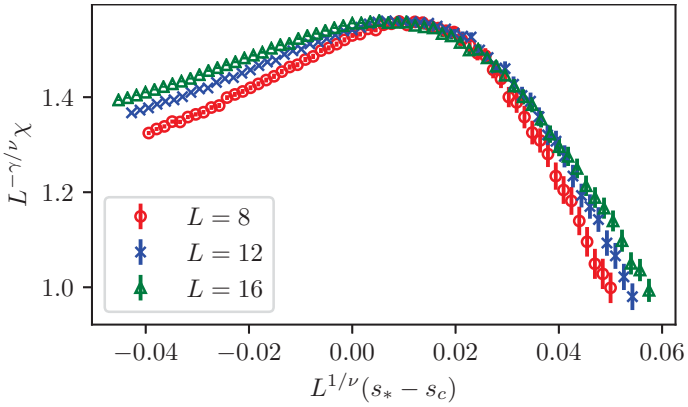

Figure 5.4.: Finite size scaling analysis on the global linear susceptibility with parameters $\nu = 5$, $s_c = 0.386$, and $\gamma/\nu = 0.136$.

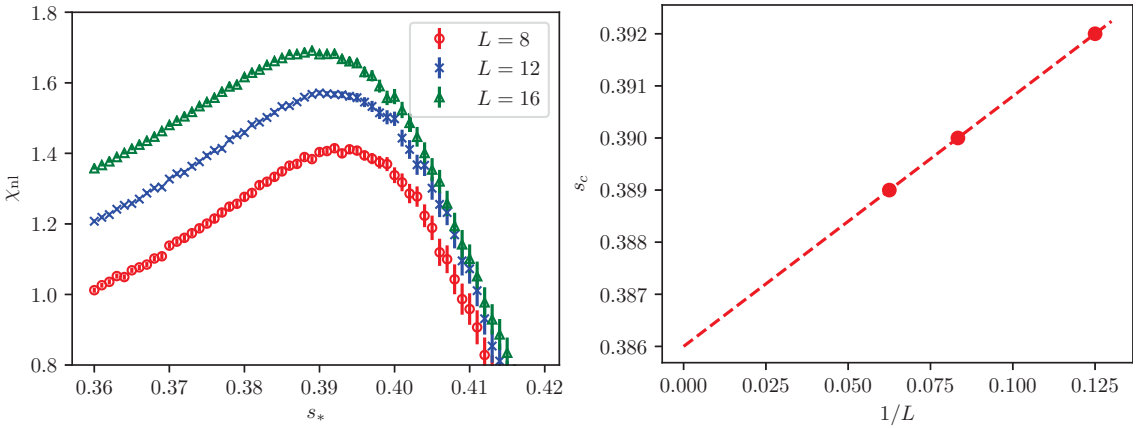

Figure 5.5.: (Left) Global nonlinear susceptibility for each system size obtained from the D-Wave machine. The aspect ratio of the figure is the same as Fig. 5.3. (Right) peak point (which corresponds to the phase transition point s_c) as a function of inverse system size $1/L$. The result is almost the same as that of global linear susceptibility.

Carlo ($\nu \sim 1.5$, see Chapter 4). One of the possible reasons for this inconsistent behavior comes from the magnetic flux from superconducting qubits in the D-Wave machine, which may affect other flux qubits and result in larger correlation length and a broader peak in susceptibilities. Note that these behaviors of the susceptibilities may affect the data of histogram of susceptibilities, which will be discussed later.

We also calculate global nonlinear susceptibility which is shown on the left panel of Fig. 5.5 where the aspect ratio is the same as the global linear susceptibility in Fig. 5.3. Although the peak is a little bit narrower compared to the global linear susceptibility, the peak position is the same as that of global linear susceptibility, leading to the same critical point $s_c \sim 0.386$ in the infinite system size limit as shown on the right panel of Fig. 5.5.

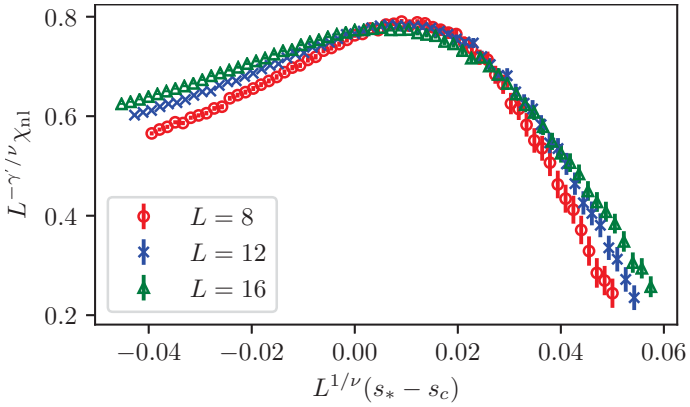

Figure 5.6.: Finite size scaling analysis on the global nonlinear susceptibility with parameters $\nu = 5$, $s_c = 0.386$, and $\gamma'/\nu = 0.28$.

Figure 5.6 shows the finite size scaling analysis on the global nonlinear susceptibility. [4)]

We find that the critical exponent of the nonlinear susceptibility γ' is larger than that of linear susceptibility γ, indicating a stronger divergence than the linear susceptibility.

5.2.3. Histograms of global susceptibilities

In this section we show the histogram of the susceptibilities obtained from the D-Wave machine which corresponds to Section 4.2.2. Figure 5.7 shows the histogram of the global linear susceptibility with the pause point $s_* = 0.365$ which is far from the critical point. [5)] We find that, even for the D-Wave machine, a similar behavior to the quantum Monte Carlo, power-law decay which is independent of the system size in the large susceptibility region, is observed. Besides, we also observe the large tail distribution in the small susceptibility region especially for the system with small size. This large tail can be explained by considering the phenomenon which is observed in the histogram of the magnetization in 5.1 where we have seen samples of magnetization which still have values ± 1 even in the paramagnetic region. These samples of magnetization may make the system behave as if it was in a ferromagnetic state, resulting in a large tail behavior especially for the small system size.

Nevertheless we can apply a linear fitting in the large susceptibility region. Comparing the relation which is expected to hold especially in the large susceptibility region explained in Chapter 3,

$$\log P(\chi) \sim -\left(\frac{d}{z'} + 1\right) \log \chi, \tag{5.10}$$

We can conclude that d/z' is around 12 for this pause point $s_* = 0.365$.

The distribution $P(\chi)$ with the pause points $s_* = 0.369, 0.375$, and 0.38 which is closer to the critical point than the above case is shown in Figs. 5.8, 5.9, and 5.10 respectively.

[4)] In this chapter we define the critical exponent of the nonlinear susceptibility as

$$\chi_{\mathrm{nl}} \sim \left|\frac{s_* - s_c}{s_c}\right|^{-\gamma'}, \tag{5.8}$$

as an analogy of the linear susceptibility,

$$\chi \sim \left|\frac{s_* - s_c}{s_c}\right|^{-\gamma}. \tag{5.9}$$

[5)] When applying a fitting to obtain d/z', we first exclude the data with $P(\chi) \leq 10^{-2}$ since these data are not reliable.

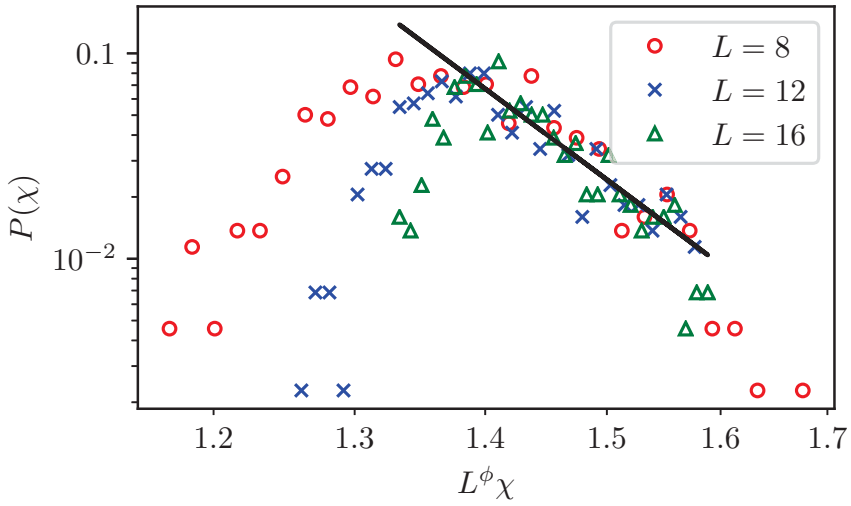

Figure 5.7.: Log-log plot of the histogram $P(\chi)$ of the global linear susceptibility χ obtained from the D-Wave machine with the pause point $s_* = 0.365$ (far from the critical point). The notations in this figure are the same as in Fig. 4.15. The black solid line shows a fit to data whose slope is 14.7±1.74, which indicates that the exponent d/z' is around 13.7

Although the data look similar to Fig. 5.7, the exponent d/z' obtained from the data is remarkably smaller than the data from the case $s_* = 0.365$ and we also observe that the exponent d/z' decays monotonically as we close to the critical point $s_c = 0.386$. This monotonic decay of the exponent d/z' is qualitatively consistent with the result from the quantum Monte Carlo simulation.

The region above the critical point, $s_* = 0.394$, is shown on Fig. 5.11. We find that no power-law decay behavior is observed from the data. Besides, we also find that $P(\chi)$ monotonically increases as the global linear susceptibility χ increases. The same behavior is observed on the histogram of local linear susceptibility obtained by quantum Monte Carlo as shown in Fig. 4.11.

The same power-law decay of the histogram is also observed even in the case of the global nonlinear susceptibility. Figure 5.12 shows the histogram $P(\chi_{\mathrm{nl}})$ in the paramagnetic region $s_* = 0.365$. The data shows the similar behavior compared to that of the global linear susceptibility $P(\chi)$ though the slope is smaller than the linear susceptibility $P(\chi)$, which is reasonable taking the relation,

$$\log P(\chi_{\mathrm{nl}}) \sim -\left(\frac{d}{3z'} + 1\right) \log \chi_{\mathrm{nl}}, \tag{5.11}$$

into consideration. The histograms of the global nonlinear susceptibility with the pause point $s_* = 0.369, 0.375$, and 0.38 (closer to the critical point) are shown on Figs. 5.13, 5.14, and 5.15. We observe that d/z' roughly decreases monotonically, which is the same as the global linear susceptibility.

The relation between the exponent d/z' and the pause point s_* is shown in Fig. 5.16. From this figure one can show the behavior is almost the same as the result from the quantum Monte Carlo in that the exponent d/z' decreases monotonically towards the phase transition point as can confirmed from the bottom panel of Fig. 5.16. Taking the error bars of d/z' into consideration, the region $d/z' < 3$ can exist, implying that the divergence of the nonlinear susceptibilities induced by the quantum Griffiths singularity may occur.

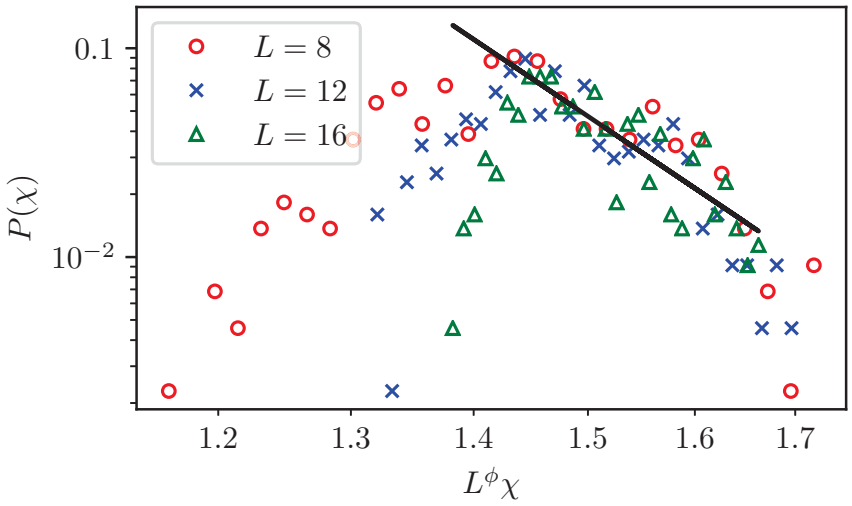

Figure 5.8.: Log-log plot of the histogram $P(\chi)$ of the global linear susceptibility χ obtained from the D-Wave machine with the pause point $s_* = 0.369$. The black solid line shows a fit to data whose slope is 12.29±2.03, which indicates that the exponent d/z' is around 11.29.

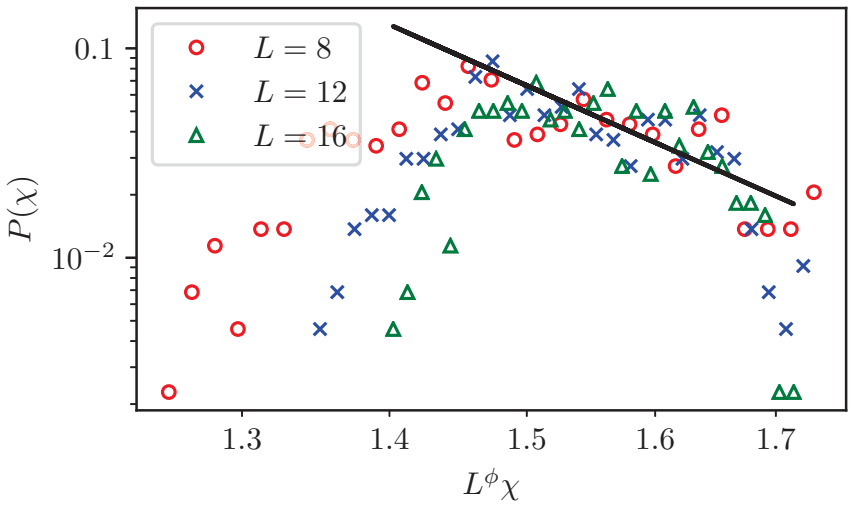

Figure 5.9.: Log-log plot of the histogram $P(\chi)$ of the global linear susceptibility χ obtained from the D-Wave machine with the pause point $s_* = 0.375$. The black solid line shows a fit to data whose slope is 9.7±2.07, which indicates that the exponent d/z' is around 8.7.

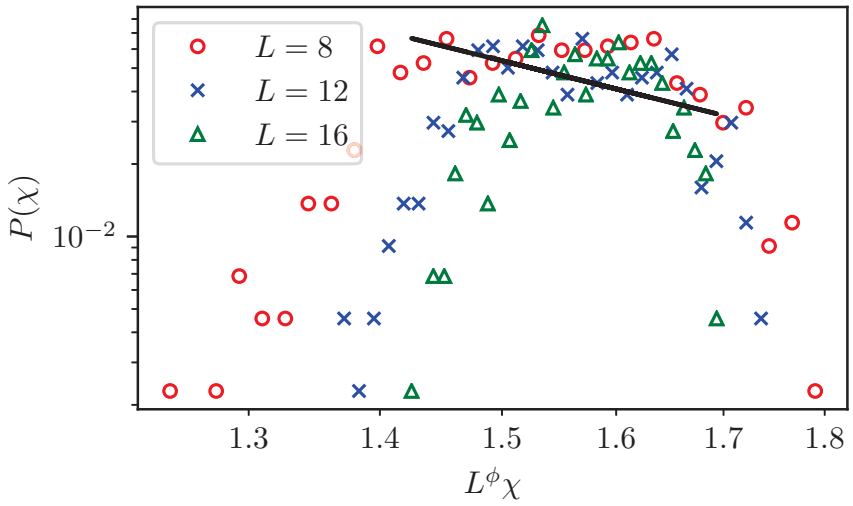

Figure 5.10.: Log-log plot of the histogram $P(\chi)$ of the global linear susceptibility χ obtained from the D-Wave machine with the pause point $s_* = 0.38$. The black solid line shows a fit to data whose slope is 4.18 ±2.47, which indicates that the exponent d/z' is around 3.18.

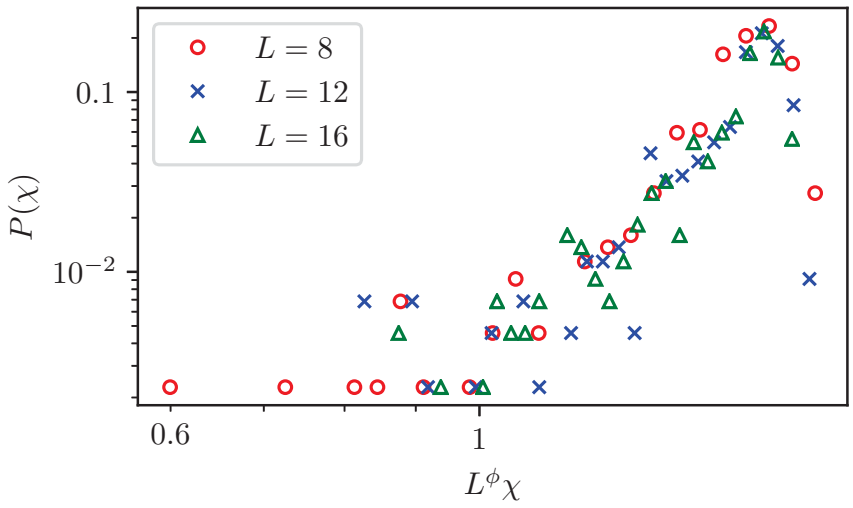

Figure 5.11.: Log-log plot of the histogram $P(\chi)$ of the global linear susceptibility χ obtained from the D-Wave machine with the pause point $s_* = 0.394$ (above the critical point). No power-law decay behavior is observed on this figure and $P(\chi)$ roughly grows monotonically as the global linear susceptibility increases.

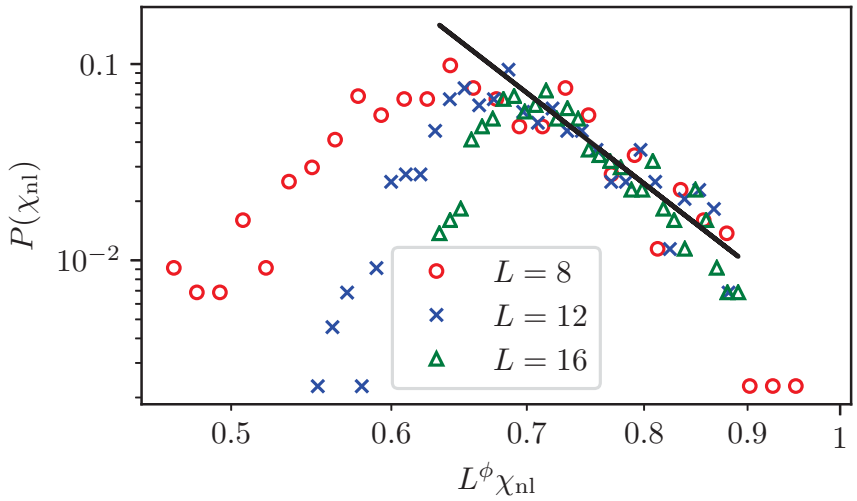

Figure 5.12.: Log-log plot of the histogram $P(\chi_{\mathrm{nl}})$ of the global nonlinear susceptibility χ_{nl} obtained from the D-Wave machine with the pause point $s_* = 0.365$ (far from the critical point). Black solid line shows a fit to data whose slope is 7.982±1.06, which indicates that the exponent $d/3z'$ is around 6.982.

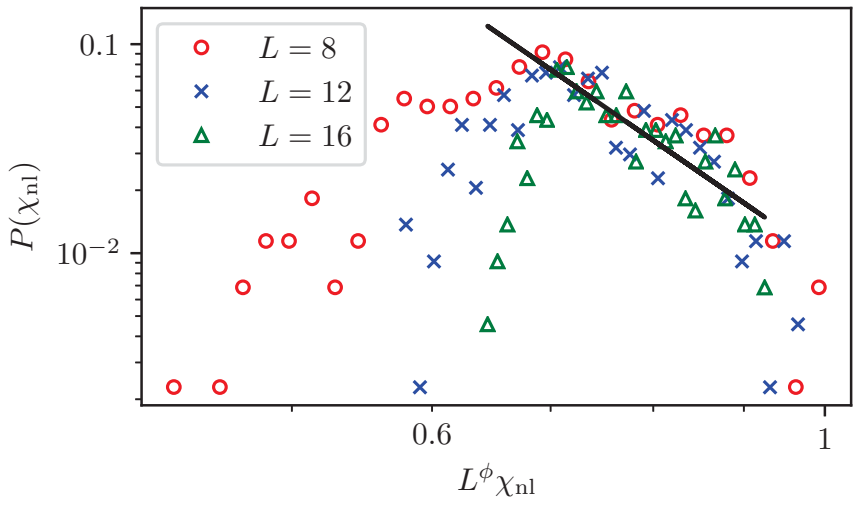

Figure 5.13.: Log-log plot of the histogram $P(\chi_{\mathrm{nl}})$ of the global nonlinear susceptibility χ_{nl} obtained from the D-Wave machine with the pause point $s_* = 0.369$ (far from the critical point). Black solid line shows a fit to data whose slope is 5.843±0.86, which indicates that the exponent $d/3z'$ is around 4.843.

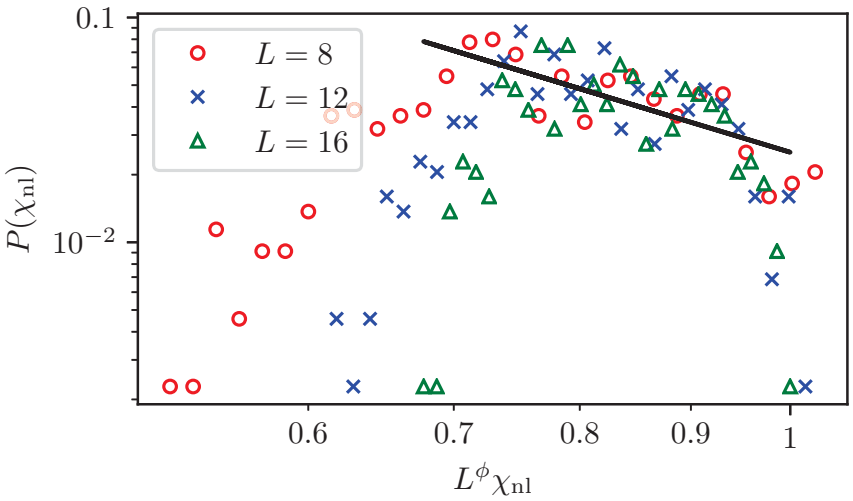

Figure 5.14.: Log-log plot of the histogram $P(\chi_{\mathrm{nl}})$ of the global nonlinear susceptibility χ_{nl} obtained from the D-Wave machine with the pause point $s_* = 0.375$ (far from the critical point). Black solid line shows a fit to data whose slope is 2.9±0.88, which indicates that the exponent $d/3z'$ is around 1.9.

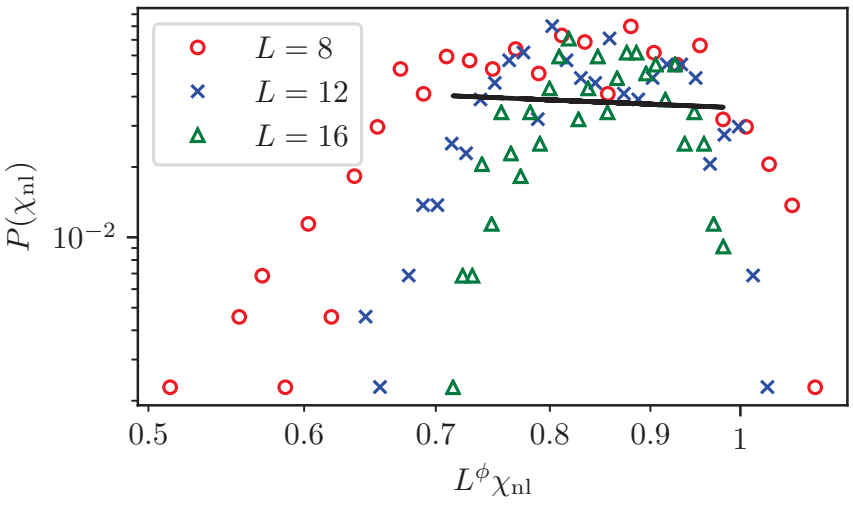

Figure 5.15.: Log-log plot of the histogram $P(\chi_{\mathrm{nl}})$ of the global nonlinear susceptibility χ_{nl} obtained from the D-Wave machine with the pause point $s_* = 0.38$ (far from the critical point). Black solid line shows a fit to data whose slope is 0.3±1.4, which indicates that the exponent $d/3z'$ is around -0.7.

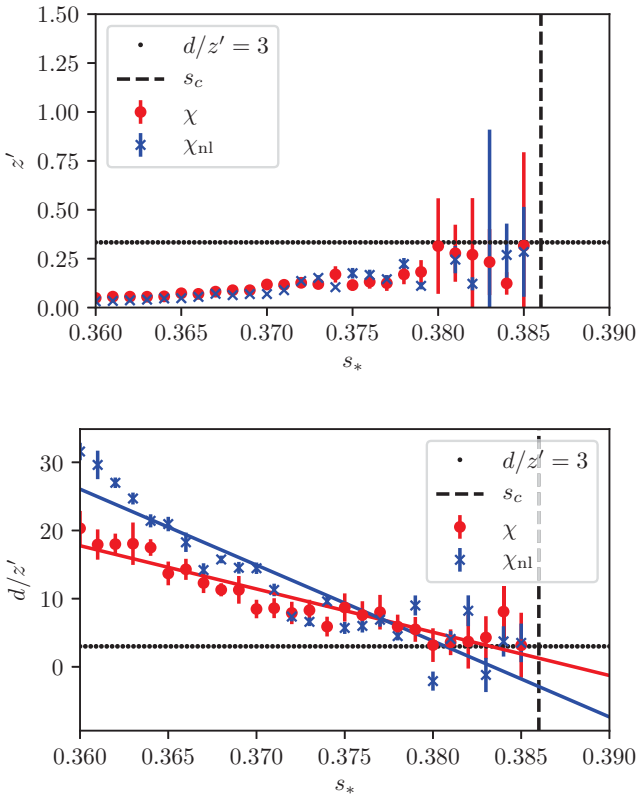

Figure 5.16.: (Top) Log-log plot of the exponent z' as a function of the pause point s_*. Solid curve is just a guide for eye. (Bottom) the same as the top figure but the vertical axis shows the exponent d/z'. Since the slope of the histogram from the D-Wave machine deviates especially in the vicinity of the critical point, error bars are added to the plot.

5.2.4. Summary and discussion

In this chapter we carried out experiments on the D-Wave machine aiming at the detection of the Griffiths-McCoy singularity. From the histogram of the magnetizations, we can see a clear sign of phase transition as shown in Fig. 5.1 although the precise phase transition point cannot be determined from physical quantities such as the Binder ratio and magnetization due to the samples of magnetizations which stick to ± 1 even in the paramagnetic region unlike the quantum Monte Carlo method in Chapter 4. Besides, from the data of susceptibility we can observe a clear peak near the phase transition point and the value can be determined as $s_* \sim 0.386$.

To check if this obtained phase transition point is consistent with the result obtained by the quantum Monte Carlo simulation, we now relate the factors between quantum Monte Carlo and the D-Wave machine, that is, pause point s_* and the pair of the inverse temperature and the transverse field (β, Γ) used on the quantum Monte Carlo simulation by comparing the exponents of the Boltzmann factors as

$$\exp\left[-\beta_{\text{phys}} H(s)\right] \sim \exp\left[-\beta H\right], \tag{5.12}$$

where $\beta_{\text{phys}} \sim 12\text{mK}$ is the physical temperature inside the D-Wave device and the Hamiltonians $H(s)$ and H denote the Hamiltonian of the D-Wave device and the quantum Monte Carlo method respectively, [6)]

$$H(s) = -\frac{A(s)}{2}\left(\sum_i \hat{\sigma}_i^x\right) + \frac{B(s)}{2}\left(\frac{1}{2}\sum_{\langle i,j\rangle} J_{ij}\hat{\sigma}_i^z\hat{\sigma}_j^z\right), \tag{5.13}$$

$$H = \sum_{\langle i,j\rangle} J_{ij}\hat{\sigma}_i^z\hat{\sigma}_j^z - \Gamma\sum_i \hat{\sigma}_i^x. \tag{5.14}$$

It is expected that the quantity Γ converted from the critical point s_{*c} of the D-Wave machine coincides with the critical point of the transverse field calculated by quantum Monte Carlo method. Assuming that the exponents of Eq. 5.12 are the same, we obtain the relations between s_* and (β, Γ) as follows,

$$\beta = \frac{\beta_{\text{phys}} B(s_*)}{4}, \tag{5.15}$$

$$\Gamma = \frac{2A(s_*)}{B(s_*)}, \tag{5.16}$$

or with units,

$$\beta = \frac{1}{k_B\ \text{J}\cdot\text{K}^{-1} \times 12\text{mK}} \frac{B(s_*)\ \text{GHz} \times h\ \text{J}\cdot\text{s}}{4}, \tag{5.17}$$

$$\Gamma = \frac{2A(s_*)\ \text{GHz} \times h\ \text{J}\cdot\text{s}}{B(s_*)\ \text{GHz} \times h\ \text{J}\cdot\text{s}}, \tag{5.18}$$

where h and k_B denote the Planck constant and the Boltzmann constant. Figure 5.17 shows the relations Eqs. (5.17) and (5.18). From the figure we read that the critical point $s_* = 0.386$ corresponds to the parameter $\beta = 2.49$ and $\Gamma = 1.37$ in quantum Monte Carlo method. On the other hand, according to the left panel of Fig. 4.3, we also see that the quantum Monte Carlo method exhibits phase transition at the point $\Gamma \sim 1.6$ with the temperature $\beta = 2.49$ ($T = 1/\beta \sim 0.4$). We find these two transverse fields are close enough to show that the D-Wave machine can exhibit the same critical point as the quantum Monte Carlo, though they do not have completely the same values. Besides, our

[6)] Remember that the interactions J_{ij} in the D-Wave machine is set to be half smaller.

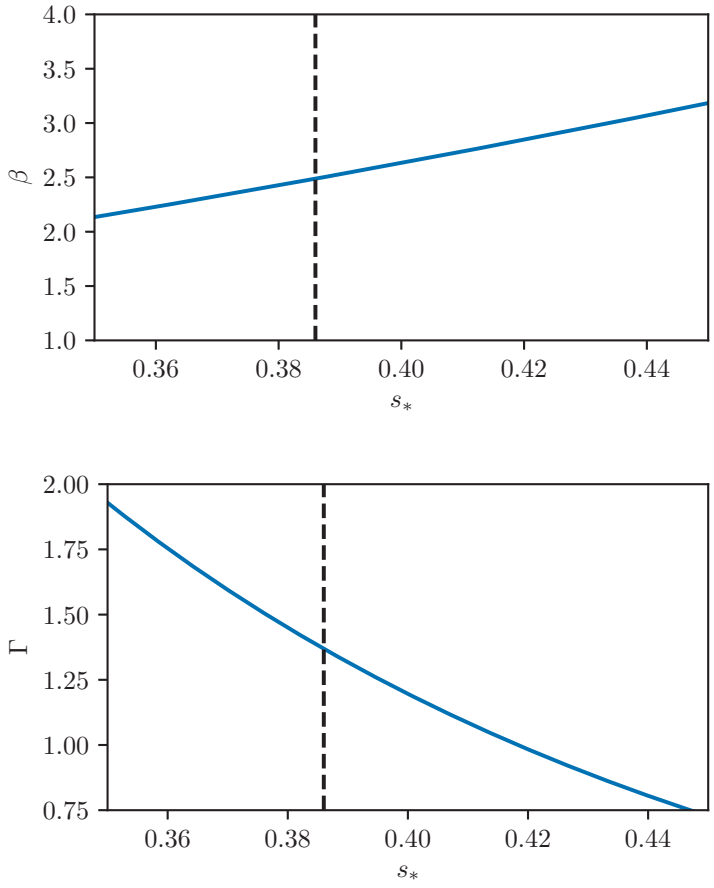

Figure 5.17.: The relation between the pause point s_* and the parameters (β, Γ). Black dashed line shows the point $s_* = s_c = 0.386$ at which $\beta = 2.49$ and $\Gamma = 1.37$.

experiment could not ensure the correspondence of the other quantities (such as critical exponents) to quantum Monte Carlo.

As for the exponent d/z', we can show that the behave is almost qualitatively the same as the quantum Monte Carlo. We observe that the exponent d/z' monotonically decreases near the phase transition point and the region $d/z' < 3$ can exist taking the error bars in Fig. 5.16 into consideration.

One may argue that the systematic error affects the result of the histogram of the susceptibilities. However, if the noise effect is dominant, the histogram is expected to behave the Gaussian-like function, resulting in independence of d/z' as a function of s_*. Since d/z' has a clear dependence as a function of s_* and decreases monotonically, it can be said that the above results are induced by the quantum Griffiths effect.

6. Conclusion

In this study we demonstrate one of the established physical phenomena, the Griffiths-McCoy singularity on the D-Wave quantum annealer motivated by the previous studies of the demonstration of quantum phase transition on the machine [17, 18].

Chapters 2 and 3 show the preliminaries of the study. In Chapter 2 we introduce the historical background of quantum annealing and its peripheral topics, especially the topics of the D-Wave machine and its applications to simulation of classical and quantum Boltzmann distribution. Chapter 2 also shows the introduction of the D-Wave machine from technical aspects. In Chapter 3 we explain the Griffiths-McCoy singularity which we demonstrate on the D-Wave machine and show that the histogram of susceptibilities is a reasonable indicator to detect the divergence induced by this singularity.

Chapters 4 and 5 are the main part of the thesis and we perform both quantum simulations: quantum Monte Carlo on a large-scale classical computer and experiments on the D-Wave machine aiming to observe the Griffiths-McCoy singularity. Even though the result from the D-Wave machine contains non-negligible noise effect, we observe that the machine exhibits the clear quantum phase transition point which is consistent to the result obtained by the quantum Monte Carlo simulation, while the other properties such as critical exponents do not necessarily coincide with the result obtained by the quantum Monte Carlo method. As for the exponent d/z' which characterizes the Griffith-McCoy singularity, the D-Wave machine shows qualitatively the same behavior where d/z' decreases monotonically. Although it is hard to give a conclusion that the region $d/z' < 3$, which indicates the divergence of the nonlinear susceptibility, exists in the paramagnetic region since d/z' obtained from the D-Wave machine has large deviation near the critical point, it can be said that the monotonically decrease of d/z' indicates that the D-Wave machine captures the quantum Griffiths effect.

There remains some tasks to be considered towards the more accurate quantum simulation on a physical quantum annealer. One is the improvement of accuracy of the result from the D-Wave machine. Although some error-mitigation tricks are applied which are elucidated in Appendix D, there remains noise in the result from the D-Wave machine some of which hampers the accurate estimates of the phase transition point. One of the obstacles is the quench process in the anneal-pause-quench protocol itself, which makes the system biased to the ferromagnetic state. Since this obstacle is owing to the interface of the D-Wave device itself, it can be technically eliminated by allowing the annealing schedule which is not $s = 1$ at the end of the annealing. Other obstacles may come from such as the noise from environment or magnetic flux inside the quantum annealer, which seems not to be solved immediately. Recently published white paper from the D-Wave systems [61] announces that the device with low environment noise is developed. Therefore it is expected that this new device will mitigate the noise effect and exhibit more accurate results, which enables us to perform more detailed analysis of the physical phenomena including critical exponents of the system.

One may raise the question: "is there a meaning to perform the quantum simulation of the quantum annealer that can also be performed on existing classical computer?". As demonstrated in Chapter 4, the observation of Griffiths-McCoy singularity itself can be observed by using quantum Monte Carlo method. The main difference between the D-Wave machine and quantum Monte Carlo method is, as stated in Chapter 1, the D-Wave machine generate the real quantum state inside the device whereas the quantum

Monte Carlo is a stochastic simulation. Simulating the quantum Griffiths singularity on the D-Wave machine is of great significance in terms of physical realization of this physical phenomenon on the real quantum device, not a simulation on a classical computer. Moreover, there is an advantage of simulating physical phenomena on a real quantum device over using quantum Monte Carlo method. It has been known that the large-scale quantum Monte Carlo method can be applied only to the special case of the quantum systems which are often referred to as "stoquastic" Hamiltonian [62]. Although the system with transverse magnetic field is categorized in the stoquastic Hamiltonian, systems with other kind of quantum terms may not be categorized in this group and hence cannot be simulated by quantum Monte Carlo. By using real quantum device these kind of problem can be overcome easily by introducing the corresponding quantum terms directly in the device. As for the D-Wave machine, they succeeded a demonstration of introducing quantum term which is known to be "nonstoquastic" which cannot be dealt with quantum Monte Carlo [63]. In near-term future it may be possible to perform large-scale quantum simulation that cannot perform on quantum Monte Carlo method by using real quantum device such as the D-Wave machine. This approach may open the door to the large-scale quantum simulator that cannot be performed on conventional classical computers.

A. Suzuki-Trotter Decomposition

In general it is a formidable task to investigate statistical properties of quantum systems since an exact summation of partition function

$$Z = \mathrm{Tr} e^{-\beta \hat{H}} \tag{A.1}$$

requires huge calculation time that grows exponentially as a function of system size.

Even though the same difficulty arises in the case of classical model, the established algorithm Markov-chain Monte Carlo (MCMC) method enables us to reduce the calculation time drastically, whereas this algorithm cannot be applied directly to a quantum model.

The studies by Suzuki and Trotter [64, 65] pointed out that the partition function of d dimensional quantum system can be interpreted to that of corresponding $d+1$ dimensional classical model. With this mapping, often referred to as Suzuki-Trotter decomposition, we can compute the d dimensional quantum system efficiently by mapping into $d+1$ dimensional classical system then apply MCMC algorithm.

Assume that we have a transverse field Ising model Hamiltonian with interactions J_{ij},

$$H(\hat{\boldsymbol{\sigma}}) = -\sum_{i<j} J_{ij} \hat{\sigma}_i^z \hat{\sigma}_j^z - \Gamma \sum_i \hat{\sigma}_i^x. \tag{A.2}$$

The partition function is denoted as

$$Z(\beta, \Gamma) = \mathrm{Tr} \exp\{-\beta H(\hat{\boldsymbol{\sigma}})\}. \tag{A.3}$$

Applying Lie-Trotter formula,

$$e^{\hat{A}+\hat{B}} = \lim_{P\to\infty} \left(e^{\hat{A}/N} e^{\hat{B}/N} \right)^N, \tag{A.4}$$

and inserting identity operators with the basis of Pauli-z eigenstates $|\pm 1\rangle$,

$$\hat{1} = \sum_{\sigma=\pm 1} |\sigma\rangle \langle\sigma|, \tag{A.5}$$

in the partition function gives

$$
\begin{aligned}
Z(\beta,\Gamma) &= \mathrm{Tr}\exp(-\beta H(\hat{\boldsymbol{\sigma}})) \\
&= \mathrm{Tr}\exp\left(\beta\sum_{i<j}J_{ij}\hat{\sigma}_i^z\hat{\sigma}_j^z+\beta\Gamma\sum_i\hat{\sigma}_i^x\right) \\
&= \mathrm{Tr}\exp(-\beta\hat{H}_z-\beta\hat{H}_x) \\
&= \lim_{P\to\infty}\mathrm{Tr}\left[\exp\left(-\frac{\beta}{P}\hat{H}_z\right)\exp\left(-\frac{\beta}{P}\hat{H}_x\right)\right]^P \\
&= \lim_{P\to\infty}\mathrm{Tr}\,\langle\boldsymbol{\sigma}(0)|\exp\left(-\frac{\beta}{P}\hat{H}_z\right)|\boldsymbol{\sigma}(1)\rangle\langle\boldsymbol{\sigma}(1)|\exp\left(-\frac{\beta}{P}\hat{H}_x\right) \\
&\times\exp\left(-\frac{\beta}{P}\hat{H}_z\right)|\boldsymbol{\sigma}(2)\rangle\langle\boldsymbol{\sigma}(2)|\exp\left(-\frac{\beta}{P}\hat{H}_x\right) \\
&\times\exp\left(-\frac{\beta}{P}\hat{H}_z\right)|\boldsymbol{\sigma}(3)\rangle\langle\boldsymbol{\sigma}(3)|\exp\left(-\frac{\beta}{P}\hat{H}_x\right) \\
&\cdots \\
&\times\exp\left(-\frac{\beta}{P}\hat{H}_z\right)|\boldsymbol{\sigma}(P)\rangle\langle\boldsymbol{\sigma}(P)|\exp\left(-\frac{\beta}{P}\hat{H}_x\right)|\boldsymbol{\sigma}(0)\rangle\,,
\end{aligned}
\tag{A.6}
$$

where

$$
\hat{H}_z \equiv -\sum_{i<j}J_{ij}\hat{\sigma_i^z}\hat{\sigma_j^z}, \tag{A.7}
$$

$$
\hat{H}_x \equiv -\Gamma\sum_i\hat{\sigma_i^x}, \tag{A.8}
$$

and the states $|\boldsymbol{\sigma}(t)\rangle$ $[0\le t\le P]$ are the product of each basis for sites $\prod_i|\sigma_i(t)\rangle$. The variable t denotes the Trotter index. Owing to the following equations,

$$
\langle\sigma_i(t)|\exp\left(\frac{\beta}{P}\Gamma\hat{\sigma_i^x}\right)|\sigma_i(t+1)\rangle = Ae^{B\sigma_i(t)\sigma_i(t+1)}, \tag{A.9}
$$

$$
A = \sqrt{\frac{1}{2}\sinh\frac{2\beta\Gamma}{P}}, \tag{A.10}
$$

$$
B = \frac{1}{2}\log\coth\frac{\beta\Gamma}{P}, \tag{A.11}
$$

we obtain the corresponding effective Hamiltonians as shown below, [1)]

$$
H_{\mathrm{eff}}(\boldsymbol{\sigma}) = -\sum_{i<j}\sum_{t=1}^{P}\frac{\beta}{P}J_{ij}\sigma_i(t)\sigma_j(t)-\sum_i\sum_{t=1}^{P}B\sigma_i(t)\sigma_i(t+1), \tag{A.12}
$$

$$
Z(\beta,\Gamma) = \mathrm{Tr}\exp\left(-\tilde{H}_{\mathrm{eff}}(\boldsymbol{\sigma})\right), \tag{A.13}
$$

where the symbol Tr in Eq.(A.13) represents the sum over all classical spins,

$$
\{S_i,\sigma_i(t)=\pm1|1\le i\le N,1\le t\le P\}\,. \tag{A.14}
$$

The derived Hamiltonian is nothing but a classical Ising model with an extra dimension owing to the Trotter index. Although this formulation can be applied formally to general

[1)] The coefficient A can be omitted because it does not affect any physical quantities derived from the partition function.

quantum model, we have to be aware of a caveat of the formulation. Remember that the coefficient B in Eq.(A.12) is defined at Eq.(A.11). If Γ takes a negative value, B becomes a complex variable because of a negative argument in log function. In that case the MCMC algorithm can then no longer be applied because of the existence of negative probability. This feature has been known as an infamous *negative sign problem*.

Although the negative sign problem can be eliminated in the case of transverse field Ising model by applying local gauge transformation $\{\hat{\sigma}_i^x, \hat{\sigma}_i^y, \hat{\sigma}_i^z\} \to \{-\hat{\sigma}_i^x, -\hat{\sigma}_i^y, \hat{\sigma}_i^z\}$ for each spin, there is no trivial method to eliminate the sign problem for general model, whose model is often referred to as *nonstoquastic* model. [66]

Moreover, recent study shows that a certain curing negative sign problem turns out to be NP-complete problem. [67]. Finding an efficient method of eliminating negative sign problem is thus of great importance since it can be applied to large-scale quantum simulation.

B. Details of GPU-based Monte Carlo method

B.1. Markov-chain Monte Carlo method

Suppose that we want to generate a sequence of spins $\boldsymbol{\sigma} \equiv \{\sigma_1, \sigma_2, \cdots\}$ following the canonical distribution,

$$P(\boldsymbol{\sigma}) = \frac{e^{-H(\boldsymbol{\sigma})}}{Z}, \tag{B.1}$$

This task is going to be impractical if we deal with relatively large system since we need to evaluate the value of the partition function $Z \equiv \sum_{\boldsymbol{\sigma}} e^{-H(\boldsymbol{\sigma})}$ whose summation grows exponentially as a function of system size. The Markov-chain Monte Carlo (MCMC) solves the problem by introducing a proper stochastic process which generates a sequence of spins $\{\boldsymbol{\sigma} \to \boldsymbol{\sigma'} \to \boldsymbol{\sigma''} \to \cdots\}$ (Markov-chain) whose distribution matches the desired distribution $P(\boldsymbol{\sigma})$ in a long-time limit. The stochastic process is often determined according to the following condition,

$$P(\boldsymbol{\sigma'}|\boldsymbol{\sigma})P(\boldsymbol{\sigma}) = P(\boldsymbol{\sigma}|\boldsymbol{\sigma'})P(\boldsymbol{\sigma'}), \tag{B.2}$$

where $P(\boldsymbol{\sigma'}|\boldsymbol{\sigma})$ denotes the stochastic process which represents the probability the state $\boldsymbol{\sigma}$ goes to the state $\boldsymbol{\sigma'}$. The above condition is often referred to as *detailed balance condition* and has been proved that the statement that $P(\boldsymbol{\sigma'}|\boldsymbol{\sigma})$ satisfies the detailed balance condition is sufficient for the statement that $P(\boldsymbol{\sigma'}|\boldsymbol{\sigma})$ makes the Markov-chain converge to the target distribution $P(\boldsymbol{\sigma})$. [1)] The choice of the stochastic process $P(\boldsymbol{\sigma'}|\boldsymbol{\sigma})$ then characterizes the algorithm of MCMC.

One of the most established algorithm is known as *Metropolis-Hasting* algorithm which is proposed by Metropolis and Hasting [69, 70]. In this algorithm, the state gets changed if the proposed states lowers the total energy and if not, the state will be changed with a probability which depends on the difference of the energy between the original and the proposed state. A naive Metropolis-Hasting process, single spin flip algorithm, is shown on Algorithm 1. Although this single spin flip algorithm can be applied to system with arbitrary interactions, it intrinsically has a problem that the state tends to be stuck in a local minimum on the energy surface during the MCMC process. This phenomenon occurs especially on a spin-glass type Hamiltonian with a low temperature region. To avoid this difficulty and accelerate the equilibration, *replica exchange Monte Carlo method* is often combined with the single spin flip algorithm. [71] This method runs systems with different parameters (e.g. temperature and the strength of the transverse field) each other simultaneously and exchanges the spin configurations following the Metropolis-Hasting criteria. With this method, the system which is stuck in a local minimum will be put under higher temperature (or larger transverse field) and is expected to escape from the local minimum. The procedure of the method is listed on Algorithm 2 where $\{\boldsymbol{\sigma}^{(1,\beta_1)}, \boldsymbol{\sigma}^{(2,\beta_2)}, \cdots \boldsymbol{\sigma}^{(M,\beta_M)}\}$ denotes M copied systems with different parameters β_1 to

[1)] Note that the detailed balance condition is *not* a necessary condition. One of the most notable study which employs a stochastic process without satisfying the detailed balance condition is done by Suwa and Todo [68].

Algorithm 1 Single spin flip algorithm for generating $\boldsymbol{\sigma}_{\text{new}}$ from $\boldsymbol{\sigma}_{\text{old}}$ with system size N

function SINGLE-SPIN-FLIP($\boldsymbol{\sigma}_{\text{old}}$)
  $\boldsymbol{\sigma} \leftarrow \boldsymbol{\sigma}_{\text{old}}$
  for $i = 1$ to N **do**
    $\boldsymbol{\sigma'} \leftarrow \boldsymbol{\sigma}$ with a single spin randomly chosen and flipped
    generate r from the uniform distribution from 0 to 1
    if $\exp\left[-(H(\boldsymbol{\sigma'}) - H(\boldsymbol{\sigma}))\right] > r$ **then**
      $\boldsymbol{\sigma} \leftarrow \boldsymbol{\sigma'}$
  $\boldsymbol{\sigma}_{\text{new}} \leftarrow \boldsymbol{\sigma}$
  return $\boldsymbol{\sigma}_{\text{new}}$

Algorithm 2 Replica exchange Monte Carlo combined with single spin flip algorithm

function REPLICA-EXCHANGE-MONTE-CARLO($\{\boldsymbol{\sigma}^{(1,\beta_1)}, \boldsymbol{\sigma}^{(2,\beta_2)}, \cdots \boldsymbol{\sigma}^{(M,\beta_M)}\}$)
  for $i = 1$ to N_{ss} **do**
    for $j = 1$ to M **do**
      $\boldsymbol{\sigma}^{(j,\beta_j)} \leftarrow$ SINGLE-SPIN-FLIP($\boldsymbol{\sigma}^{(j,\beta_j)}$)
  for $i = 1$ to $M - 1$ **do**
    $\Delta E \leftarrow (H(\boldsymbol{\sigma}^{(i+1,\beta_i)}) + H(\boldsymbol{\sigma}^{(i,\beta_{i+1})})) - (H(\boldsymbol{\sigma}^{(i,\beta_i)}) + H(\boldsymbol{\sigma}^{(i+1,\beta_{i+1})}))$
    generate r from the uniform distribution from 0 to 1
    if $\exp\left[-\Delta E\right] > r$ **then**
      Swap spin configurations between $\boldsymbol{\sigma}^{(i,\beta_i)}$ and $\boldsymbol{\sigma}^{(i+1,\beta_{i+1})}$
  return $\{\boldsymbol{\sigma}^{(1,\beta_1)}, \boldsymbol{\sigma}^{(2,\beta_2)}, \cdots \boldsymbol{\sigma}^{(M,\beta_M)}\}$

β_M sorted in ascending order and the exchange step occurs every N_{ss} Monte Carlo steps. An extension of the method to multiple parameters is straightforward.

In the case of quantum Monte Carlo where the partition function has a matrix operator such as

$$Z = \mathrm{Tr} e^{-\hat{H}}, \tag{B.3}$$

We can use the same algorithms by applying Suzuki-Trotter decomposition (see Appendix A) to convert d dimensional quantum system to $d+1$ dimensional classical system.

B.2. Markov-chain Monte Carlo parallelized by GPU

Even if we employ sophisticated MCMC algorithms, the growth of equilibration time cannot be inevitable as system size increases. In our situation on Chapter 4, the maximum system size (the number of spins including Trotter slices) we have to deal with is around 86,400,000, which seems to require enormous calculation time to make the system equilibrated.

Recent progress of *general-purpose computing on graphics processing units* (GPGPU) technique enables us to pave the way to simulate a quite large system in a practical time. GPGPU uses graphics processing units (GPU), which is typically used only for calculation of computer graphics, as a calculator for general purposes which have been the task for CPU. Unlike CPU, GPU has quite a lot of processing cores, though each of which is inferior to that in CPU. GPU is hence suited for parallel computing where many processes in the task can be carried out simultaneously. Notable applications of GPU are for instance, large-scale matrix computation, physics simulation such as fluid dynamics, rendering in computer graphics, and more.

As for MCMC algorithm, parallel computing should be performed carefully since the system has to be developed sequentially following the proper Markov process to generate Markov-chain. Inappropriate MCMC update by parallel scheme results in violation of Markov-chain, i.e., the distribution of the system is no longer guaranteed to converge to the target distribution.

An example of a drastic acceleration of MCMC algorithm using parallel computing can be seen especially when we deal with a Hamiltonian with sparse connectivity. Remember that the model we are going to simulate in this study is a chimera graph with Trotter direction. Owing to its sparsity, the spins in the model can be divided into two sectors where no two adjacent spins are located on the same sector. Since the difference of the energy of the system by a flip of spin in the sector is determined only by configurations of spins in the other sector, the spins in the same sector can perform single spin flip algorithm in parallel. The N steps single spin flip for each Monte Carlo step is thus reduced to only 2 steps. Replica exchange Monte Carlo method is also parallelized by applying similar technique since the exchange process between two systems is independent of spin configuration of other systems. The modified algorithms for parallel computing is listed on Algorithms 3 and 4.

B.3. Data analysis

After we store systems $\boldsymbol{\sigma}$ for each Monte Carlo step to generate a sequence of samples, $\{\boldsymbol{\sigma} \to \boldsymbol{\sigma}' \to \boldsymbol{\sigma}'' \to \cdots\}$ using the above MCMC algorithms, our next task will be to extract statistical information of physical quantities from this Markov-chain.

If the systems in the sequence are totally uncorrelated, the mean μ and the standard

Algorithm 3 Parallel single spin flip algorithm for generating $\boldsymbol{\sigma}_{\text{new}}$ from $\boldsymbol{\sigma}_{\text{old}}$ with system size N

function SINGLE-SPIN-FLIP($\boldsymbol{\sigma}_{\text{old}}$)
  $\boldsymbol{\sigma} \leftarrow \boldsymbol{\sigma}_{\text{old}}$
  divide $\boldsymbol{\sigma}$ into two sectors $\boldsymbol{\sigma}^{(1)}$ and $\boldsymbol{\sigma}^{(2)}$

  for σ in $\boldsymbol{\sigma}^{(1)}$ **do in parallel**
    $\boldsymbol{\sigma'}^{(1)} \leftarrow \boldsymbol{\sigma}^{(1)}$ with spin σ flipped
    generate r from the uniform distribution from 0 to 1
    if $\exp\left[-(H(\boldsymbol{\sigma'}^{(1)}) - H(\boldsymbol{\sigma}^{(1)}))\right] > r$ **then**
      flip spin σ in $\boldsymbol{\sigma}^{(1)}$

  for σ in $\boldsymbol{\sigma}^{(2)}$ **do in parallel**
    $\boldsymbol{\sigma'}^{(2)} \leftarrow \boldsymbol{\sigma}^{(2)}$ with spin σ flipped
    generate r from the uniform distribution from 0 to 1
    if $\exp\left[-(H(\boldsymbol{\sigma'}^{(2)}) - H(\boldsymbol{\sigma}^{(2)}))\right] > r$ **then**
      flip spin σ in $\boldsymbol{\sigma}^{(2)}$

  $\boldsymbol{\sigma}_{\text{new}} \leftarrow \boldsymbol{\sigma}$
  return $\boldsymbol{\sigma}_{\text{new}}$

Algorithm 4 Parallel replica exchange Monte Carlo combined with single spin flip algorithm

function REPLICA-EXCHANGE-MONTE-CARLO($\{\boldsymbol{\sigma}^{(1,\beta_1)}, \boldsymbol{\sigma}^{(2,\beta_2)}, \cdots \boldsymbol{\sigma}^{(M,\beta_M)}\}$)
  for $i = 1$ to N_{ss} **do**
    for $j = 1$ to M **do in parallel**
      $\boldsymbol{\sigma}^{(j,\beta_j)} \leftarrow$ SINGLE-SPIN-FLIP($\boldsymbol{\sigma}^{(j,\beta_j)}$)

  for $k = 1$ to $\lfloor M/2 \rfloor$ **do in parallel**
    $i \leftarrow 2k - 1$
    $\Delta E \leftarrow (H(\boldsymbol{\sigma}^{(i+1,\beta_i)}) + H(\boldsymbol{\sigma}^{(i,\beta_{i+1})})) - (H(\boldsymbol{\sigma}^{(i,\beta_i)}) + H(\boldsymbol{\sigma}^{(i+1,\beta_{i+1})}))$
    generate r from the uniform distribution from 0 to 1
    if $\exp[-\Delta E] > r$ **then**
      Swap spin configurations between $\boldsymbol{\sigma}^{(i,\beta_i)}$ and $\boldsymbol{\sigma}^{(i+1,\beta_{i+1})}$

  for $k = 1$ to $\lfloor M/2 \rfloor$ **do in parallel**
    $i \leftarrow 2k$
    $\Delta E \leftarrow (H(\boldsymbol{\sigma}^{(i+1,\beta_i)}) + H(\boldsymbol{\sigma}^{(i,\beta_{i+1})})) - (H(\boldsymbol{\sigma}^{(i,\beta_i)}) + H(\boldsymbol{\sigma}^{(i+1,\beta_{i+1})}))$
    generate r from the uniform distribution from 0 to 1
    if $\exp[-\Delta E] > r$ **then**
      Swap spin configurations between $\boldsymbol{\sigma}^{(i,\beta_i)}$ and $\boldsymbol{\sigma}^{(i+1,\beta_{i+1})}$

  return $\{\boldsymbol{\sigma}^{(1,\beta_1)}, \boldsymbol{\sigma}^{(2,\beta_2)}, \cdots \boldsymbol{\sigma}^{(M,\beta_M)}\}$

error SE of a certain physical quantity $f(\boldsymbol{\sigma})$ will be

$$\mu = \langle f(\boldsymbol{\sigma}) \rangle = \frac{1}{N_{\text{seq}}} \sum_{k=1}^{N_{\text{seq}}} f(\boldsymbol{\sigma}_k), \tag{B.4}$$

$$SE = \sqrt{\frac{\langle f(\boldsymbol{\sigma})^2 \rangle - \langle f(\boldsymbol{\sigma}) \rangle^2}{N_{\text{seq}}}} = \sqrt{\frac{1}{N_{\text{seq}}} \left[\left(\frac{1}{N_{\text{seq}}} \sum_{k=1}^{N_{\text{seq}}} f(\boldsymbol{\sigma}_k)^2 \right) - \left(\frac{1}{N_{\text{seq}}} \sum_{k=1}^{N_{\text{seq}}} f(\boldsymbol{\sigma}_k) \right)^2 \right]}, \tag{B.5}$$

where $\boldsymbol{\sigma}_k$ denotes kth element (i.e., kth Monte Carlo step) of Markov-chain and N_{seq} is the number of samples. In fact, the true standard error is larger than estimated one in Eq. (B.5) owing to correlations. A straightforward calculation shows that the modified standard error $\tilde{SE}$ is given by

$$\tilde{SE} = \sqrt{SE^2 + \frac{2\tau}{N_{\text{seq}}}}, \tag{B.6}$$

where τ is known as *autocorrelation time* defined as

$$\tau = \sum_{k=1}^{N_{\text{seq}}-1} \left(1 - \frac{k}{N_{\text{seq}}} \right) \frac{\langle f(\boldsymbol{\sigma}_k) f(\boldsymbol{\sigma}_0) \rangle - \langle f(\boldsymbol{\sigma}_k) \rangle \langle f(\boldsymbol{\sigma}_0) \rangle}{\langle f(\boldsymbol{\sigma})^2 \rangle - \langle f(\boldsymbol{\sigma}) \rangle^2}. \tag{B.7}$$

Since an exact calculation of τ is in general a troublesome task, an alternative method, *log binning*, is commonly used to compute the true SE. During log binning, we store only the mean value of $f(\boldsymbol{\sigma})$ from 2^m th step to $2^{m+1} - 1$th step,

$$\langle f(\boldsymbol{\sigma}) \rangle_m = \frac{1}{2^m} \sum_{k=2^m}^{2^{m+1}-1} f(\boldsymbol{\sigma}_k) \tag{B.8}$$

every 2^m Monte Carlo steps ($m \geq 0$). In the large Monte Carlo step limit, the taken samples can be assumed to be nearly uncorrelated so that we can apply the same formula as Eq. (B.5). There are mainly two other advantages of log binning. First, we need to store only m averaged physical quantities out of 2^m Monte Carlo steps, which enables us to reduce the memory significantly. Second, the plot of averaged physical quantities as a function of a logarithm of Monte Carlo steps exhibits a clear equilibration behavior. The data fluctuates before equilibration and converges to a certain value after the system gets equilibrated. We should then fetch the data from the Monte Carlo step when the system is equilibrated. An example of log binning is in Fig. B.1. After gaining uncorrelated samples, we are now ready to investigate the behavior of the system near the critical point, which is elucidated in the next appendix.

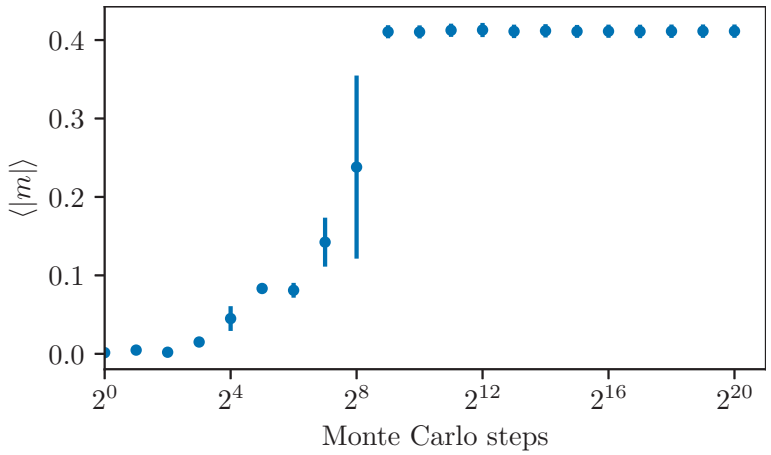

Figure B.1.: An example of log binning. The horizontal axis shows the log-scale of Monte Carlo steps and the vertical axis shows a physical quantity (absolute magnetization in this example). The point at the 2^m th Monte Carlo step shows the mean and the standard deviation of the quantity averaged from 2^m th step to $2^{m+1} - 1$th step. One can see that the quantity gets converged at the 2^8th Monte Carlo step, which indicates that the system gets equilibrated.

C. Finite-size scaling analysis on a quantum critical point

To investigate statistical properties related to phase transition, we have to deal with systems in a thermodynamic limit, i.e. infinite-size limit. Since we can perform numerical calculations only with finite system size which exhibits in principle no phase transitions, we have to extract information by computing the systems with different sizes and performing a extrapolation to infinite-size limit.

Finite-size scaling analysis is a established method and is conventionally used for the extrapolation. We elucidate the detailed method and how to determine physical properties such as quantum critical point and critical exponents given physical quantities of finite-size system.

C.1. Definitions of critical exponents

Before entering the topic let us give a brief review of the critical exponents.

Near the quantum critical point at zero temperature, various physical quantities such as susceptibilities exhibit singular behavior which is characterized by the power-law as a function of the distance from the critical point, Quantum phase transition is characterized as

$$r = \frac{\Gamma - \Gamma_c}{\Gamma_c}, \tag{C.1}$$

where Γ_c denotes the quantum critical point. Definitions of the critical exponents are summarized in Table C.1. Note that in the presence of quenched disorder, there is the

Table C.1.: List of critical exponents. d denotes the dimension of the system and ξ_τ denotes the correlation length along the Trotter direction.

	exponent	definition
specific heat	α	$c \sim \lvert r\rvert^{-\alpha}$
magnetization	β	$\lvert m\rvert \sim \lvert r\rvert^{\beta}$
susceptibility	γ	$\chi \sim \lvert r\rvert^{-\gamma}$
correlation length	ν	$\xi \sim \lvert r\rvert^{-\nu}$
correlation function	η	$G(\boldsymbol{x}) \sim \lvert \boldsymbol{x}\rvert^{-d+2-\eta}$
dynamical critical exponent	z	$\xi_\tau \sim \xi^z$
activated dynamical scaling	ψ	$\log \xi_\tau \sim \xi^\psi$

case the divergence of ξ_τ have exponential scaling, $\log \xi_\tau \sim \xi^\psi$, which is often referred to as *activated dynamical scaling*.

These critical exponents are not independent each other and connected by the scaling

relations. Some relations are listed below: [1)]

$$\alpha + 2\beta + \gamma = 2, \tag{C.2}$$
$$\nu(2 - \eta) = \gamma, \tag{C.3}$$
$$2 - \alpha = (d + z)\nu. \tag{C.4}$$

C.2. Finite-size scaling analysis with a fixed temperature

In this section we first introduce the method for finite-size scaling analysis with a fixed temperature for simplicity of explanation.

Assume that one want to determine the critical exponent of particular physical quantity which behaves near the critical point as

$$A(r) \sim |r|^{-\rho}. \tag{C.5}$$

In the region $L \gg \xi$ where the system size is larger than correlation length, using the relation $\xi \sim |r|^{-\nu}$ leads to

$$A(r) \sim \xi^{\rho/\nu}, \tag{C.6}$$

while in the region $L \ll \xi$, $A(r)$ explicitly depends on the system size as

$$A(r) \sim L^{\rho/\nu}. \tag{C.7}$$

Taking these relation into consideration, $A(r)$ can be represented as

$$A(r) \sim \xi^{\rho/\nu} f(L/\xi), \tag{C.8}$$

where the scaling function $f(x)$ is defined as

$$f(x) = \begin{cases} \text{const.} & \text{if } x \gg 1 \ (L \gg \xi), \\ x^{\rho/\nu} & \text{if } x \ll 1 \ (L \ll \xi). \end{cases} \tag{C.9}$$

Rewriting the scaling function to $\tilde{f}(x) = x^{-\rho} f(x^{\nu})$ gives

$$A(r) \sim L^{\rho/\nu} \tilde{f}(L^{1/\nu}(\Gamma - \Gamma_c)), \tag{C.10}$$

where

$$\tilde{f}(x) = \begin{cases} L^{-\rho/\nu}(\Gamma - \Gamma_c)^{-\rho} & \text{if } x \gg 1 \ (L \gg \xi), \\ \text{const.} & \text{if } x \ll 1 \ (L \ll \xi). \end{cases} \tag{C.11}$$

It follows that $\tilde{f}(x)$ is independent of system size in the vicinity of the critical point where $\Gamma \to \Gamma_c$ and $L \ll \xi$ if we choose proper Γ_c, ν, and ρ. With these parameters, plotting $L^{-\rho/\nu} A(r)$ as a function of $L^{1/\nu}(\Gamma - \Gamma_c)$ makes the data with different system sizes collapse onto the single curve of $\tilde{f}(x)$. We can determine the three unknown parameters, namely critical point, critical exponents of correlation length and the physical quantity $A(r)$ simultaneously by applying this data collapse technique.

If we choose $A(r)$ to *binder ratio* g which is defined as [2)]

$$g = \frac{1}{2}\left(3 - \frac{\langle m^4 \rangle}{\langle m^2 \rangle^2}\right), \tag{C.12}$$

[1)] The classical counterpart of Eq. (C.4) is $2 - a = d\nu$. In the case of quantum phase transition, d is replaced with $d + z$ owing to Trotter direction which scales as L^z.

[2)] $\langle \cdots \rangle$ denotes the thermal average.

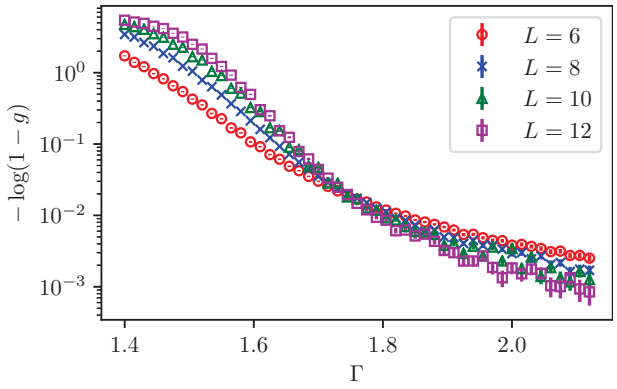

Figure C.1.: An example of the binder ratio for each system size (the same figure as the left panel of Fig. 4.2. In this plot we use $-\log(1-g)$ instead of the original binder ratio to see the crossing point more clearly. We find that all plots with different sizes cross on the point near $\Gamma \sim 1.7$, which indicates that the critical point is near $\Gamma \sim 1.7$.

where m shows the magnetization, the critical exponent is fixed to zero since g takes the value which is independent of system size at the critical point as can be confirmed by the following relations,

$$\langle m^2 \rangle \sim |r|^{2\beta} \tag{C.13}$$

$$, \langle m^4 \rangle \sim |r|^{4\beta} \tag{C.14}$$

$$, g = \frac{1}{2}\left(3 - \frac{\langle m^4 \rangle}{\langle m^2 \rangle^2}\right) \sim |r|^0 \sim \text{const.}. \tag{C.15}$$

The relation (C.10) can thus be rewritten with only two parameters,

$$g \sim \tilde{f}(L^{1/\nu}(\Gamma - \Gamma_c)). \tag{C.16}$$

Hence it might be convenient to apply the data collapse of binder ratio to determine Γ_c and ν first then determine the critical exponent of other physical quantities.

Note that the binder ratio g is also useful to estimating the initial guess of the transition point Γ_c. In the vicinity of the zero temperature (or zero transverse field), the variables $\langle m^2 \rangle$ and $\langle m^4 \rangle$ are close to unity hence g is also close to unity. In the paramagnetic region, physical quantities such as spins will behave randomly. It follows the averaged physical quantities such as $\langle m^2 \rangle$ and $\langle m^4 \rangle$ can be regarded as second and fourth moment of the Gaussian distribution, which gives the following relation,

$$\langle m^4 \rangle = 3 \langle m^2 \rangle^2 . \tag{C.17}$$

It follows that the binder ratio g goes zero in the paramagnetic region. In the vicinity of the critical point g takes value which is independent of the system size as stated above. For these reasons, One should plot g for each system size and find the crossing point which is expected to be located on the critical point. An example is shown on Fig. C.1. In this example, we should estimate the initial guess of the critical point as 1.7.

Although one has to consider the zero temperature limit when considering quantum phase transition, we believe that the universal behavior of the system such as critical exponent remain unchanged.

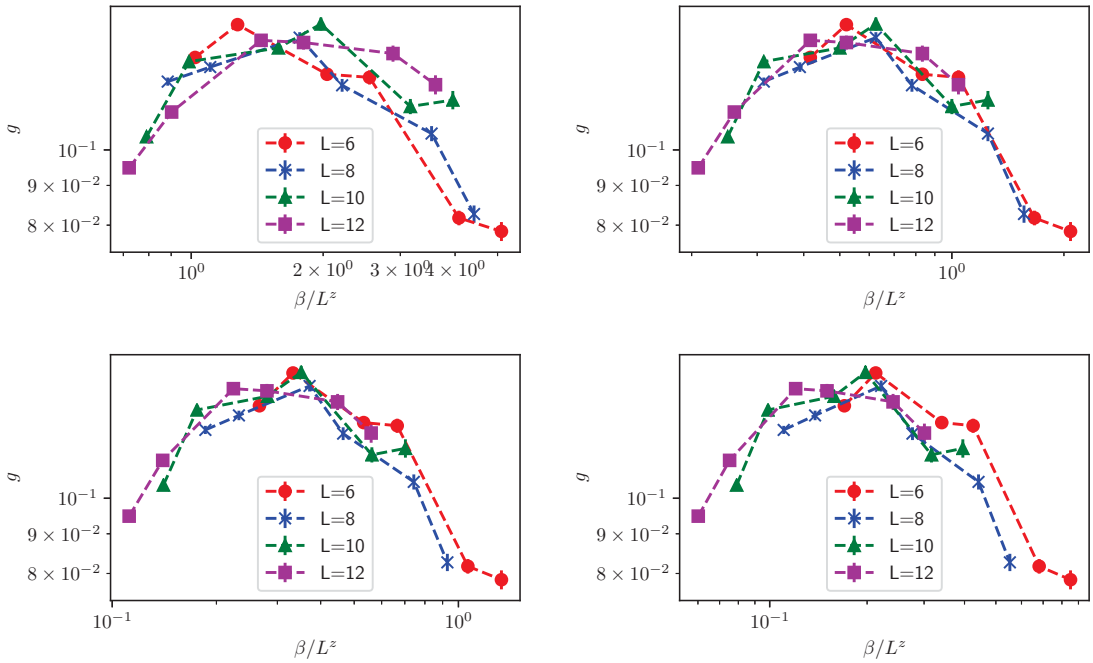

Figure C.2.: Binder ratio g of sparse chimera graph (see Chapter 4) with different sizes as a function of β/L^z at the critical point where $\beta \sim M$. The dynamical critical exponent z is set to $z = 0.5$ (left top), $z = 1.0$ (right top), $z = 1.25$ (left bottom), and $z = 1.5$ (right bottom). The figure is the same as Fig. 4.7

C.3. Finite-size scaling analysis on a quantum system

In the previous section we introduced finite-size scaling method with a fixed temperature. When taking quantum phase transition (zero temperature limit) into consideration, we have to apply finite-size scaling to Trotter direction. In the case of the binder ratio, the modified scaling function will be

$$g \sim \tilde{f}(L^{1/\nu}(\Gamma - \Gamma_c), M/L^z), \tag{C.18}$$

where z denotes dynamical critical exponents and M represents the number of Trotter slices. At the critical point $\Gamma = \Gamma_c$, the scaling function depends only on M/L^z. Thus in the case z takes finite value, one can find the dynamical exponent by tuning z so that the binder ratio g as a function of M/L^z exhibits the clear data collapse. An example is shown on Fig. C.2. Each plot shows the binder ratio as a function of β/L^z where β is set to near M and we can observe that setting z to 1 makes data collapse onto a single curve most precisely. If the data collapse fails for any z, it means that the z is infinity: one should apply activated dynamical scaling.

The scaling function in Eq. (C.10) is also modified as

$$A(r) \sim L^{\rho/\nu} \tilde{f}(L^{1/\nu}(\Gamma - \Gamma_c), M/L^z). \tag{C.19}$$

If we set the aspect ratio M/L^z to a constant value, Eq. (C.19) reduces to the scaling function with a single argument which is the same as Eq. (C.19) hence we can use the same method elucidated in Section C.2.

D. Techniques for reducing noise in the D-Wave quantum annealer

In Chapter 2 we introduced an application of the D-Wave machine for simulation of quantum Ising model and the anneal-pause-quench protocol for making the system thermally equilibrated. In addition to the above techniques, an error-mitigation process should be considered in order to use the D-Wave machine as a practical quantum simulator. Since the D-Wave machine is intrinsically an analog device, not a conventional digital computer, the derived result is severely affected by various obstacles such as environmental noise. Some of the most remarkable ones come from deficiencies of superconducting flux qubits, namely inhomogeneous characteristics of each qubit and interference of magnetic flux in other qubits. We can immediately observe the failure of the simulation caused by the above deficiencies by running simple experiments on the D-Wave machine without any tunings. For instance, if we set all interactions J_{ij} and local fields h_i to zero to the machine, the configurations of spins are expected to behave randomly hence the thermal average of each spin is around 0, whereas the derived result seems to be biased and thermal averages have finite values as shown in Fig. Moreover, if we set all interactions J_{ij} to ferromagnetic variables (say -1) and sample several times, the machine is expected to exhibit all-up or all-down spin configurations with the same probability owing to its spin-reversal symmetry, whereas the actual result contains only all-up spin configurations that means we cannot simulate spin-reversal symmetric system properly.

In the following sections we elucidate how to overcome these obstacles and show that the above difficulties can be mitigated to a certain extent.

D.1. Calibrating individual flux bias

We first focus on the first obstacle: inhomogeneous characteristics of each qubits. Since we cannot make the superconducting flux qubits with completely the same characteristics, each flux qubit has individuality in principle. As shown in Fig., Some of the flux qubits tend to have spin-up direction while the others tend to have spin-down direction. This bias can be modeled as an effective local field which we call *flux bias* and the task is to eliminate its individuality by calibrating individual flux bias. As for the D-Wave machine, this effective local field can be controlled through the "flux-biases" option and the task is to search the optimal flux bias for each flux qubits where the thermal average of each spin becomes zero. An algorithm for searching the optimal flux for each flux qubit using binary search is listed on algorithm. [1)]

D.2. Gauge averaging

Next we focus on the second factor: interference of magnetic flux in other qubits. Even if there is no interaction J_{ij} between two flux qubits, the magnetic flux from the one flux qubit might affect the other qubit, resulting in an emergence of an effective ferromagnetic interaction between two qubits. This phenomenon hampers the correct calculation

[1)] $\{a_i\}$ in algorithm chart denotes a set of variables $\{a_1, a_2, \cdots\}$.

Algorithm 5 Binary search algorithm for finding the optimal flux bias for individual qubit

$h_i^{\text{flux}} \leftarrow$ flux bias of ith flux qubit
$h_i^{\text{up}} \leftarrow$ initial guess (positive value) of upper bound of flux bias of ith flux qubit
$h_i^{\text{low}} \leftarrow$ initial guess (negative value) of lower bound of flux bias of ith flux qubit
$N \leftarrow$ system size
$N_{\text{rep}} \leftarrow$ number of repetitions

function DWAVE($\{h_i^{\text{flux}}\}$)
    Set flux bias of ith qubit to h_i^{flux} for each qubit
    Set interactions J_{ij} and local fields h_i to zero
    perform anneal-pause-quench protocol on the D-Wave machine
    calculate thermal average of spin m_i for each qubit
    return $\{m_i\}$

function BINARY-SEARCH($\{h_i^{\text{up}}\}, \{h_i^{\text{down}}\}$)
    loop
        $\{m_i\} =$ DWAVE($\{h_i^{\text{up}}\}$)
        if $\frac{1}{N}\sum_{i=1}^{N} m_i > 0.5$ **then**
            break
        for $i = 1$ to N **do**
            $h_i^{\text{up}} \leftarrow 2h_i^{\text{up}}$

    loop
        $\{m_i\} =$ DWAVE($\{h_i^{\text{down}}\}$)
        if $\frac{1}{N}\sum_{i=1}^{N} m_i < -0.5$ **then**
            break
        for $i = 1$ to N **do**
            $h_i^{\text{down}} \leftarrow 2h_i^{\text{down}}$

    for $r = 1$ to N_{rep} **do**
        for $i = 1$ to N **do**
            $(pivot)_i \leftarrow (1/2)(h_i^{\text{up}} + h_i^{\text{down}})$
        $\{m_i\} =$ DWAVE($\{(pivot)_i\}$)
        for $i = 1$ to N **do**
            if $m_i > 0$ **then**
                $h_i^{\text{up}} \leftarrow (pivot)_i$
            else
                $h_i^{\text{down}} \leftarrow (pivot)_i$

    $\{h_i^{\text{flux}}\} = \{(1/2)(h_i^{\text{up}} + h_i^{\text{down}})\}$
    return $\{h_i^{\text{flux}}\}$

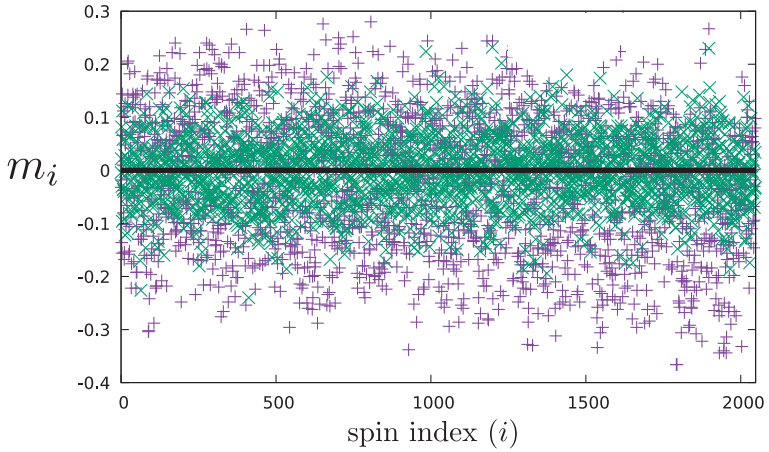

Figure D.1.: Average spin configuration for each site over 100 runs of annealing. Purple dots show the result without applying error mitigation and green dots show the one with error mitigation.

especially in the case of the random ferromagnetic interactions where the effective ferromagnetic interaction forces the spins to align to the same direction.

Gauge averaging is the technique to eliminate this effective ferromagnetic interaction by introducing random ± 1 variables $\{\epsilon_i\}$ and applying following gauge transformations:

$$J_{ij} \to J_{ij}\epsilon_i\epsilon_j, \tag{D.1}$$

$$\hat{\sigma}_i{}^z \to \hat{\sigma}_i{}^z\epsilon_i, \tag{D.2}$$

which remains the total Hamiltonian invariant. We can easily apply the technique by only replacing interactions J_{ij} to $J_{ij}\epsilon_i\epsilon_j$ and flip the ith spin if $\epsilon_i = -1$ for all derived spins.

D.3. Results

In this section we show how these error mitigation techniques affect the result of the D-Wave machine.

D.3.1. Zero interaction

We first prepare the Hamiltonian

$$H(s) = -\frac{A(s)}{2}\left(\sum_i \hat{\sigma}_i^x\right) + \frac{B(s)}{2}\left(\sum_{\langle i,j\rangle} J_{ij}\hat{\sigma}_i^z\hat{\sigma}_j^z\right), \tag{D.3}$$

where all interactions J_{ij} are set to zero. We next measure the spin configuration for each site averaged over 100 runs of annealing,

$$m_i = \sum_{a=1}^{100} \sigma_i^a, \tag{D.4}$$

which is expected to take the value near zero. Figure D.1 shows m_i for each site before and after applying the error mitigation techniques. Purple dots and green dots show the result before and after applying the error mitigation respectively. We observe that m_i of the data without error mitigation tend to have values which are far from zero even if the interactions are set to zero. This behavior comes from individualities of each flux qubit.

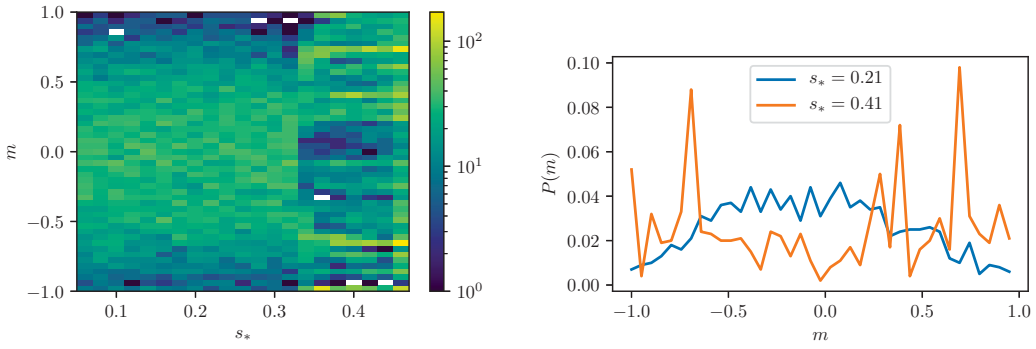

Figure D.2.: (Left) Histogram (color map) of magnetization without error mitigation. Notations are the same as Fig. 5.1. (Right) Histograms of magnetization without error mitigation where the pause point s_* is fixed to 0.21 (paramagnetic phase) and 0.41 (ferromagnetic phase)

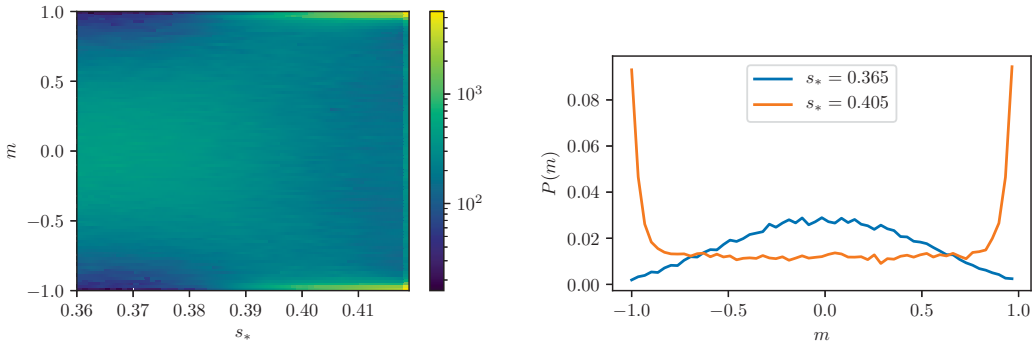

Figure D.3.: (Left) Histogram (color map) of magnetization after applying error mitigation. (Right) Histogram of magnetization after applying error mitigation where the pause point s_* is fixed to 0.21 (paramagnetic phase) and 0.41 (ferromagnetic phase). These figures are the same as Fig. 5.1.

As for the data with error mitigation, we can see that m_i has much smaller deviation and the values are closer to zero than the one without error mitigation. It follows that the above error mitigation techniques reduces individualities of each flux qubits and work effectively.

D.3.2. Sparse chimera graph

Next we apply the techniques to sparse chimera graph (see Chapter 5 for definition) and see how the result changes by applying error mitigation. Figure D.2 shows the histogram of magnetization without any error mitigation. We can see that there are multiple peaks of magnetizations in the ferromagnetic region, where the magnetization is expected to have peaks at ± 1, due to systematic errors on the D-Wave machine. Even if we can see the behavior of phase transition around $s_* = 0.35$, it seems quite a hard task to extract informations of physical quantities from this data.

Figure D.3 shows the data after applying error mitigation process. Unlike the data without error mitigation, we can clearly observe peaks only at ± 1 in the ferromagnetic region, which is consistent to a theory of statistical mechanics. From these data we confirm that the error mitigation process is quite effective and inevitable for demonstrating quantum simulation on the D-Wave machine.

References

[1] R. Feynman, "Simulating physics with computers," *International Journal of Theoretical Physics*, vol. 21, pp. 467–488, 1982.

[2] M. A. Nielsen and I. L. Chuang, *Quantum Computation and Quantum Information: 10th Anniversary Edition*. Cambridge University Press, 2010.

[3] L. K. Grover, "A fast quantum mechanical algorithm for database search," *ACM Symposium on Theory of Computing*, 1996.

[4] P. W. Shor, "Polynomial-Time Algorithms for Prime Factorization and Discrete Logarithms on a Quantum Computer," *SIAM Journal on Computing*, vol. 26, no. 5, pp. 1484–1509, 1997.

[5] A. W. Harrow, A. Hassidim, and S. Lloyd, "Quantum algorithm for linear systems of equations," *Phys. Rev. Lett.*, vol. 103, p. 150502, Oct 2009.

[6] F. Arute, K. Arya, R. Babbush, D. Bacon, J. C. Bardin, R. Barends, R. Biswas, S. Boixo, F. G. S. L. Brandao, D. A. Buell, B. Burkett, Y. Chen, Z. Chen, B. Chiaro, R. Collins, W. Courtney, A. Dunsworth, E. Farhi, B. Foxen, A. Fowler, C. Gidney, M. Giustina, R. Graff, K. Guerin, S. Habegger, M. P. Harrigan, M. J. Hartmann, A. Ho, M. Hoffmann, T. Huang, T. S. Humble, S. V. Isakov, E. Jeffrey, Z. Jiang, D. Kafri, K. Kechedzhi, J. Kelly, P. V. Klimov, S. Knysh, A. Korotkov, F. Kostritsa, D. Landhuis, M. Lindmark, E. Lucero, D. Lyakh, S. Mandrà, J. R. McClean, M. McEwen, A. Megrant, X. Mi, K. Michielsen, M. Mohseni, J. Mutus, O. Naaman, M. Neeley, C. Neill, M. Y. Niu, E. Ostby, A. Petukhov, J. C. Platt, C. Quintana, E. G. Rieffel, P. Roushan, N. C. Rubin, D. Sank, K. J. Satzinger, V. Smelyanskiy, K. J. Sung, M. D. Trevithick, A. Vainsencher, B. Villalonga, T. White, Z. J. Yao, P. Yeh, A. Zalcman, H. Neven, and J. M. Martinis, "Quantum supremacy using a programmable superconducting processor," *Nature*, vol. 574, no. 7779, pp. 505–510, 2019.

[7] J. Preskill, "Quantum Computing in the NISQ era and beyond," *Quantum*, vol. 2, p. 79, Aug. 2018.

[8] T. Kadowaki and H. Nishimori, "Quantum annealing in the transverse Ising model," *Phys. Rev. E.*, vol. 58, pp. 5355–5363, Nov 1998.

[9] M. W. Johnson, P. Bunyk, F. Maibaum, E. Tolkacheva, A. J. Berkley, E. M. Chapple, R. Harris, J. Johansson, T. Lanting, I. Perminov, E. Ladizinsky, T. Oh, and G. Rose, "A scalable control system for a superconducting adiabatic quantum optimization processor," *Supercond. Sci. Technol.*, vol. 23, no. 6, p. 065004, 2010.

[10] A. J. Berkley, M. W. Johnson, P. Bunyk, R. Harris, J. Johansson, T. Lanting, E. Ladizinsky, E. Tolkacheva, M. H. S. Amin, and G. Rose, "A scalable readout system for a superconducting adiabatic quantum optimization system," *Supercond. Sci. Technol.*, vol. 23, no. 10, p. 105014, 2010.

[11] R. Harris, M. W. Johnson, T. Lanting, A. J. Berkley, J. Johansson, P. Bunyk, E. Tolkacheva, E. Ladizinsky, N. Ladizinsky, T. Oh, F. Cioata, I. Perminov, P. Spear, C. Enderud, C. Rich, S. Uchaikin, M. C. Thom, E. M. Chapple, J. Wang, B. Wilson, M. H. S. Amin, N. Dickson, K. Karimi, B. Macready, C. J. S. Truncik, and G. Rose, "Experimental investigation of an eight-qubit unit cell in a superconducting optimization processor," *Phys. Rev. B.*, vol. 82, p. 024511, Jul 2010.

[12] V. S. Denchev, S. Boixo, S. V. Isakov, N. Ding, R. Babbush, V. Smelyanskiy, J. Martinis, and H. Neven, "What is the computational value of finite-range tunneling?," *Phys. Rev. X*, vol. 6, p. 031015, Aug 2016.

[13] S. Mandrà, Z. Zhu, W. Wang, A. Perdomo-Ortiz, and H. G. Katzgraber, "Strengths and weaknesses of weak-strong cluster problems: A detailed overview of state-of-the-art classical heuristics versus quantum approaches," *Phys. Rev. A*, vol. 94, p. 022337, Aug 2016.

[14] T. Albash, V. Martin-Mayor, and I. Hen, "Temperature scaling law for quantum annealing optimizers," *Phys. Rev. Lett.*, vol. 119, p. 110502, Sep 2017.

[15] A. Mishra, T. Albash, and D. A. Lidar, "Finite temperature quantum annealing solving exponentially small gap problem with non-monotonic success probability," *Nature Communications*, vol. 9, no. 1, p. 2917, 2018.

[16] M. H. Amin, "Searching for quantum speedup in quasistatic quantum annealers," *Phys. Rev. A*, vol. 92, p. 052323, Nov 2015.

[17] R. Harris, Y. Sato, A. J. Berkley, M. Reis, F. Altomare, M. H. Amin, K. Boothby, P. Bunyk, C. Deng, C. Enderud, S. Huang, E. Hoskinson, M. W. Johnson, E. Ladizinsky, N. Ladizinsky, T. Lanting, R. Li, T. Medina, R. Molavi, R. Neufeld, T. Oh, I. Pavlov, I. Perminov, G. Poulin-Lamarre, C. Rich, A. Smirnov, L. Swenson, N. Tsai, M. Volkmann, J. Whittaker, and J. Yao, "Phase transitions in a programmable quantum spin glass simulator," *Science*, vol. 361, no. 6398, pp. 162–165, 2018.

[18] A. D. King, J. Carrasquilla, J. Raymond, I. Ozfidan, E. Andriyash, A. Berkley, M. Reis, T. Lanting, R. Harris, F. Altomare, K. Boothby, P. I. Bunyk, C. Enderud, A. Fréchette, E. Hoskinson, N. Ladizinsky, T. Oh, G. Poulin-Lamarre, C. Rich, Y. Sato, A. Y. Smirnov, L. J. Swenson, M. H. Volkmann, J. Whittaker, J. Yao, E. Ladizinsky, M. W. Johnson, J. Hilton, and M. H. Amin, "Observation of topological phenomena in a programmable lattice of 1,800 qubits," *Nature*, vol. 560, no. 7719, pp. 456–460, 2018.

[19] J. M. Kosterlitz and D. J. Thouless, "Ordering, metastability and phase transitions in two-dimensional systems," *Journal of Physics C: Solid State Physics*, vol. 6, pp. 1181–1203, apr 1973.

[20] A. D. King, J. Raymond, T. Lanting, S. V. Isakov, M. Mohseni, G. Poulin-Lamarre, S. Ejtemaee, W. Bernoudy, I. Ozfidan, A. Y. Smirnov, M. Reis, F. Altomare, M. Babcock, C. Baron, A. J. Berkley, K. Boothby, P. I. Bunyk, H. Christiani, C. Enderud, B. Evert, R. Harris, E. Hoskinson, S. Huang, K. Jooya, A. Khodabandelou, N. Ladizinsky, R. Li, P. A. Lott, A. J. R. MacDonald, D. Marsden, G. Marsden, T. Medina, R. Molavi, R. Neufeld, M. Norouzpour, T. Oh, I. Pavlov, I. Perminov, T. Prescott, C. Rich, Y. Sato, B. Sheldan, G. Sterling, L. J. Swenson, N. Tsai, M. H. Volkmann, J. D. Whittaker, W. Wilkinson, J. Yao, H. Neven, J. P. Hilton, E. Ladizinsky, M. W. Johnson, and M. H. Amin, "Scaling advantage in quantum simulation of geometrically frustrated magnets," 2019.

[21] H. Rieger and A. P. Young, "Griffiths singularities in the disordered phase of a quantum ising spin glass," *Phys. Rev. B*, vol. 54, pp. 3328–3335, Aug 1996.

[22] A. P. Young and H. Rieger, "Numerical study of the random transverse-field ising spin chain," *Phys. Rev. B*, vol. 53, pp. 8486–8498, Apr 1996.

[23] M. Guo, R. N. Bhatt, and D. A. Huse, "Quantum critical behavior of a three-dimensional ising spin glass in a transverse magnetic field," *Phys. Rev. Lett.*, vol. 72, pp. 4137–4140, Jun 1994.

[24] T. Vojta, "Rare region effects at classical, quantum and nonequilibrium phase transitions," *Journal of Physics A: Mathematical and General*, vol. 39, pp. R143–R205, may 2006.

[25] T. Vojta, "Quantum griffiths effects and smeared phase transitions in metals: Theory and experiment," *Journal of Low Temperature Physics*, vol. 161, no. 1, pp. 299–323, 2010.

[26] T. Ikegami, S. Miyashita, and H. Rieger, "Griffiths-mccoy singularities in the transverse field ising model on the randomly diluted square lattice," *Journal of the Physical Society of Japan*, vol. 67, no. 8, pp. 2671–2677, 1998.

[27] E. Ising, "Beitrag zur Theorie des Ferromagnetismus," *Zeitschrift für Phys.*, vol. 31, no. 1, pp. 253–258, 1925.

[28] H. Nishimori and G. Ortiz, *Elements of Phase Transitions and Critical Phenomena*. Oxford University Press, 2010.

[29] L. Onsager, "Crystal Statistics. I. A Two-Dimensional Model with an Order-Disorder Transition," *Phys. Rev.*, vol. 65, pp. 117–149, 1944.

[30] H. Nishimori, *Statistical Physics of Spin Glasses and Information Processing*. Oxford University Press, 2001.

[31] S. F. Edwards and P. W. Anderson, "Theory of spin glasses," *J. Phys. F. Met. Phys.*, vol. 5, no. 5, p. 965, 1975.

[32] D. Sherrington and S. Kirkpatrick, "Solvable Model of a Spin-Glass," *Phys. Rev. Lett.*, vol. 35, pp. 1792–1796, Dec 1975.

[33] C. H. Papadimitriou and K. Steiglitz., *Combinatorial optimization: algorithms and complexity*. Courier Corporation, 1982.

[34] P. Hart, N. Nilsson, and B. Raphael, "A Formal Basis for the Heuristic Determination of Minimum Cost Paths," *Systems Science and Cybernetics, IEEE Transactions on*, vol. 4, pp. 100–107, July 1968.

[35] F. Glover, "Future paths for integer programming and links to artificial intelligence," *Comput. Oper. Res.*, vol. 13, no. 5, pp. 533 – 549, 1986. Applications of Integer Programming.

[36] M. Dorigo, *Optimization, Learning and Natural Algorithms*. PhD thesis, Politecnico di Milano, Italy, 1992.

[37] S. Kirkpatrick, C. D. Gelatt, and M. P. Vecchi, "Optimization by Simulated Annealing," *Science*, vol. 220, no. 4598, pp. 671–680, 1983.

[38] A. Lucas, "Ising formulations of many NP problems," *Front. Phys.*, vol. 2, no. 5, 2014.

[39] J. Hopfield and D. Tank, "Computing with neural circuits: a model," *Science*, vol. 233, no. 4764, pp. 625–633, 1986.

[40] S. Geman. and D. Geman, "Stochastic Relaxation, Gibbs Distributions, and the Bayesian Restoration of Images," *IEEE Trans. Pattern Anal. Mach. Intell.*, vol. 6, no. 6, pp. 721–741, 1984.

[41] I. Hen and F. M. Spedalieri, "Quantum annealing for constrained optimization," *Phys. Rev. Applied*, vol. 5, p. 034007, Mar 2016.

[42] I. Hen and M. S. Sarandy, "Driver hamiltonians for constrained optimization in quantum annealing," *Phys. Rev. A*, vol. 93, p. 062312, Jun 2016.

[43] K. Kudo, "Constrained quantum annealing of graph coloring," *Phys. Rev. A*, vol. 98, p. 022301, Aug 2018.

[44] S. Morita and H. Nishimori, "Convergence theorems for quantum annealing," *J. Phys. A. Math. Gen.*, vol. 39, no. 45, p. 19, 2006.

[45] S. Morita and H. Nishimori, "Mathematical foundation of quantum annealing," *Journal of Mathematical Physics*, vol. 49, no. 12, p. 125210, 2008.

[46] Y. Seki and H. Nishimori, "Quantum annealing with antiferromagnetic fluctuations," *Phys. Rev. E*, vol. 85, p. 051112, May 2012.

[47] Y. Seki and H. Nishimori, "Quantum annealing with antiferromagnetic transverse interactions for the hopfield model," *Journal of Physics A: Mathematical and Theoretical*, vol. 48, p. 335301, jul 2015.

[48] T. Lanting, A. J. Przybysz, A. Y. Smirnov, F. M. Spedalieri, M. H. Amin, A. J. Berkley, R. Harris, F. Altomare, S. Boixo, P. Bunyk, N. Dickson, C. Enderud, J. P. Hilton, E. Hoskinson, M. W. Johnson, E. Ladizinsky, N. Ladizinsky, R. Neufeld, T. Oh, I. Perminov, C. Rich, M. C. Thom, E. Tolkacheva, S. Uchaikin, A. B. Wilson, and G. Rose, "Entanglement in a quantum annealing processor," *Phys. Rev. X*, vol. 4, p. 021041, May 2014.

[49] M. Benedetti, J. Realpe-Gómez, R. Biswas, and A. Perdomo-Ortiz, "Estimation of effective temperatures in quantum annealers for sampling applications: A case study with possible applications in deep learning," *Phys. Rev. A*, vol. 94, p. 022308, Aug 2016.

[50] J. Raymond, S. Yarkoni, and E. Andriyash, "Global warming: Temperature estimation in annealers," *Frontiers in ICT*, vol. 3, p. 23, 2016.

[51] A. K. Hartmann, "Ground-state behavior of the three-dimensional $\pm j$ random-bond ising model," *Phys. Rev. B*, vol. 59, pp. 3617–3623, Feb 1999.

[52] R. B. Griffiths, "Nonanalytic behavior above the critical point in a random ising ferromagnet," *Phys. Rev. Lett.*, vol. 23, pp. 17–19, Jul 1969.

[53] T. D. Lee and C. N. Yang, "Statistical theory of equations of state and phase transitions. ii. lattice gas and ising model," *Phys. Rev.*, vol. 87, pp. 410–419, Aug 1952.

[54] B. M. McCoy and T. T. Wu, "Theory of a two-dimensional ising model with random impurities. i. thermodynamics," *Phys. Rev.*, vol. 176, pp. 631–643, Dec 1968.

[55] D. S. Fisher, "Critical behavior of random transverse-field ising spin chains," *Phys. Rev. B*, vol. 51, pp. 6411–6461, Mar 1995.

[56] A. Möbius and U. K. Rössler, "Critical behavior of the coulomb-glass model in the zero-disorder limit: Ising universality in a system with long-range interactions," *Phys. Rev. B*, vol. 79, p. 174206, May 2009.

[57] H. Rieger and N. Kawashima, "Application of a continuous time cluster algorithm to the two-dimensional random quantum ising ferromagnet," *The European Physical Journal B - Condensed Matter and Complex Systems*, vol. 9, no. 2, pp. 233–236, 1999.

[58] H. Rieger and A. P. Young, "Zero-temperature quantum phase transition of a two-dimensional ising spin glass," *Phys. Rev. Lett.*, vol. 72, pp. 4141–4144, Jun 1994.

[59] H. G. Katzgraber, F. Hamze, and R. S. Andrist, "Glassy chimeras could be blind to quantum speedup: Designing better benchmarks for quantum annealing machines," *Phys. Rev. X*, vol. 4, p. 021008, Apr 2014.

[60] J. Whittaker, "Phase transitions in a programmable quantum spin glass simulator," Qubits 2018 D-Wave Users Conference, Knoxville, 2018.

[61] "Probing mid-band and broad-band noise in lower-noise d-wave 2000q fabrication stacks," tech. rep., D-Wave Systems, May 2019.

[62] S. Bravyi, R. DiVincenzo, David P.and Oliveira, and B. M. Terhal, "The complexity of stoquastic local hamiltonian problems," *Quantum Information & Computation*, vol. 8, no. 5, pp. 361–385, 2008.

[63] I. Ozfidan, C. Deng, A. Y. Smirnov, T. Lanting, R. Harris, L. Swenson, J. Whittaker, F. Altomare, M. Babcock, C. Baron, A. J. Berkley, K. Boothby, H. Christiani, P. Bunyk, C. Enderud, B. Evert, M. Hager, A. Hajda, J. Hilton, S. Huang, E. Hoskinson, M. W. Johnson, K. Jooya, E. Ladizinsky, N. Ladizinsky, R. Li, A. MacDonald, D. Marsden, G. Marsden, T. Medina, R. Molavi, R. Neufeld, M. Nissen, M. Norouzpour, T. Oh, I. Pavlov, I. Perminov, G. Poulin-Lamarre, M. Reis, T. Prescott, C. Rich, Y. Sato, G. Sterling, N. Tsai, M. Volkmann, W. Wilkinson, J. Yao, and M. H. Amin, "Demonstration of nonstoquastic hamiltonian in coupled superconducting flux qubits," 2019.

[64] M. Suzuki, "Relationship between d-Dimensional Quantal Spin Systems and (d+1)-Dimensional Ising Systems: Equivalence, Critical Exponents and Systematic Approximants of the Partition Function and Spin Correlations," *Prog. Theor. Phys.*, vol. 56, no. 5, pp. 1454–1469, 1976.

[65] H. F. Trotter, "On the Product of Semi-Groups of Operators," *Proc. Amer. Math. Soc.*, vol. 10, no. 4, pp. 545–551, 1959.

[66] S. Bravyi, D. P. Divincenzo, R. Oliveira, and B. M. Terhal, "The complexity of stoquastic local hamiltonian problems," *Quantum Info. Comput.*, vol. 8, p. 361–385, May 2008.

[67] M. Marvian, D. A. Lidar, and I. Hen, "On the computational complexity of curing non-stoquastic hamiltonians," *Nature Communications*, vol. 10, no. 1, p. 1571, 2019.

[68] H. Suwa and S. Todo, "Markov chain monte carlo method without detailed balance," *Phys. Rev. Lett.*, vol. 105, p. 120603, Sep 2010.

[69] N. Metropolis, A. W. Rosenbluth, M. N. Rosenbluth, A. H. Teller, and E. Teller, "Equation of state calculations by fast computing machines," *The Journal of Chemical Physics*, vol. 21, no. 6, pp. 1087–1092, 1953.

[70] W. K. Hastings, "Monte carlo sampling methods using markov chains and their applications," *Biometrika*, vol. 57, no. 1, pp. 97–109, 1970.

[71] K. Hukushima and K. Nemoto, "Exchange monte carlo method and application to spin glass simulations," *Journal of the Physical Society of Japan*, vol. 65, no. 6, pp. 1604–1608, 1996.